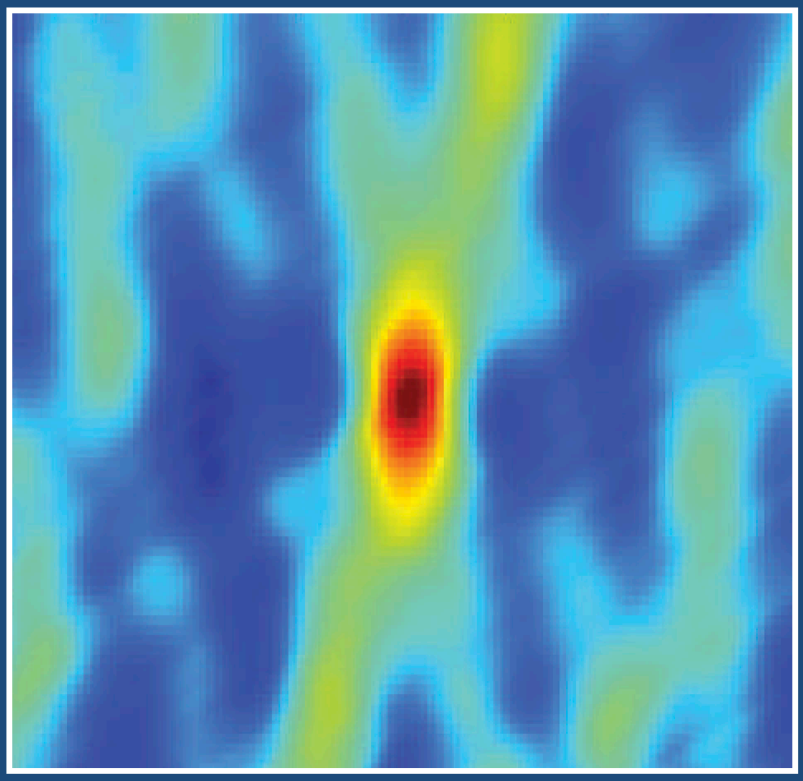

The Euclid Space Mission: Development of End-to-End Simulation Software Tools Aimed at Improving the Wavelength Calibration of NISP Instrument Spectroscopic Data

Paola M. Battaglia

Physics PhD School
Università degli Studi di Trieste

Università degli Studi di Trieste

Scuola di Dottorato in Fisica
Dipartimento di Fisica

Corso di Dottorato in Fisica
Ciclo XXX

The Euclid Space Mission: development of end-to-end simulator software tools aimed at improving the wavelength calibration of NISP instrument spectroscopic data.

Settore Scientifico Disciplinare FIS/01

Supervisor: Professoressa Anna GREGORIO

Coordinator: Professor Livio LANCERI

Tesi di Dottorato di:

Paola Maria BATTAGLIA
Matricola: PHD0400022

Anno Accademico 2016-2017

Università degli Studi di Trieste

Scuola di Dottorato in Fisica
Dipartimento di Fisica

Corso di Dottorato in Fisica
Ciclo XXX

The Euclid Space Mission: development of end-to-end simulator software tools aimed at improving the wavelength calibration of NISP instrument spectroscopic data.

Settore Scientifico Disciplinare FIS/01

Supervisor: Professoressa Anna GREGORIO

Coordinator: Professor Livio LANCERI

Tesi di Dottorato di:

Paola Maria BATTAGLIA
Matricola: PHD0400022

Anno Accademico 2016-2017

Final examination:

2 February 2018

Università degli Studi di Trieste, Dipartimento di Fisica, Trieste, Italy

"All you really need to know for the moment is that the Universe is a lot more complicated than you might think, even if you start from a position of thinking it's pretty damn complicated in the first place".

Douglas Adams

Cover illustration:

Heat map showing the correlation as a function of deformation parameters for K5 template and bright observed stellar spectrum. An intense correlation peak is well visible at the center of the image. The computation of the correlation function is part of the validation process developed in this work for the spectra location of the NISP data.

MIUR subjects:

FIS/01 - Experimental Physics

Contents

List of Figures

List of Tables

Introduction

Motivation

Our present understanding of Cosmology is that of a Universe evolving from a homogeneous state after the initial moment ("the Big Bang") to a hierarchical distribution of galaxies, clusters and super-clusters at our epoch. The most recent studies of the Cosmic Microwave Background (CMB) (see Ade et al. 2014), the relic radiation from the Big Bang, demonstrate that baryonic matter contributes only 4.9% of the total energy density of the Universe; 26.3% is a form of non-luminous matter called the **dark matter** and the remaining 68.8% is dark energy. Dark energy is linked to the observation of the non-linear accelerated expansion of the Universe deduced from independent measurements of Type Ia supernovae, while the existence of dark matter was already pointed out by Zwicky in the 1930s by comparing the dispersion velocities of galaxies in the Coma cluster with the observable star mass.

Since the discovery of these two "dark constituents" of the Universe, many questions have arisen:

- is dark energy merely a cosmological constant?
- is dark energy instead a manifestation of a break-down of General Relativity and deviations from the law of gravity?
- what are the nature and properties of dark matter?
- what are the initial conditions which seed the formation of cosmic structure?

Several observational probes can help us to disentangle different answers. Two powerful methods for dark Universe investigation are "weak gravitational lensing" and "Baryon Acoustic Oscillations" (BAOs).

The **weak gravitational lensing** technique relies on the fact that the distribution of mass along the line of sight distorts the apparent shapes and orientation of galaxies. The matter distribution, and hence cosmological structures, is obtained from the inferred gravitational field causing the weak lensing. This provides a measurement of the effect of dark energy on both the geometry and the growth of structure. Using gravitational

lensing it is also possible to probe the amount and distribution of dark matter

The **BAOs** are robust features with which to constrain Cosmology. In the early Universe fluctuations in the coupled baryon-photon fluid were subject to attractive gravity and repulsive pressure. These two effects produced a series of acoustic peaks (named Baryon Acoustic Oscillations) in both the CMB (see Sunyaev & Zeldovich 1970) and the matter power spectra (see Eisenstein & Hu 1999). BAOs have been observed in the CMB temperature-temperature power spectrum (see figure 1) using data from the Planck mission data. As galaxy surveys cover increasingly larger volumes, they too can probe the scales on which the BAOs are predicted. These have been observed, for instance, in the Sloan Digital Sky Survey (SDSS) (see section 1). The scale of the oscillations provides a standard rules and has been used to constrain dark energy parameters (see Eisenstein et al. 2005; Amendola et al. 2005) as well as neutrinos masses (see Goobar et al. 2006) and even alternative models of gravity (see Alam & Sahni 2006).

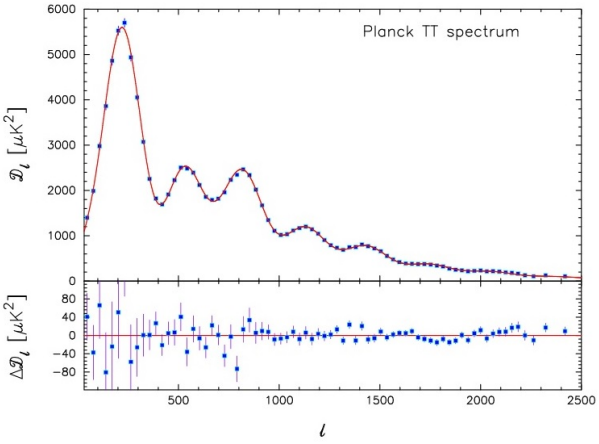

Figure 1: Planck's power spectrum of temperature fluctuations in the Cosmic Microwave Background Radiation. The red line shows the best-fit base ΛCDM spectrum. The lower panel shows the residuals with respect to the theoretical model. Credits: (see Ade et al. 2013)

Distance measurements provide one set of constraints on dark energy, but dark energy also affects how rapidly structure grows: the greater the acceleration, the more suppressed the growth of structure. Upcoming surveys are therefore designed to probe ϖ_{DE} with direct observations of the distance scale and the growth of structure.

From a technological point of view it is not trivial to exploit the gravitational lensing as an investigation method for dark matter and dark energy studies. A demanding subarcsecond angular resolution, together with the source and lens redshifts are needed to identify the lensing systems, and to transform angular quantities into masses and lengths. Radio or optical-near infrared observations, together with long exposures, are then required, preferably from space.

A great effort is being performed by the international community of scientists to perform in the forthcoming years observations with the goal of mapping hundreds of million of galaxies, through imaging and redshift surveys conducted on ground and from space.

Among these ambitious projects there is **Euclid**, a Medium Class space mission of the European Space Agency belonging to the Cosmic Vision 2015-2025 programme. The Euclid wide survey will produce a visible image of a large fraction of the extra-galactic sky (15,000 squared degrees) at a diffraction limited spatial resolution not possible from ground due to atmospheric instability. This wide survey will enable the measurement of shapes and redshifts of galaxies up to to redshift $z = 2$ as required for weak lensing and BAO.

The Euclid Payload Module comprises a 1.2 m on-axis 3-mirror Korsch cold telescope, the **Visible Instrument** (VIS) and the **Near Infrared Spectrometer and Photometer** (NISP) instrument. Currently the mission is in its phase C of development (i.e. final design and fabrication), having successfully passed the preliminary design review.

The design of a space mission is a long and complex process. For this reason, the support of dedicated software tools is necessary, especially for the performance analysis of the mission itself. The request is then for specific tools that can simulate the complete behavior of the probe, its payload (i.e. those elements of the spacecraft specifically dedicated to producing mission data), and scientific data acquisition starting from synthetic scenes.

On the other hand, detailed data quality control is essential to manage the mission, process data and achieve the science goals. Quality control is performed at the different levels of data processing: quick quality checks are done by the Science Operation Center (SOC), more elaborate quality controls involving full pipeline reductions and calibrations are done by the Instrument Operation Teams.

Once mission simulators have been developed and scientific pipeline outputs are available, there is the necessity to **verify** and **validate** these products. Software verification and validation activities check the software against its specifications. Every project must verify and validate the software it produces. This is done by:

- checking that each software item meets specified requirements
- checking each software item before it is used as an input to another activity
- ensuring that the amount of verification and validation effort is adequate to show each software item is suitable for operational use

Verification usually means the act of reviewing, inspecting, testing, checking, auditing, or otherwise establishing and documenting whether items, processes, services or documents conform to specified requirements. Validation is, according to its ANSI/IEEE definition, "the process of evaluating a system or component during or at the end of the development process to determine whether it satisfies specified requirements". Validation is, therefore, end-to-end verification.

Verification activities may include carrying out formal proofs. These activities are generally described in one or more "Software Verification and Validation Plan".

Thesis overview

Scope

Driven by the motivations described above, the present thesis describes the activities and the results obtained in the framework of the development of simulator software tools aimed at improving the wavelength calibration of the Euclid NISP instrument spectroscopic data.

The products of this research work are:

1. an End-to-End (E2ES) mission performance simulator for the Euclid NISP instrument
2. a validation process for the NISP spectra location inside the SIR Processing Function

The European Space Agency has been widely using mission performance simulators in Earth Observations programs. ESA has then promoted several activities in order to reduce the re-engineering effort to generate E2E simulators, and to test the feasibility of a generic environment for space missions. The activity described in this thesis at sections 3 and 4 has been supported within the ESA contract no. IPL-PTE/GLC/al/241.2014, and has been executed under the supervision of Dr. A. Gregorio (Physics Department, University of Trieste). I focused mainly on the verification and validation of the E2ES, reviewing requirements, conceiving test cases, preparing and executing test sequences and producing test reports.

Exploiting the experience matured on the validation of the Euclid NISP E2ES, from May 2016 I have being involved in a collaboration with INAF-IASF Milano to assess if the wavelength calibration accuracy of NISP spectroscopic data can be validated using spectra of bright stars within the spectroscopic data set produced by the SIR Processing Function. Activities have been performed under the supervision of the SIR OU leader, Dr. M. Scodeggio.

Organizational note

The present Thesis consists of five main sections.

Chapter 1 is related to our present understanding of the so-called "dark Universe". This section describes the observational evidences for the existence of DM and DE, from early indications, to most recent ones. It is pointed out how gravitational lensing and the measure of the clustering of galaxies at multiple redshifts are powerful tools for dark components investigation.

Chapter 2 deals with the technical challenges related to weak gravitational lensing and large surveys of galaxy large scale structures, including an overview of the experiments dedicated to the quest of the dark components of the Universe. An entire section is dedicated to the Euclid space mission, giving prominence to the Near Infrared Spectrometer and Photometer (NISP) instrument, and the data processing system of the mission.

In **Chapter 3** and **Chapter 4** there is the description of the E2ES simulator of the NISP instrument, of its architecture and of the implemented versions. The software validation concept is deepened, and results of the conceived validation plan are presented.

Finally **Chapter 5** describes the activities and the results obtained in the framework of the development of the module dedicated to the validation of the NISP spectra location.

CHAPTER 1

A Dark Universe

1.1 Introduction

Our present understanding of cosmology is that of the Universe evolving from a homogeneous state after the initial moment ("the Big Bang") to a hierarchical distribution of galaxies, clusters and super-clusters at our epoch. Such a view relies on several assumptions about the initial conditions of the Universe and the nature of the gravity itself, and on the observational evidence that the Universe is not dominated by the ordinary matter, but instead by two components whose origin is still mysterious.
The most recent studies of the Cosmic Microwave Background (CMB), the relic radiation from the Big Bang, demonstrate indeed that baryonic matter contributes only 4.9% of the total energy density of the Universe. The remaining 95.1% of the content of the Universe is split up as follows: 26.3% is a form of non-luminous matter called the ***dark matter*** (DM) and 68.8% is ***dark energy*** (DE) (see Ade et al. 2014).

DE is responsible for the observation of the non-linear accelerated expansion of the Universe deduced from independent measurements of Type Ia supernovae (see Riess et al. 1998). The expression *dark energy* may be somewhat confusing in the sense that a similar expression, *dark matter*, has been used to describe a pressure-less matter (a non-relativistic matter) that interacts weakly with standard matter particles.

The existence of DM was already pointed out by Zwicky in the 1930s by comparing the dispersion velocities of galaxies in the Coma cluster with the observable star mass (see Zwicky 1937). Since DM does not mediate the electromagnetic force, its presence is mainly inferred from gravitational effects on visible matter. DM can cluster by gravitational instability (unlike standard dark energy) so that local structures have been formed in the Universe. In fact it is observationally known that DM has played a central role for the growth of large-scale structures such as galaxies and cluster of galaxies.

The black body radiation, which dominated over the matter components in the past, shares only about 0.005% of the present total energy density.
In modern cosmology it is believed that another cosmic acceleration called *inflation* occurred in the very early Universe prior to the radiation-dominated epoch. The idea of inflation was originally proposed in the early 1980s by a number of people to solve several cosmological problems such as the flatness and horizon problems (see Guth 1981).

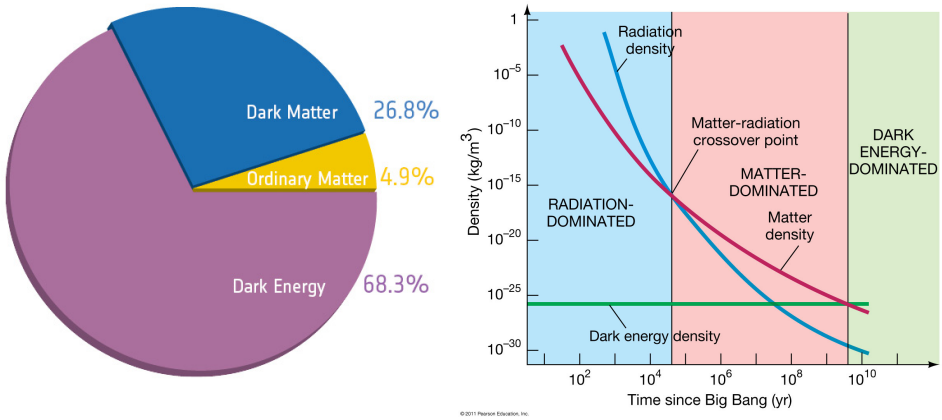

Figure 1.1: ***Left:*** *Planck's high-precision cosmic microwave background map has allowed scientists to extract the most refined values yet of the Universe's ingredients. The "before Planck" figure is based on the WMAP 9-year data release presented by Hinshaw et al., (see Hinshaw et al. 2013). Credits: ESA and the Planck Collaboration.* ***Right:*** *the density evolution of the main components of the Universe. The early Universe was radiation-dominated, until the temperature dropped enough for matter density to being to dominate. The energy density of dark energy is constant if its equation of state parameter $w = 1$. Because the matter energy density drops as the scale factor increased (see section 1.3), dark energy began to dominate in the recent past. At the present time ($a(t) = 1$), we live in a Universe dominated by dark energy. Credits:* `http://pages.uoregon.edu/jimbrau/BrauImNew/Chap27/7th/AT_e_Figure_27_01.jpg`

Inflation provides also a mechanism for the origin of large-scale structure in the Universe.

A strong support for the existence of an inflationary era as well as DE comes from the observational data of **CMB anisotropies**. Such anisotropies have been observed firstly by the Cosmic Background Explorer (COBE) in 1992, then by the Wilkinson Microwave Anisotropy Probe (WMAP) after 2003 and, finally, by the Planck probe which in 2013 released the most accurate observational data.

After the end of inflation the Universe entered the radiation-dominated epoch (see figure 1.1) during which light elements such as helium and deuterium were formed. The temperature anisotropies observed by CMB experiments occur at the last scattering surface, i.e. the events horizon at the epoch of recombination, when electrons were trapped by hydrogen to form atoms. After this *decoupling epoch* photons are free to move toward us without experiencing Thomson scattering.

The formation of galaxies and clusters of galaxies started in the matter-dominated epoch, i.e. when the DM began to dominate the total energy density of the Universe. Baryons also contribute to the formation of large-scale structure to some extent. During the matter era the energy density of DE needs to be suppressed compared to that of DM in order to allow sufficient growth of large-scale structure. If DE couples to DM with some interaction, as in the coupled quintessence scenario (see Amendola 2000), then dark energy also affects the past expansion history of the Universe as well as the structure formation. Constraints on the strength of such coupling can be inferred from the observations of the CMB and of galaxy clustering.

The simplest candidate for dark energy is the so-called **cosmological constant** Λ, whose energy density remains constant. While the energy density of DM evolves as $\rho_m \propto a^{-3}$ (a is the scale factor of an expanding Universe, see section 1.3), the dark energy density is nearly constant in time ($\rho_{de} \propto a^{-n}$ with n probably close to 0). Hence the latter energy density eventually meets the former. Cosmic acceleration begins around the redshift $z \approx 1$, although there is still uncertainty for its precise value because of the model-dependence. The standard radiation-and matter-dominated ages are between two periods of cosmic acceleration inflation and dark energy.

The cosmological constant was originally introduced by Albert Einstein in 1917 to realize a static Universe in the framework of General Relativity (see Einstein 1917). As a static solution of the field equations of general relativity with added cosmological term, he obtained a Universe with spatial geometry of a three-dimensional sphere. In Einstein treatment the cosmological constant is universal, i.e. it must be constant throughout the whole Universe. But it is not fundamental: its value is determined by the matter density in the Universe. Einstein noted that the Λ-term must be added to his equations if the density of matter in the Universe is non-zero in average.

After the discovery of the expansion of the Universe in 1929 (see Hubble 1929) by Hubble from the measurement of recession speeds of distant galaxies, Einstein abandoned the idea of adding the Λ term to the equations. Around 1998 the cosmological constant appeared again as a form of dark energy responsible for the late-time acceleration of the Universe.

The origin of the cosmological constant is unknown. With the development of the quantum field theory it was recognized that the Λ-term is related to "zero-point motion of quantum fields". It describes the energy–momentum tensor of the quantum vacuum, $T^{\mu\nu}_{vac} = \Lambda g^{\mu\nu}$. This means that Λ is nothing but the energy density of the vacuum, $\Lambda = \rho_{vac}$, i.e. the vacuum can be considered as a medium obeying the equation of state:

$$\rho_{vac} = -p_{vac} \tag{1.1}$$

Such view on the cosmological constant led to principle difficulties. The main two problems are:

- the energy density of the zero-point motion is highly divergent because of the formally infinite number of modes
- the vacuum energy is determined by the high-energy degrees of quantum fields, and thus at first glance must have a fixed value which is not sensitive to the low-density and low-energy matter in the present Universe, which is also in disagreement with observations.

The naive summation over all the known modes of the quantum fields up to the Planck scale gives an estimate for the energy density equal to $\rho_{vac} \cong 10^{76} GeV^4$ (see Luo 2014). This estimate of the cosmological constant exceeds by 120 orders of magnitude the upper limit posed by astronomical observations. The introduction of new (currently unknown) physics could change this result. For example, supersymmetry would bring the discrepancy from 120 orders of magnitude to 60 orders of magnitude (see Volovik 2005).

However, none of these proposal justify the fact that the observed value of the cosmo-

logical constant is of the same order of magnitude of the observed value of the matter density. This was a problem even when the cosmological constant was believed to be exactly zero (see Weinberg 1989) and various possibilities have been proposed.

If the origin of DE is not the cosmological constant, some alternative models must be found in order to explain the cosmic acceleration today. Basically there are two approaches to construct models of DE other than the cosmological constant.

The first approach is to build **scalar-field models of dark energy** based on particle physics (see Binetruy 1999). The representative models that belong to this class are the so-called *cosmon* or *quintessence* (see Zlatev et al. 1999), k-essence (see Armendariz-Picon et al. 2001), and perfect fluid models (see Kamenshchik et al. 2001).In the context of inflation, since the associated energy scale is high, it is natural for scalar fields to be responsible for the acceleration of the Universe. The situation is different for DE - its energy scale is too low compared to typical scales appearing in particle physics. Moreover, the field potentials need to be sufficiently flat so that the field evolves slowly enough to drive the present cosmic acceleration.

The second approach for the construction of DE models is that of the models called *f* (R) gravity, scalar-tensor theories (see Perrotta et al. 2000), and braneworld models (see Sahni & Shtanov 2003). The cosmological constant scenario (in other words the "Λ *Cold Dark Matter* (ΛCDM) model") corresponds to the Lagrangian density $f(R) = R - 2\Lambda$, where R is the Ricci scalar. A possible modification of the ΛCDM is described by a nonlinear Lagrangian density *f* in terms of R, which is called *f*(R) gravity. Generally we require that modified gravity models satisfy local gravity constraints as well as conditions for the cosmic acceleration preceded by the matter-dominated epoch. It is important to realize however that the two approaches, the modified matter and modify gravity, are not fundamentally different. From the viewpoint of classical General Relativity, one can always rephrase one into the other by defining a suitable conserved energy-momentum tensor that equals the Einstein tensor.

In order to distinguish this variety of models of DE, it is important to place constraints by using observational data such as SN Ia, CMB, and large-scale structure (LSS). Usually the equation of state of DE, $\varpi_{DE} \equiv P_{DE}/\rho_{DE}$, where P_{DE} is the pressure and ρ_{DE} is the energy density, is a good measure to describe the property of dark energy at a background level. In the case of the cosmological constant we have $P_{DE} = -\rho_{DE}$ and hence $\varpi_{DE} = -1$.

In other models of DE the equation of state ϖ_{DE} generally varies in time. The SN Ia observations have provided information of cosmic expansion history around the redshift $z \leq 2$ by the measurement of luminosity distances of the sources. The presence of DE leads to a shift of the position of acoustic peaks in CMB anisotropies as well as modification of the large-scale CMB spectrum through the so-called integrated Sachs-Wolfe (SW) effect which is the predominant source of fluctuations in the CMB for angular scales above ten degrees. Although the CMB data alone are not sufficient to place strong constraints on DE, the combined analysis of SN Ia and CMB can provide tight bounds on the equation of state ϖ_{DE} and the present energy fraction Ω^0_{DE} of DE (see Komatsu et al. 2009).

The distribution of **large-scale clustering of galaxies** in the sky also provides additional

information on the properties of DE. In 2005 the detection of a peak of **Baryon Acoustic Oscillations** (BAO) was reported at the average redshift $z = 0.35$ from the observations of luminous red galaxies in the Sloan Digital Sky Survey (see Eisenstein et al. 2005). This also given us another independent test of DE. From the combined analysis of CMB data and BAO, the Planck collaboration (see Ade et al. 2013) find no evidence for dynamical DE. The dark energy equation of state parameter is constrained to be $\varpi_{DE} = -1.13^{+0.13}_{-0.10}$. The cosmological constant ($\varpi_{DE} = -1$) is well consistent with the current observational data while some DE models have been already excluded from observations.

In the following sections we will offer a review of the expanding Universe, the Cosmological Standard Model and the inflation. We will then report the observational evidence for DM and DE. Specifically, section 1.5 deals with indications for DM and gravitational lensing. Section 1.6 treats DE and the accelerating Universe.

1.2 Expanding Universe

When the spectra of galaxies were first observed in the early 1900s it was found that their observed spectral lines, such as those of hydrogen and calcium, were shifted from the positions of the lines when observed in the laboratory. In the closest galaxies the lines were shifted toward the blue end of the spectrum, but for galaxies beyond our Local Group, the lines were shifted towards the red.

This effect is called a **redshift** or **blueshift** and the simple explanation attributes this effect to the speed of approach or recession of the galaxy. For speeds which are small compared with the speed of light, then the following simple formula may be used:

$$\Delta f/f = \Delta\lambda/\lambda = v/c = z \tag{1.2}$$

where f is the frequency, λ is the wavelength, Δf and $\Delta\lambda$ are changes in frequency and wavelength, v is the velocity of approach or recession and c is the speed of light.

By 1915 the American astronomer Vesto Slipher had measured the shifts for 15 galaxies, 11 of which were redshifted. Two years later, a further six redshifts had been measured and it became obvious that only the nearer galaxies (those within our Local Group) showed blueshifts. From the measured shifts and, using the Doppler formula given above, he was able to calculate the velocities of approach or recession of these galaxies.

These data were used by Edwin Hubble in what was perhaps the greatest observational discovery of the last century. In the late 1920s, Edwin Hubble, using the 100 in. Hooker Telescope on Mount Wilson, measured the distances of galaxies using the Cepheid variables method. He discovered that all, except the closest galaxies, are receding from us with a recession velocity which is linearly proportional to the distance (see figure 1.2), and follows **Hubble's law**,

$$v = H_0 D \tag{1.3}$$

The proportionality coefficient is the **Hubble parameter**, and it is often called the "*Hubble constant*", though it is not truly a constant.
Its actual value is $H_0 = (67.74 \pm 0.46)\,\mathrm{km\,s^{-1}\,Mpc^{-1}}$ (see Ade et al. 2016).

There are several immediate consequences to the observation of Hubble's law:

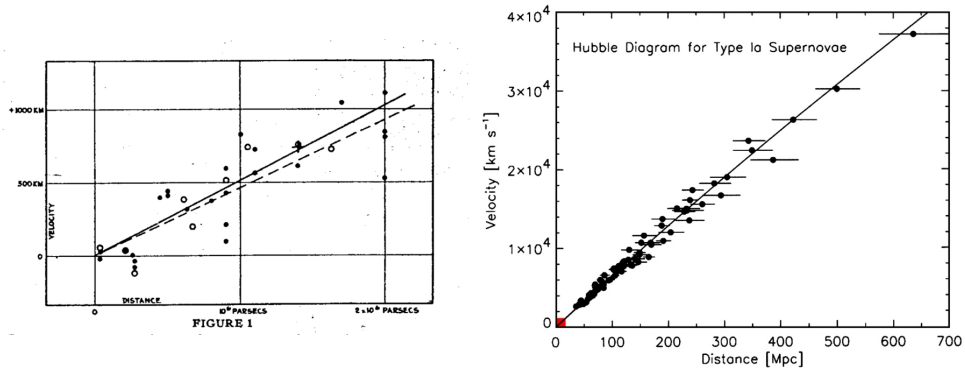

Figure 1.2: ***Left:*** *original Hubble's diagram (see Hubble 1929) - Radial velocities, corrected for solar motion, are plotted against distances estimated from involved stars and mean luminosities of nebulae in a cluster. The black discs and full line represent the solution for solar motion using the nebulae individually; the circles and broken line represent the solution combining the nebulae into groups; the cross represents the mean velocity corresponding to the mean distance of 22 nebulae whose distances could not be estimated individually.* ***Right:*** *the Hubble diagram for type Ia supernovae (see Kirshner 2003). The scatter about the line corresponds to statistical distance errors of 10% per object. The small red region in the lower left marks the span of original Hubble's diagram from 1929.*

1. all galaxies are moving away from each other, i.e. the Universe is expanding
2. there is no center to this expansion since, as we have seen, observers in all galaxies see the same expansion
3. in the past the Universe must have been denser
4. finally, if the expansion has been going on for long enough, there was a time when distances between all galaxies was zero. This follows from the linear dependence of velocity on distance.

From the last statement of the above list it follows that the Universe has a finite age. If galaxies do not accelerate or decelerate, then that age is given by:

$$t_0 = \frac{1}{H_0} = \frac{1}{67.74\,\mathrm{km\,s^{-1}\,Mpc^{-1}}} = \frac{3.1 \times 10^{24}\,\mathrm{cm}}{67.74 \times 10^5\,\mathrm{cm\,s^{-1}}} = 4.6 \times 10^{17}\,\mathrm{s} \cong 14\,\mathrm{Gyr} \qquad (1.4)$$

It turns out that this "**Hubble time**" is close to the current best estimates of the age of the Universe.

If the Universe is expanding, then it would have been smaller in the past. When a photon has been emitted in a distant galaxy corresponding to a specific spectral line, the Universe would have been smaller. In the time it has taken that photon to reach us whilst the photon has been traveling through space, the Universe has expanded and this expansion has stretched, by exactly the same ratio, the wavelength of the photon. This increases the wavelength so giving rise to a redshift that is a very nice interpretation of the parameter z (see equation 1.2) and it is called the **cosmological redshift**. If we find that a galaxy is observed at a redshift of z, then, by adding 1 to that value we can find the ratio of the wavelengths of the photons observed to those emitted. This simply means that we "see" the galaxy at a time when the universe was smaller by just this ratio, $(1 + z)$.

1.3 The Cosmological Standard Model

The dynamics of the expanding Universe is described by the two Friedmann equations derived from Einstein's theory of general relativity:

$$\frac{\dot{a}^2 + kc^2}{a^2} = \frac{8\pi G\rho + \Lambda c^2}{3} \tag{1.5}$$

$$\frac{\ddot{a}}{a} = -\frac{4\pi G}{3}\left(\rho + \frac{3p}{c^2}\right) + \frac{\Lambda c^2}{3} \tag{1.6}$$

where $H \equiv \frac{\dot{a}}{a}$ is the **Hubble parameter**, G is the Newton's gravitational constant, Λ is the **cosmological constant**, and c is the speed of light in vacuum.

These solutions produced a set of models (called by F. Hoyle **Big Bang models**) in which the Universe expanded from a point, or singularity. Standard hot big bang cosmology is based on the ***cosmological principle***, which states that the Universe is homogeneous and isotropic at least on large scales.

Homogeneity is evidenced by the form of Hubble's Law (see equation 1.3), which is such that every observer sees the same expansion. Furthermore, this is supported by a large number of observations, such as the CMB photons coming from different part of the sky with almost the same temperature. Inhomogeneities and irregularities (such as stars and galaxies) are observable in the local region of the Universe. These inhomogeneities have grown in time through gravitational instability from a matter distribution that was more homogeneous in the past. Then the inhomogeneities can be regarded as small perturbations evolving on the background, homogeneous Universe.

The linear form of Hubble's Law, $v = H_0 D$, leads at large enough distances to velocities $v > c$. This suggests that, to describe the dynamics of the Universe, we require a relativistic theory of gravity, namely **General Relativity**. General Relativity relates the density of mass and energy, which are the sources of gravity, to the curvature of spacetime. The curvature is described by a metric tensor, which specifies the line element of the curved spacetime. It is possible to demonstrate (see Maoz 2007) that the metric of the Universe that corresponds to the Cosmological Principle of isotropy and homogeneity is the **Friedman-Lemaître-Robertson-Walker (FLRW) metric**:

$$ds^2 = -c^2dt^2 + a^2(t) = \frac{dr^2}{1 - kr^2} + r^2(d\theta^2 + sin^2\theta d\phi^2) \tag{1.7}$$

where ds_3^2 is a three dimensional metric that must be one of a flat space, a sphere of constant positive curvature or hyperbolic space with constant negative curvature. The quantity $a(t)$ is a crucial one. It is called the **scale factor of the Universe** and it measures the universal expansion rate. For example, if $a(t)$ grows with time, every observer sees other points in the Universe receding radially, just as in the observed Hubble expansion of galaxies. Thus, a galaxy at coordinates (r, θ, ϕ) remains at those coordinates, and it is the coordinate system, which is "locked" onto the galaxies, that expands according to $a(t)$. The coordinates (r, θ, ϕ) are therefore called **comoving coordinates**.

The expansion rate at time t is given by

$$H^2(t) \equiv \left(\frac{\dot{a}}{a}\right)^2 = \frac{8\pi G}{3}\sum_i \rho_i - \frac{k}{a^2} + \frac{\Lambda}{3} \tag{1.8}$$

The first term on the right hand side is proportional to the sum over all energy densities in the Universe ρ_i including baryons, photons, neutrinos, dark matter and dark energy. The second term is the curvature term. Finally, the dark energy term has been pulled explicitly out of the sum and placed it in the third term assuming it is a constant.

The cosmological constant Λ has been introduced by Einstein to his equations of general relativity to counteract the attractive effects of gravity on ordinary matter, which would otherwise cause a spatially finite Universe to either collapse or expand forever. At that time the most accredited theory for the origin of the Universe was the **Steady State** one: the Universe has no beginning and will have no end and is, as the theory's name implies, in a "steady state".The deathblow to the Steady State theory came in 1963 when radiation, believed to have come from the Big Bang, was discovered by a lucky accident by radio astronomers Arno Penzias and Robert Wilson. It was an American physicist, George Gamow, who first realized that the Big Bang should have resulted in radiation that would still pervade the Universe. However, incontrovertible proof as to its origin had to wait until 1990 when the COBE satellite was able to show that the background radiation has the precise black body spectrum that would have been expected (see Mather et al. 1990).

Equation 1.8 can be transformed in a form useful for numerical integration if we introduce Ω parameters:

$$\Omega_i \equiv \frac{8\pi G}{3H^2}\rho_i, \Omega_\Lambda \equiv \frac{8\pi G}{3H^2}\rho_\Lambda = \frac{\Lambda}{3H^2}, \Omega_k \equiv \frac{-k}{(aH)^2} \tag{1.9}$$

Dividing equation 1.10 by H^2 we get the sum rule $1 = \Omega_m + \Omega_k + \Omega_\Lambda$, which is true at all times, where Ω_m is the sum over all Ω_i excluding dark energy. At the present time $H(t) = H_0$, $a = 1$, and cosmological density parameters become

$$\Omega_i(0) = \frac{8\pi G}{3H_0^2}\rho_i(0), \Omega_\Lambda(0) = \frac{\Lambda}{3H_0^2}, \Omega_k(0) = \frac{-k}{H_0^2} \tag{1.10}$$

Equation 1.10 can then be manipulated into the form:

$$\dot{a} = H_0[\Omega_m(0)(a^{-1} - 1) + \Omega_\gamma(0)(a^{-2} - 1) + \Omega_\Lambda(0)(a^2 - 1) + 1]^{1/2} \tag{1.11}$$

In equation 1.11 it has been explicitly introduced a density parameter for the background radiation field Ω_γ and used the fact that matter and radiation densities scale as a^{-3} and a^{-4}, respectively, and it has been used the sum rule to eliminate Ω_k. Equation 1.11 is equation 1.8 expressed in terms of the current values of the density and Hubble parameters, and makes explicit the scale factor dependence of the various contributions to the expansion rate. In particular, it is clear that the expansion rate is dominated first by radiation, then by matter, and finally by the cosmological constant.

Current measurements of the **cosmological parameters** by the Planck mission (see Ade et al. 2016) yield the following numbers:

$$H_0 = (67.81 \pm 0.92)\,\mathrm{km\,s^{-1}\,Mpc^{-1}} \tag{1.12}$$

$$\Omega_\Lambda = 0.692 \pm 0.012, \Omega_m = \Omega_{cdm} + \Omega_b = 0.308 \pm 0.012 \tag{1.13}$$

In all Big Bang models, the initially fast rate of expansion is slowed by the attractive gravitational force between the matter of the Universe. If the density of matter within the Universe exceeded a critical amount, it would be sufficient to cause the expansion to cease and then the Universe would collapse down to a **Big Crunch** ("closed universes"). If the actual density was less than the critical density, the Universe would expand for ever ("open" universes). In the critical case that is the boundary between the open and closed universes, the rate of expansion would fall to zero after infinite time ("flat" or "critical" universe)(see figure 1.3).

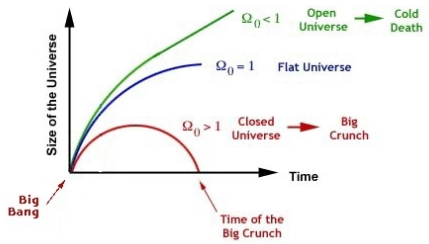

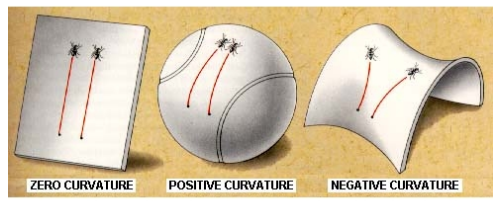

Figure 1.3: ***Left****: the figure shows a plot of the size of the Universe versus time. The competition between the violence of the initial explosion and the slow-down effect of gravity has been considered only. Credits:* `http://www2.astro.psu.edu/~mce/A001/lect23.html`.***Right****: possible Universe geometry in relation to its mass content. Credits:* `https://starchild.gsfc.nasa.gov/docs/StarChild/questions/question35.html`

The models are distinguished by the constant Ω that is defined as the ratio of the actual density to the critical density, and is equal to the sum of Ω_Λ and Ω_m. In closed universes, Ω is greater than 1, space has positive curvature, the angles within a triangle add up to more than 180 degrees and two initially parallel light rays would converge. In open universes, Ω is less than 1, space has negative curvature, the angles within a triangle add up to less than 180 degrees and two initially parallel light rays would diverge. In the critical case, Ω is equal to 1, space is said to be "flat", the angles within a triangle add up to 180 degrees and two initially parallel light rays will remain parallel.

The actual set of parameters for energy densities, with $\Omega = 1$, constituting the so called "**concordance model**", describes then a spatially flat, low matter density, high dark energy density Universe in which baryons, neutrinos, and photons make a negligible contribution to the large scale dynamics. Most of the matter in the Universe is cold dark matter (CDM).

1.4 Inflation

By the 1970s, problems with the standard Big Bang models had arisen. Observations have shown that the Universe was very close to being "flat", $\Omega \sim 1$, and the Big Bang theory gives no particular reason why this should be so (**"flatness problem"**). A second

problem is known as the **"horizon problem"**.

The Universe appears to have exactly the same properties – specifically the observed temperature of the CMB – in opposing directions. The CMB from one direction has taken nearly 14 billion years to reach us, and the same from the opposing direction. In the standard Big Bang models there has not been sufficient time to allow radiation to travel from one of these regions to the other – they cannot "know" what each other's temperature is, as this information cannot travel faster than the speed of light.

These problems were addressed with the idea of **inflation**, first proposed by Alan Guth (see Guth 1981) and refined by others. In this scenario the whole of the visible Universe would have initially been contained in a volume of order the size of a proton. Some 10^{-35} s after the origin this volume of space began to expand exponentially and increased in size by a factor of order 10^{26} in a time of $\sim 10^{-32}$ s to the size of a sphere a meter or more in size. This massive expansion of space would force the geometry of space to become "flat". Inflation would also ensure that the whole of the visible Universe would have uniform properties so also addressing the horizon problem (see 1.4). This is a result of the fact that, prior to the inflationary period, the volume of space that now forms the visible Universe was sufficiently small that radiation could easily travel across it and so give it a uniform temperature. Furthermore, according to the standard

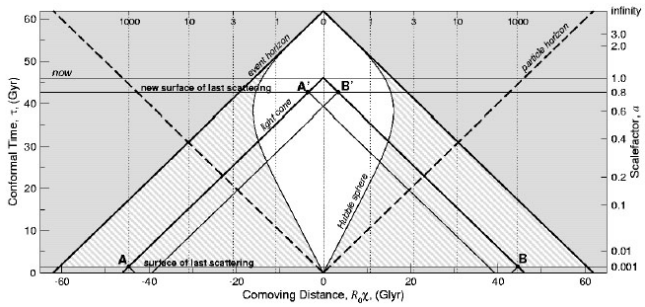

Figure 1.4: Inflation shifts the position of the surface of last scattering. The image shows what the insertion of an early period of inflation does to the past light cones of two points, A and B, at the surface of last scattering on opposite sides of the sky. An opaque wall of electrons - the cosmic photosphere, also known as the surface of last scattering - is at a scale factor $a \cong 0.001$ when the Universe was approx 1000 times smaller than it is now and only 380,000 years old. The past light cones of A and B do not overlap - they have never seen each other - they have never been in causal contact. And yet we observe these points to be at the same temperature. This is the "horizon problem". Inserting an early epoch of inflation onto the big bang model moves the surface of last scattering upward to the line labeled "new surface of last scattering". Points A and B move upward to A' and B'. Their new past light cones overlap substantially. They have been in causal contact for a long time. Without inflation there is no overlap. With inflation there is. That is how inflation solves the problem of identical temperatures in "different" horizons. Credits: `https://ned.ipac.caltech.edu/level5/March03/Lineweaver/frames.html`

cosmological model, the largest structures that we observe today (i.e. galaxies and clusters of galaxies) grew out of small initial fluctuations that were seeded during the phase of in inflationary expansion. Subsequently these fluctuations grew under the influence of gravity. Most of the growth occurred after the decoupling of photons and electrons, since at that point the Universe was mostly matter-dominated, and this fact allowed the galactic-size structures to grow unimpeded.

1.5 Observational Evidence for Dark Matter

1.5.1 Early Indications

Astronomers have long relied on photometry to yield estimates on mass, specifically through well defined mass to luminosity ratios (M/L). Usually one measures mass to luminosity in terms of the Sun's mass and luminosity such that $M_\odot/L_\odot = 1$ by definition. Thus by measuring the light output of an object (for example a galaxy or cluster of galaxies) one can use well-defined M/L ratios in order to estimate the mass of the object.

In the second half of the 1930s the Swiss astronomer Fritz Zwicky found indication of missing mass in a cluster of galaxies (see Zwicky 1937). Zwicky studied the Coma cluster, about 99 Mpc (322 million lightyears) from Earth, and, using observed doppler shifts in galactic spectra, was able to calculate the velocity dispersion of the galaxies in the Coma cluster. Knowing the velocity dispersions of the individual galaxies (i.e. kinetic energy), Zwicky employed the virial theorem to calculate the cluster's mass. Assuming only gravitational interactions and Newtonian gravity ($F \propto 1/r^2$), the virial theorem gives the following relation between kinetic and potential energy:

$$\langle T \rangle = -\frac{1}{2} \langle U \rangle \tag{1.14}$$

where $\langle T \rangle$ is the average kinetic energy and $\langle U \rangle$ is the average potential energy.

Zwicky found that the total mass of the cluster was $M_{cluster} \approx 4.5 \times 10^{13} M_\odot$. Since he observed roughly 1000 nebulae in the cluster, Zwicky calculated that the average mass of each nebula was $M_{nebula} = 4.5 \times 10^{10} M_\odot$. This result was remarkable because a measurement of the mass of the cluster using standard M/L ratios for nebulae gave a total mass for the cluster approximately 2% of this value. Galaxies, then, only accounted for only a small fraction of the total mass; the vast majority of the mass of the Coma cluster was for some reason "**missing**" or "**non-luminous**" (although not known to Zwicky at the time, roughly 10% of the cluster mass is contained in the intracluster gas which slightly improves but does not solve the issue of missing mass, (see Zwicky 1937)).

In the 1970s the American astronomer Vera Rubin observed the light from HII regions (ionized clouds of hydrogen such as the Orion Nebula) in a number of spiral galaxies. These HII regions move with the stars and other visible matter in the galaxies but, as they are very bright, are easier to observe than other visible matter. HII regions emit the deep red hydrogen alpha (H-alpha) spectral line. By measuring the Doppler shift in this spectral line Rubin was able to plot their velocities around the galactic center as a function of their distance from it. What emerged is that the rotational speed of the clouds did not decrease with increasing distance from the galactic center and, in some cases, even increased somewhat. The only way these results can be explained is that either the stars in the galaxy are embedded in a large halo of unseen matter – extending well beyond the visible galaxy – or that Newton's law of gravity does not hold true for large distances. The unseen matter, whose gravitational effects Rubin's observations had discovered, is called "**dark matter**". Rubin summarized, "The conclusion is inescapable: mass, unlike luminosity, is not concentrated near the center of spiral galaxies. Thus the light distribution in a galaxy is not at all a guide to mass distribution." (see Rubin 1983).

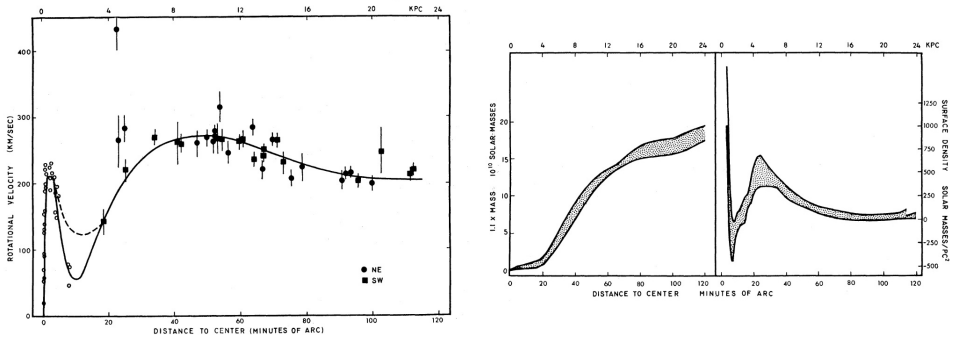

Figure 1.5: ***Left****: rotational velocities for HII regions in M31, as function of distance from the center. Solid curve is a fifth-order polinomial fitting (for distances* $< 12'$*); for distances greater than 12′ curve is fourth-order polynomial required to remain approximately flat near a distance equal to 120′. Dashed curve near a distance of 10′ is a second rotation curve with higher inner minimum.* ***Right****: the mass contained within a certain radius of the center of M31 (left part of the image). In the right part of the image, the corresponding density at the radius. Notice how in the left panel, even at large radii (*$> 20kpc$*) the mass is still increasing. (see Rubin 1970)*

1.5.2 Gravitational Lensing

In the 1970s, another way to probe the amount and distribution of DM was discovered: **gravitational lensing**. In his famous article "Lens-Like Action of a Star by the Deviation of Light in the Gravitational Field" (see Einstein 1936), Albert Einstein introduced the concept of gravitational lensing - the bending of light around massive objects, which serves as one of the prime predictions of his General Theory of Relativity and was confirmed by observation of the "Twin QSO" SBS 0957+0561.

The gravitational deflection of light generated by mass concentrations along a light path produces magnification, multiplicity, and distortion of images and delays photon propagation from one line of sight relative to another. The manifestation of gravitational lensing can be strong or weak, with additional features such as Einstein's rings, arcs and crosses that modify the phenomenological study of effects of strong gravity. To see the effects of gravitational lensing, cosmologists look for a relatively close, massive object (often a cluster of galaxies) behind which a distant, bright object (often a galaxy) is located. If the distant galaxy is located directly behind the massive object, a complete "Einstein ring" would appear. However, the likelihood of two bright and distant objects lining up perfectly with the Earth is low; thus, distorted galaxies generally appear as "arclets" or partial Einstein rings (see figure 1.6).

In 1916 Einsten derived the correct formula for the deflection angle α of a light passing at a distance r from an object with mass M as:

$$\alpha = \frac{4GM}{c^2 r^2} \tag{1.15}$$

In 1937 Zwicky reaffirmed the Einstein effect ("On the Probability of Detecting Nebulae Which Act as Gravitational Lenses", Physical Review, vol. 51, Issue 8, pp. 679-679), when he stated that "the probability that *extragalactic nebulae* which act as gravitational

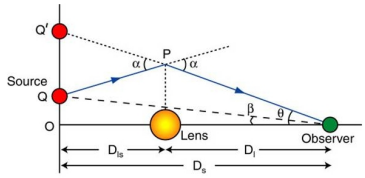

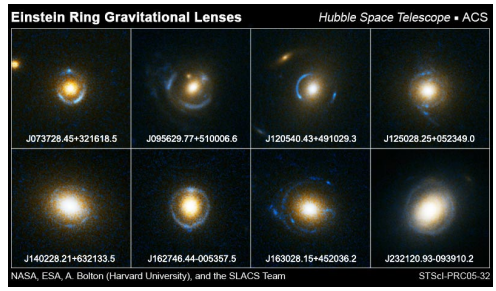

Figure 1.6: ***Left****: geometry of a gravitational lens system. Light from the background object at Q follows the trajectory shown by the blue arrow, deflecting by angle at P and then travelling to the observer. As a result, the observer sees the image at Q' rather than Q. (Image credit:* `http://www.jb.man.ac.uk/distance/frontiers/glens/section2.htm`*)* ***Right****: the thin blue bull's-eye patterns in these eight Hubble images appear like neon signs floating over reddish-white blobs. The blobs are giant elliptical galaxies roughly 2 to 4 billion light-years away. The bull's-eye patterns are created as the light from galaxies twice as far away is distorted into circular shapes by the gravity of the giant elliptical galaxies. (Image credit: NASA/ESA/SLACS Survey Team)*

lenses will be found practically a certainty". He also established gravitational lensing as a precursor to significant breakthroughs, such as a means to determine the DM content of individual galaxies and galaxy clusters.

Until the late 1970s, gravitational lensing was limited to only the premise of our galaxy. It was only in 1979 that the first example of an extragalactic gravitational lens was provided by the observation of the distant quasar QSO 0957+0561, by D. Walsh, R.F. Carswell, and R.J. Weymann with the $2.1m$ Telescope at the Kitt Peak National Observatory, Arizona. The next significant observation was in 1985, that of the "Einstein's cross - a lensing system producing a four-leaf clover, formed by the quasar QSO 237+0305".

We can study a distant galaxy's distorted image and make conclusions about the amount of mass within a lensing cluster using this expression for θ_E, the "Einstein radius" (the radius of an arclet in radians):

$$\theta_E = \sqrt{\frac{4GM}{c^2}\frac{d_{LS}}{d_L d_S}} \tag{1.16}$$

where G is the gravitational constant, M is the mass of lens, c is the speed of light, and d_{LS}, d_L, and d_S are the distance between the lens and source, the distance to the lens, and the distance to the source, respectively. Physicist have found that the calculated mass is much larger than the mass that can be inferred from a cluster's luminosity.

1.5.3 Most Recent Evidence

To explain DM physicists have first turned to astrophysical objects made of baryonic matter. Possible "dark" candidates include brown dwarfs, neutron stars, black holes, and unassociated planets; all of these candidates can be classified as **MACHOs**, MAssive Compact Halo Objects.

To hunt for these objects two collaborations, the MACHO Collaboration (see Alcock

et al. 2000)and the EROS-2 Survey (see Derue et al. 1999), searched for **Gravitational Microlensing**, i.e. the changing brightness of a distant object due to the interference of a nearby object caused by possible MACHOs in the Milky Way halo. The MACHO Collaboration has extensively observed the skies for such lensing: millions of stars have been spotted with just few possible lensing events associated. This low number of possible MACHOs can only account for a very small percentage of the non-luminous mass in our galaxy, revealing that most DM cannot be strongly concentrated or exist in the form of baryonic astrophysical objects. Furthermore, the Big Bang nucleosynthesis and CMB observations give indication that other forms of baryonic matter cannot make up the majority of DM.

The **Big Bang nucleosynthesis** is a period from a few seconds to a few minutes after the Big Bang in the early Universe when neutrons and protons fused together to form deuterium, helium, and trace amounts of lithium and other light elements. Since any deuterium found or produced in stars is almost immediately converted into ^4He, the present abundance of deuterium in the Universe can be considered a "lower limit" on the amount of deuterium created by the Big Bang. Therefore, by considering the **deuterium to hydrogen ratio** of distant, primordial-like areas with low levels of elements heavier than lithium, physicists are able to estimate the D/H abundance directly after the nucleosynthesis. It turns out that the D/H ratio is heavily dependent on the overall density of baryons in the Universe, so measuring the D/H abundance gives the overall baryon abundance. This is usually represented by $\Omega_b h^2$, where b is the baryon density relative to a reference critical density (ρ_c) and $h = H/100\,\mathrm{kms}^{-1}\mathrm{Mpc}^{-1}$ the reduced Hubble constant. Calculations (see Cyburt 2004) show that the baryon density can accounts for only about 20% of the total matter density.

The **CMB** is another way in which we can learn about the composition of the Universe. The COsmic Background Explorer (COBE, launched in 1989) was the first space mission that verified two fundamental properties of the CMB: 1) it's high uniformity (2.73 K across the sky) and 2) the CMB, and thus the early Universe, is a nearly perfect blackbody (see figure 1.7). Despite the uniformity, the Differential Microwave Radiometer (DMR) onboard COBE discovered in its first year fundamental fluctuations (**anisotropies**) within the CMB, beyond the signal due to our motion relative to the CMB frame and foregrounds, such as emission from dust in the Milky Way. Anisotropies are due to two different effects:

- **large scale fluctuations** can be attributed to the Sachs-Wolfe effect: lower energy photons are observed today from areas that were more dense at the time of last scattering (these photons, once emitted, lost energy escaping from deeper gravitational potential wells)
- on **small scales**, the origin of the CMB anisotropies are due to what are called **acoustic oscillations**. Before photon decoupling, protons and photons can be modeled as a photon-baryon fluid (since electrons are so much less massive than baryons we can effectively ignore them here). This fluid effectively goes through the following cycle:
  1. the fluid is compressed as it falls into a gravitational well,
  2. the pressure of the fluid increases until it forces the fluid to expand outward,
  3. the pressure of the fluid decreases as it expands until gravity pulls it back,

4. the process repeats until photon decoupling.

Depending on the location in the cycle for a portion of the fluid at photon decoupling, the photons which emerge vary in temperature. The fluctuations in the CMB are thus indications of both the initial density perturbations that allowed for the formation of early gravitational wells as well as dynamics of the photon-baryon fluid.

In this manner the temperature fluctuations of the CMB are dependent on the amount of baryons in the Universe at the time of recombination. Although the detection of the fluctuations in the CMB was a major accomplishment, the magnitude of the temperature variations puzzled scientists. These fundamental fluctuations in the CMB are incredibly small, only about $30 \pm 5\mu$K, meaning that the CMB is uniform to 1 part in 10^5. In fact, these fluctuations were too small to have solely accounted for the seeds of structure formation; essentially, given the size of the CMB fluctuations, the structure of the Universe we see today would not have had time to form. The problem is time: ordinary matter only becomes charge neutral at the epoch of recombination, and before that, due to electrostatic forces, matter cannot effectively clump into gravitational wells to begin forming structure. The COBE results showed a need for an electrically neutral form of matter that could jump start the structure formation process well before recombination.

The Planck probe of the European Space Agency was launched in 2009 with the mission to measure the anisotropies in the CMB with increased precision (see figure 1.7) with respect to COBE and its follower WMAP (Wilkinson Microwave Anisotropy probe). Located at the Earth-Sun L2 point (about a million miles from Earth), the satellite acquired data continuously for 4 years and revealed a baryonic matter density equal to

$$\Omega_m h^2 = 0.1415 \pm 0.0019, \Omega_b h^2 = 0.02226 \pm 0.00023 \tag{1.17}$$

where $\Omega_m h^2$ is the total matter density, and $\Omega_b h^2$ is the baryonic matter density. Since these quantities are different we can deduce, at least, that baryonic matter is not the only form of matter in the Universe.

Analyses of the **large scale structure of the Universe** also yield evidence for DM and help break degeneracies present in the CMB data analysis. By calculating the distance to galaxies using their redshifts, cosmologists have been able to map out the approximate locations of more than 1.5 million galaxies. For example, the Sloan Digital Sky Survey (SDSS) has created 3-D maps of more than 900,000 galaxies, 120,000 quasars, and 400,000 stars during its eight years of operation (see Abazajian et al. 2009). The current structure in the Universe is due to initial density fluctuations which served as seeds for structure formation magnified by the presence of DM.

The most likely source of these initial density perturbations are quantum fluctuations magnified by inflation (see section 1.4). Under the assumption that these random fluctuations are Gaussian, a single function, the power spectrum P(k), is sufficient to describe the density perturbations. From here a given P(k) can be used to theoretically calculate large scale structure. These statements are true, of course, only statistically. Furthermore, the converse is also true: by measuring large scale structure (galaxy counts and surveys) one can experimentally determine the power spectrum P(k).

By obtaining the matter power spectrum from galaxy surveys, the amount of total mat-

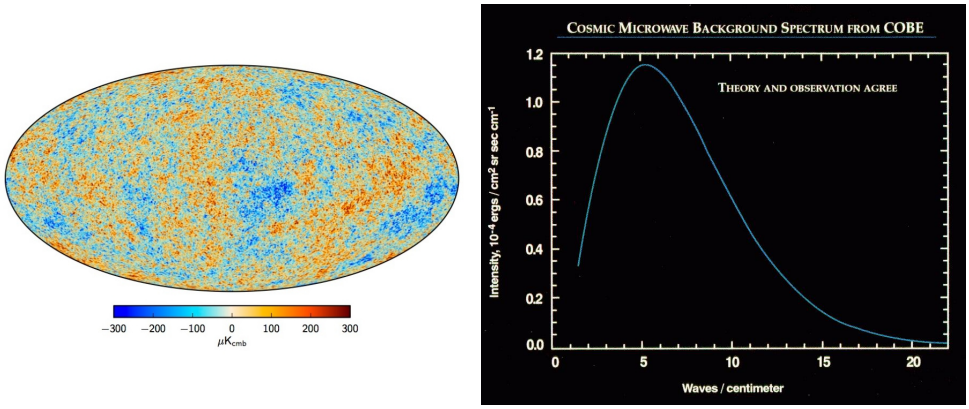

Figure 1.7: ***Left****: Maximum posterior CMB intensity map at 5′ resolution derived from the joint baseline analysis of Planck, WMAP, and 408 MHz observations. A small strip of the Galactic plane, 1.6% of the sky, is filled in by a constrained realization that has the same statistical properties as the rest of the sky (see Adam et al. 2016)* ***Right****: CMB spectrum plotted in waves per centimeter vs. intensity. The solid curve shows the expected intensity from a single temperature blackbody spectrum, as predicted by the hot Big Bang theory. A blackbody is a hypothetical body that absorbs all electromagnetic radiation falling on it and reflects none whatsoever. The FIRAS data were taken at 43 positions equally spaced along this curve. The FIRAS data match the curve so exactly, with error uncertainties less than the width of the blackbody curve, that it is impossible to distinguish the data from the theoretical curve. Credits:* `https://lambda.gsfc.nasa.gov/product/cobe/firas_image.cfm`

ter and baryonic matter can be found: the peak of P(k) is sensitive to the value of Ω_m, and the amount of baryons has effects on the shape of P(k) (through baryon acoustic oscillations, i.e. excesses in galaxies separated at certain distances due to sound waves in the pre-recombination plasma). Using these techniques, a final study of the 2dF Galaxy Redshift Survey power spectrum found

$$\Omega_m = 0.231 \pm 0.021, \Omega_b/\Omega_m = 0.185 \pm 0.046 \tag{1.18}$$

and a study based on data from SDSS yielded

$$\Omega_m = 0.286 \pm 0.018, \Omega_b/\Omega_m = 0.185 \pm 0.046 \tag{1.19}$$

Note that these results agree with both CMB and Big Bang nucleosynthesis predictions.

Recent strong evidence for dark matter comes from the **Bullet cluster**, the result of a subcluster colliding with a larger galaxy cluster. During the collision, the galaxies within the two clusters passed by each other without interacting. However, the majority of a cluster's baryonic mass exists in the extremely hot gas between galaxies, and the cluster collision compressed and shock heated this gas. A huge amount of X-ray radiation was emitted which has been observed by NASA's Chandra X-ray Observatory (see figure 1.8). Comparing the location of this radiation (an indication of the location of the majority of the baryonic mass in the clusters) to a mapping of weak gravitational lensing (an indication of the location of the majority of the total mass of the clusters) shows an interesting discrepancy; the areas of strong X-ray emission and the largest concentrations of mass seen through gravitational lensing are not the same. The majority of the mass in the clusters is non-baryonic and gravity "points" back to this missing mass.

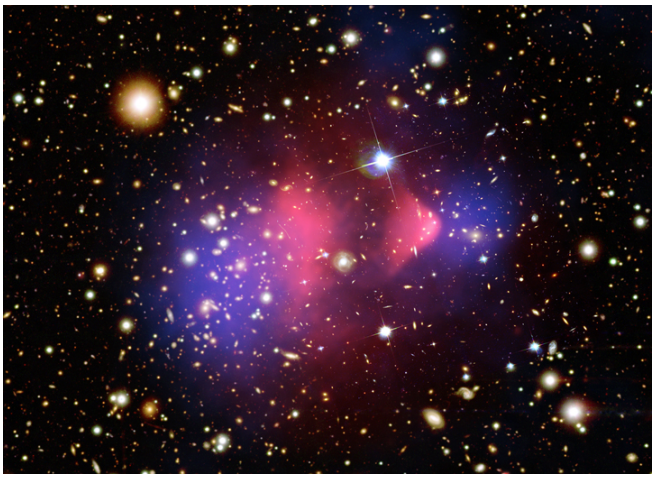

Figure 1.8: This composite image shows the galaxy cluster 1E 0657-56, also known as the "bullet cluster". This cluster was formed after the collision of two large clusters of galaxies, the most energetic event known in the Universe since the Big Bang. Hot gas detected by Chandra in X-rays is seen as two pink clumps in the image and contains most of the baryonic matter in the two clusters. The bullet-shaped clump on the right is the hot gas from one cluster, which passed through the hot gas from the other larger cluster during the collision. An optical image from Magellan and the Hubble Space Telescope shows the galaxies in orange and white. The blue areas in this image show the highest mass concentration in the clusters. The concentration of mass is determined using the gravitational lensing effect, where light from the distant objects is distorted by intervening matter. Most of the matter in the clusters (blue) is clearly separate from the normal matter (pink), giving direct evidence that nearly all of the matter in the clusters is dark. Credits: X-ray: NASA/CXC/CfA/M.Markevitch et al.; Optical: NASA/STScI; Magellan/U.Arizona/D.Clowe et al.; Lensing Map: NASA/STScI; ESO WFI; Magellan/U.Arizona/D.Clowe et al.

It has been shown that the existence of dark matter is well motivated by several lines of evidence. Nevertheless, the exact nature of dark matter remains elusive. Dark matter candidates are generically referred to as WIMPs (Weakly Interacting Massive Particles); in other words, they are massive particles that are electrically neutral which do not interact very strongly with other matter. The Standard Model (SM) in the quantum field theory does not contain any particle that could act as the dark matter. This does not invalidate the SM, but rather suggests that it must be extended. One possible extension to the Standard Model is an additional symmetry between fermions and bosons - the so called "supersymmetry" (SUSY). The new particles generated by adding SUSY to the SM are the neutralinos, charginos and gluinos, and among them there are several possible particles which could act as dark matter. These are the neutralino (a particle state which is a superposition of the neutral superpartners of the Higgs and gauge bosons), the sneutrino (the superpartner of the neutrino), and the gravitino (the superpartner of the graviton which would come from a quantum theory of gravity). All of these particles are electrically neutral and weakly interacting, and thus are ideal WIMP-like candidates for dark matter. However, sneutrinos annihilate very rapidly in the early Universe, and sneutrino relic densities are too low to be cosmologically significant. Gravitinos are too fast, so they act more like hot dark matter rather than cold dark matter, and large scale structure observations are inconsistent with a Universe dominated by hot dark matter. This leaves the neutralino as a viable candidate, even if, at the moment, not one super-

symmetric particle has been detected in the laboratory.

Other particle candidates for dark matter also exist. They are more exotic candidates like the axion, the Lightest Kaluza-Klein particle, Q-balls, WIMPzillas, branons, and GIMPs among many others. However, the neutralino remains the most studied and most theoretically motivated dark matter candidate.

1.6 Dark Energy and the Accelerating Universe

The first Friedmann equation (see 1.5) tells us that the positive cosmological constant Λ contributes positively to the background energy density and negatively to pressure. It can be thought as a perfect fluid with

$$\rho_\Lambda = \frac{\Lambda}{8\pi G}, P_\Lambda = -\frac{\Lambda}{8\pi G} \tag{1.20}$$

which corresponds to $\omega_\Lambda = -1$. The simplest candidate of dark energy is provided by the cosmological constant with $\Omega_\Lambda = -1$. Observations at present do not rule out the *phantom* dark energy with $\omega < -1$ corresponding to super acceleration.

Apart from the cosmic acceleration, dark energy has important implications, in particular, in relation to the age problem. In any cosmological model with normal form of matter, the age of Universe falls short compared to the age of some known objects in the Universe. Since the age of Universe crucially depends upon the expansion history, it can serve as an important check on the model building in cosmology. In particular, the study of large scale structure and its dynamics constrain the matter density: $0.2 < \Omega_m^{(0)} < 0.3$ and observations on CMB anisotropy reveal that Universe is critical to a good accuracy. The age problem can be resolved in a flat Universe dominated by dark energy. We can rewrite the first Friedmann equation in a convenient form

$$\left(\frac{\dot{a}}{a}\right)^2 = H_0^2[\Omega_m^{(0)}\left(\frac{a_0}{a}\right)^3 + \Omega_{DE}^{(0)}\left(\frac{a_0}{a}\right)^{3(1+w)}] \tag{1.21}$$

which allow us to write the expression of the age of the Universe as

$$t_0 = \frac{1}{H_0^2}\int_0^\infty \frac{\mathrm{d}z}{(1+z)[\Omega_m^{(0)}(1+z)^3 + \Omega_{DE}^{(0)}(1+z)^{3(1+\omega)}]^{1/2}} \tag{1.22}$$

where $\Omega_m^{(0)}$ is the contribution of dark matter and $(1+z) \equiv a_0/a, z$ being the redshift parameter. In case dark energy is cosmological constant, we get the analytical expression for the age of Universe

$$t_0 = \frac{2}{3}\frac{H_0^{-1}}{\Omega_\Lambda^{1/2}} \ln\left(\frac{1+\Omega_\Lambda^{1/2}}{\Omega_m^{(0)1/2}}\right) \tag{1.23}$$

The direct evidence of current acceleration of Universe is related to the observation of luminosity distance by high redshift supernovae. At the end of the 1990's observations of type Ia supernovae (SNe) at distances of about 6 billion light years by two independent

research groups, led by S. Perlmutter - the "**Supernova Cosmology Project**", (see Perlmutter et al. 1999)) - and by B. Schmidt and A. Riess - the "**High-Z Supernova Search**" (see Riess et al. 1998))-, respectively, reveal that presently the expansion rate of the Universe is accelerating.

The luminosity distance for a critical Universe dominated by non-relativistic fluid and cosmological constant is given by

$$d_L = \frac{(1+z)}{H_0} \int_0^z \frac{\mathrm{d}z'}{\sqrt{\Omega_m^{(0)}(1+z')^3 + \Omega_{DE}^{(0)}(1+z')^{3(1+\omega)}}} \tag{1.24}$$

Equation 1.24 is the expanding Universe generalization of absolute luminosity L_S of a source and its flux F at a distance d given by $F = L_S/(4\pi d^2)$. From the same equation it is possible to see that $D_L \cong z/H_0$ for small z and that

$$d_L = 2[1 + z - (1+z)^{1/2}]H_0^{-1}, \Omega_m^{(0)} = 1 \tag{1.25}$$

$$d_L = z(1+z)H_0^{-1}, \Omega_{DE}^{(0)} = \Omega_\Lambda = 1 \tag{1.26}$$

which means that luminosity distance at high redshift is larger in a universe dominated by the cosmological constant which also holds true in general for an arbitrary equation of state corresponding to dark energy. Therefore supernovae would appear fainter in case the Universe is dominated by dark energy.

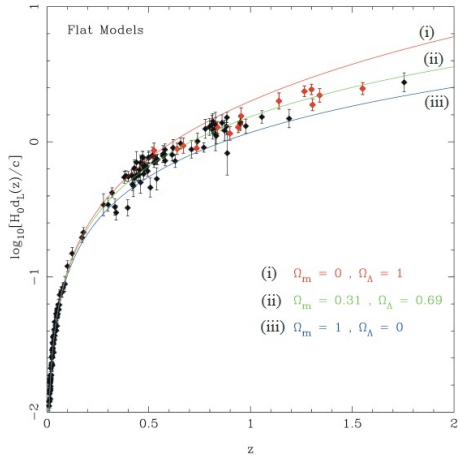

Figure 1.9: Plot of the luminosity distance $H_0 d_L$ versus the redshift z for a flat cosmological model. The black points come from the "'gold"' data sets by Riess et al. (see Riess et al. 2004); red points show data from Hubble Space Telescope. Three curves show the theoretical values of $H_0 d_L$ for (i) $\Omega_m^{(0)} = 0, \Omega_\Lambda = 1$, (ii) $\Omega_m^{(0)} = 0.31, \Omega_\Lambda = 0.69$ and (iii) $\Omega_m^{(0)} = 1, \Omega_\Lambda = 0$. Credits: (see Choudhury & Padmanabhan 2005).

The existence of a dark energy field with negative pressure leads to a cosmic expansion which is accelerating at the present time. Since this surprising discovery many observational efforts have been performed to accurately measure the cosmological parameters

over as large a fraction of the age of the Universe as possible, especially over the redshift interval $0 < z < 1.5$ which, according to current estimates (see figure 1.9), covers the deceleration-acceleration transition. These efforts include large surveys of galaxy large scale structure, galaxy clusters, weak lensing, baryon acoustic oscillation (BAO), the Lyman alpha forest, and high redshift supernovae, all of which span the relevant redshift range. Except for the supernovae, all other techniques rely on measurements of cosmological structure in order to deduce cosmological parameters.

The observations related to CMB and large scale structure (LSS) provide, indeed, an independent confirmation of the dark energy scenario. The acoustic peaks of the angular power spectrum of CMB temperature anisotropies (see figure 1) contain important information about curvature and energy contents of the Universe. The acoustic peaks occur because the cosmological perturbations excite sound waves in the relativistic plasma of the early Universe.

The recent data on Baryon Acoustic Oscillation (BAO) (see figure 1.10 and Introduction) is yet another independent probe of dark energy. BAO are frozen relics left over from the pre-decoupling Universe, and they can be exploited as standard rulers for cosmology, providing distance estimates that comes from well understood physics. The recombination to a neutral gas at decoupling era abruptly decreases the sound speed and effectively ends the wave propagation. In the time between the formation of the perturbations and the epoch of recombination, modes of different wavelength can complete different numbers of oscillation periods. This translates the characteristic time into a characteristic length scale and produces a harmonic series of maxima and minima in the anisotropy power spectrum. Because the Universe has a significant fraction of baryons, cosmological theory predicts that the acoustic oscillations in the plasma will also be imprinted onto the late-time power spectrum of the non-relativistic matter. Indeed, it must be considered that from an initial point perturbation common to the dark matter and the baryons, the dark matter perturbation grows in place while the baryonic perturbation is carried outward in an expanding spherical wave (since baryon and radiation are coupled). At recombination, this shell is roughly 150 Mpc in radius. Afterward, the combined dark matter and baryon perturbation seeds the formation of large scale structure. Because the central perturbation in the dark matter is dominant compared to the baryonic shell, the acoustic feature is manifested as a small single spike in the correlation function at 150 Mpc separation. The acoustic signatures in the large scale clustering of galaxies offer three more opportunities to test the cosmological paradigm with the early Universe acoustic phenomenon:

1. they would provide smoking-gun evidence for the theory of gravitational clustering (i.e the idea that large-scale fluctuations grow by linear perturbation theory from $z \cong 1000$ to the present
2. they would give another confirmation of the existence of dark matter at $z \cong 1000$, since a fully baryonic model produces an effect much larger than observed
3. they would provide a characteristic length scale that can be measured at a wide range of redshifts, thereby determining purely by geometry the angular diameter–distance–redshift relation and the evolution of the Hubble parameter

We saw in section 1.4 that the standard cosmological model asserts that the **largest structures** that we observe today (i.e. galaxies and clusters of galaxies) grew out of small initial fluctuations that were seeded during the phase of inflationary expansion. Most of

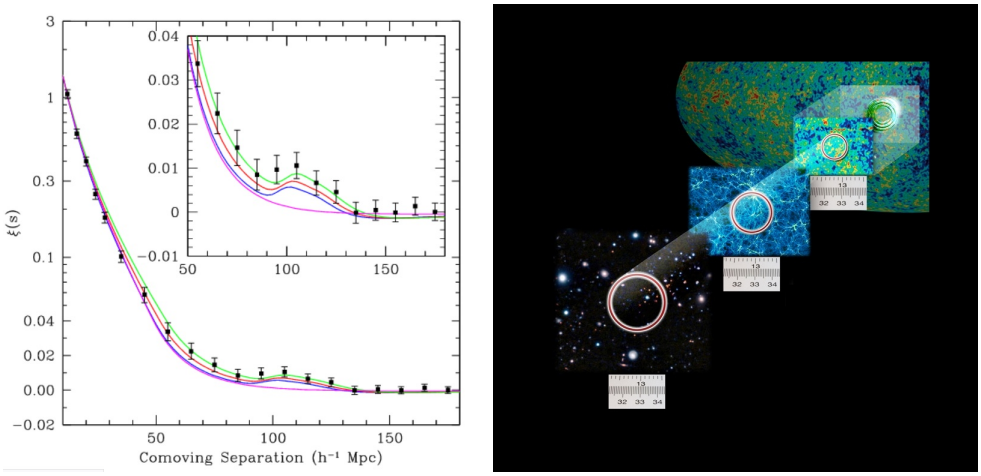

Figure 1.10: ***Left****: the Baryon Acoustic Peak (BAP) in the correlation function. The BAP is visible in the clustering of the SDSS Luminous Red Galaxy sample, and is sensitive to the matter density. Shown are models with* $\Omega_m h^2 = 0.12$ *(green),* $\Omega_m h^2 = 0.13$ *(red),* $\Omega_m h^2 = 0.14$ *(blue), all with* $\Omega_b h^2 = 0.024$*. The pink line without a BAP is the correlation function in the pure* Λ*CDM model, which lacks the acoustic peak. Credits: (see Eisenstein et al. 2005)* ***Right****: the tight coupling between photons and baryon in the hot thermal plasma, which is the remnant left over from the Big Bang, imprints a characteristic length scale onto the distribution of galaxies – the so-called baryon acoustic oscillation (BAO) scale. By using the BAO scale inferred from the measured galaxy distribution as a standard ruler, we are able to determine the cosmological distances to redshift of the galaxies, and a probe, then, of the Universe with which we can explore the nature of the cosmic acceleration. Credits:* `http://sumire.ipmu.jp/en/3002/`

the growth occurred after the decoupling of photons and electrons, since the Universe was mostly matter-dominated at that point. The smaller structures form first, while the largest structures form the latest. Hence, observations in various wavelengths can probe the full evolution of the formation of structure in the Universe, from when the first objects formed until today. Observations of the growth of structure provide a wealth of information about dark matter and dark energy. In particular, the scaling of the amplitude of growth vs. cosmic time (the so-called **growth function**) sensitively constrains dark energy parameters in a way that is complementary to distance measurements.

The temporal evolution of the growth is now readily observed by measuring the clustering of galaxies at multiple redshifts, and in the near future gravitational lensing has the potential to measure the same quantity but with the added advantage that it is directly sensitive to the growth of dark matter structures (as opposed to galaxies or other baryonic tracers such as hydrogen in the inter-galactic medium). Our ability to observe and model both the growth and the cluster counts have significantly improved over the past decade, and these two probes now provide constraints on dark energy that are complementary to distance measurements by type Ia supernovae, BAO, and CMB. New observations are expected over the next two decades. They include ground imaging surveys (e.g. DES and LSST), redshift surveys (e.g. eBOSS, PFS and DESI) and space surveys (e.g. Euclid and WFIRST). The combination of these surveys will provide high-precision measurements of the growth of structure out to redshift of a few and across most of the sky. These measurements will, in turn, strongly constrain the equation of state of dark energy and, more generally, the expansion history of the Universe over the past 10 bil-

lion years.

In the linear theory (valid at early times and large enough spatial scales) the matter density contrast $\delta = \delta\rho_m/\rho_m$ evolves independently of the spatial scale k (see equation 1.8). The growth of fluctuations in time can be obtained by solving the equation

$$\ddot{\delta} + 2H\dot{\delta} - 4\pi G\rho_m\delta = 0 \tag{1.27}$$

where H is the Hubble parameter, and dots are derivatives with respect to time t. Therefore, in standard General Relativity and in the linear regime ($|\delta| << 1$), obtaining the linear growth of fluctuations as a function of time is straightforward given the composition and the expansion rate of the Universe. The *linear growth function D(a)* can be defined in term of the scale factor a as

$$\delta(a) = D(a)\delta(a = 1) \tag{1.28}$$

or equivalently in redshift z where $1 + z = 1/a$. If General Relativity is replaced by some modified gravity theory, then equation 1.27 changes: the evolution of growth will be re-derived in the new theory, and linear growth rate D may depend on scale k as well (see figure 1.11).

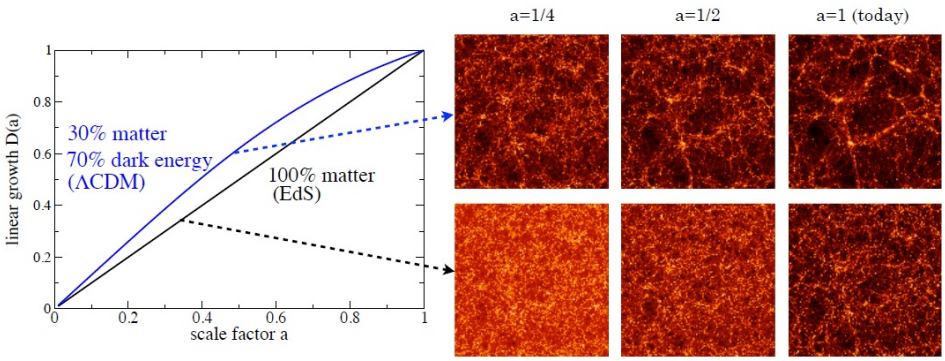

Figure 1.11: Growth of structure at large spatial scales in the Universe. ***Left panel****: because dark energy suppresses the growth of structure, the linear growth $D(a)$, which is normalized to unity today, had to be larger in the past in the currently favored model with dark energy (; blue line) than in the Einstein-de Sitter model (EdS; black line) which has matter only and no dark energy.* ***Right panel****: snapshots from numerical (N-body) simulations by the Virgo consortium (see Jenkins et al. 1998), showing larger amplitude of density fluctuations in the past in (top row) than in the EdS model (bottom row given an approximately fixed amount of clustering today. Accurate measurements of the clustering as a function of spatial scale and cosmic time can therefore stringently constrain the cosmological model. Credits:* `http://inspirehep.net/record/1254984/plots#0`

The physics behind the observed accelerated expansion of the Universe is widely recognized as one of the most profound outstanding problems in fundamental science. When interpreted in terms of our current understanding of gravity, Einstein's General Relativity, this requires adding an additional, exotic component to the cosmic energy budget

with a negative pressure, which we now refer to as dark energy. The minimalist explanation is to invoke a very small cosmological constant. However, within our current understanding of quantum theory, such a value of the cosmological constant is extremely unnatural. Instead, one can invoke a very light scalar field, whose potential energy then drives the accelerated expansion of the Universe. In fact, this is precisely the mechanism deduced to have produced inflation, which, in turns, allowed the Universe to grow to its observed large size. The same mechanism provided the seed fluctuations for the structure within the Universe itself.

As a fundamental alternative to dark energy, one can ask whether the acceleration of the Universe is caused by a modification of gravity on large scales, i.e. departure from General Relativity, rather than an exotic form of energy. This possibility has generated a significant amount of theoretical work over the past decade; and generated the so-called f (R) gravity, scalar-tensor theories (see Perrotta et al. 2000), and braneworld models (see Sahni & Shtanov 2003).

Furthermore, answering the above question, provides strong motivation to search for and constrain modifications to General Relativity using cosmological observations. However, modifying relativity on large scales in a consistent way is extremely difficult, due to both theoretical issues and a broad set of observational constraints. In particular, any theory of gravity has to reduce to relativity within the Solar System to satisfy stringent local tests of gravity; furthermore, CMB and the Big Bang nucleosynthesis provide constraints in the early Universe. Both of these constraints can be satisfied by invoking non-linear "screening mechanisms" which restore relativity in high density regions.

CHAPTER 2

The Search for Dark Matter and Dark Energy

2.1 Introduction

Section 1 offered a deep review of our present knowledge of the Universe from the point of view of its constituents. Today we know that most of the matter in the Universe is not luminous and can be observed only through its gravitational effect. Early indications of the existence of a "dark matter" came from the comparison of the mass of a cluster of galaxies deduced from the velocity dispersion of cluster components and from the mass-to-luminosity ratio (see section 1.5.1).

The **cosmic microwave background radiation**, observed in the 1960s, is another indirect proof of the existance of dark matter. The temperature anisotropies detected in this relic radiation offer a snapshot of the irregularities in the matter distribution when the Universe was only 380,000 years old. These anisotropies are the seeds from which, gravitationally, originated the structures (galaxies and cluster of galaxies) we observe today in the Universe. So comparison of the CMB-derived mass spectrum with that seen at later times will be a powerful test of cosmology.

In the 1970s, a more direct way to probe the amount and distribution of dark matter was discovered: the gravitational lensing, that uses background galaxies to reveal the foreground matter distribution on large scales. Any foreground mass bends light rays from a distant source, moving the apparent position of the source to a new position on the sky and stretching its image tangentially, by an amount proportional to the foreground mass. The **weak lensing effect** has already been used to study the mass distribution within clusters of galaxies, where the large mass associated with the clusters makes the gravitationally induced ellipticity of the background galaxies easily detectable.

In principle, weak lensing can also tell us about large-scale structure through the cumulative effect of many intervening overdensities. A deep image of a patch of the sky maps through the three-dimensional forest of galaxies seen in projection. Light rays from distant galaxies travel a tortuous path through a universe filled with clustering dark mass. Every bend in the path of a bundle of light from a distant galaxy stretches its apparent image. The orientation of the resulting elliptical images of galaxies contains information on the size and mass of the gravitational lenses distributed over the light path (see figure 2.1). Different cosmological models predict different behavior for correlations of galaxy

ellipticities versus angle on the sky.

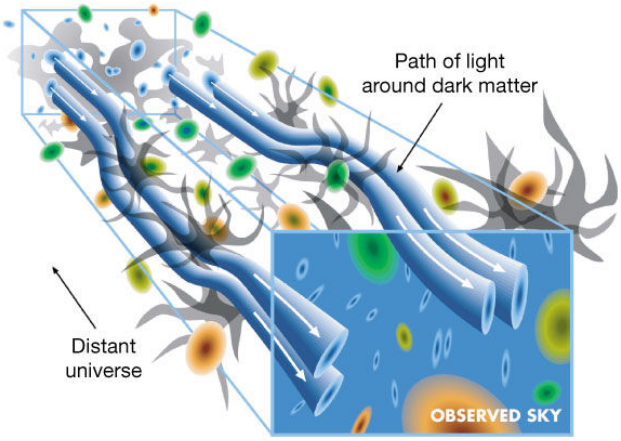

Figure 2.1: "The figure shows a schematic view of weak gravitational lensing by large-scale mass structure: distant galaxy orientation is correlated on scales characteristic of the lensing dark matter structures. Light bundles from two distant galaxies which are projected closely together on the sky follow similar paths and undergo similar gravitational deflections by intervening dark matter concentrations. Apparent orientations of distant galaxies are thus correlated on angular scales of less than a few degrees. The larger the mass in the gravitational deflectors, the larger the faint galaxy ellipticity correlations on a given angular scale. These ellipticity correlations of distant galaxies reveal the statistics of the large-scale dark matter distribution in the intervening universe - a central diagnostic of the underlying cosmology." Credits: (see Wittman et al. 2000)

The direct evidence of current acceleration of Universe come at the end of the 1990s through the observation of luminosity distance of high redshift supernovae. The existence of a "dark energy field" with negative pressure leads to a cosmic expansion which is accelerating at the present time. This discovery triggered many observational efforts to accurately measure the cosmological parameters, e.g large surveys of galaxy large scale structure, galaxy clusters, weak lensing, baryon acoustic oscillation (BAO), the Lyman alpha forest, and high redshift supernovae. Except for the supernovae, all other techniques rely on measurements of cosmological structure in order to deduce cosmological parameters.

Next sections will give details about the technical challenges related to weak gravitational lensing, large surveys of galaxy large scale structures and spectroscopic redshift surveys, including an overview of the experiments dedicated to the quest of the dark components of the Universe. Section 2.4 is entirely dedicated to the Euclid space mission.

2.2 Gravitational Lensing

Section 1.5.2 showed that the manifestation of gravitational lensing can be strong or weak, with additional features such as Einstein's rings, arcs and crosses that modify the

phenomenological study of effects of strong gravity.

The photons emitted from distant sources travel across the Universe to reach our telescopes and detectors. Their trajectories are perturbed by the inhomogeneous distribution of matter. Most sources appear to us slightly displaced and distorted in comparison with the way they would appear in a perfectly homogeneous and isotropic Universe. This phenomenon is called **weak gravitational lensing**. Under rare circumstances, the deflection caused by foreground mass overdensities such as galaxies, groups, and clusters is sufficiently large to create multiple images of the distant light source. This phenomenon is called **strong gravitational lensing**.

Three properties make strong gravitational lensing a most useful tool to measure and understand the Universe:

- strong lensing observables (e.g.relative positions, flux ratios, and time delays between multiple images) depend on the gravitational potential of the foreground galaxy
- the lensing observables also depend on the overall geometry of the Universe via angular diameter distances between observer, deflector, and source
- the background source often appears magnified to the observer, sometimes by more than an order of magnitude.

As a result, gravitational lensing can be used to address three major astrophysical issues:

1. understanding the spatial distribution of mass at kiloparsec and sub-kiloparsec scale where baryons and dark matter interact to shape galaxies as we see them
2. determining the overall geometry, content, and kinematics of the Universe
3. studying galaxies, black holes, and active nuclei that are too small or too faint to be resolved or detected with current instrumentation.

As far as 2010 approximately 200 examples of strong gravitational lensing by galaxies have been discovered (see T. Treu, "Strong Lensing by Galaxies", Annu. rev. Astron. Astrophys. 2010, 48:87-125) using different strategies. From a technological point of view it is not trivial to extract the information available from strong lensing systems. A demanding subarcsecond angular resolution, together with the source and lens redshifts are needed to identify the lensing systems, and to transform angular quantities into masses and lengths. Observations (preferably from space) in the radio or optical-near infrared part of the electromagnetic spectrum are then required, together with long exposures.

If the lens has a density which is below a critical value, then we have a **weak lensing** effect, i.e.a small distortion in the shape of a background galaxy that depends on the curvature of the foreground gravitational potential. Usually the signal produced by a single source is too weak. The presence of foreground structure can then be inferred by statistically analyzing the distorted shapes of background galaxies in a given direction, assuming that, on average, galaxies are randomly oriented.

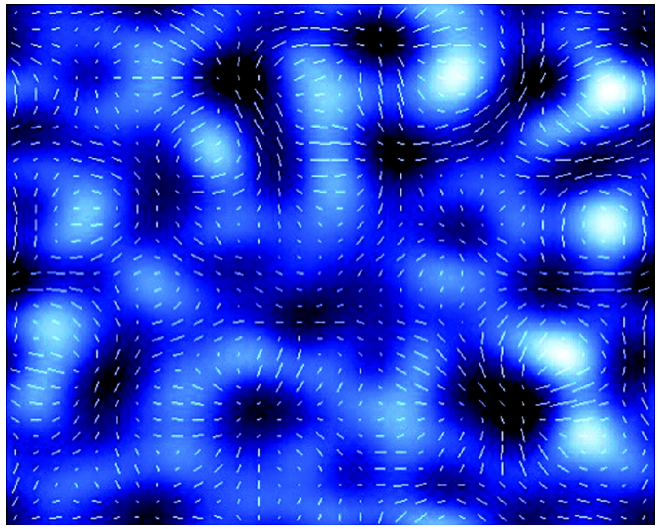

Figure 2.2: "An idealized illustration of weak gravitational lensing. The blue image represents the projected mass distribution in a given area of the sky (white indicates a higher projected density of dark matter). The white tick marks represent the average shapes and orientations of a population of faint galaxies (assumed statistically to be round in shape) viewed through the dark matter. Where the dark matter is concentrated, the background galaxies are tangentially aligned around the structure; where the dark matter density is weak, the galaxies are aligned radially. The pattern of background galaxies can be used to infer the (invisible) distribution of foreground dark matter." Credits: (see Ellis 2010)

2.2.1 Large Scale Lens Surveys

The two largest gravitational lens survey conducted to date are the **Cosmic Lens All-Sky Survey** (CLASS) (see Myers et al. 2003) and the **Sloan Lens ACS (SLACS) Survey** (see Bolton et al. 2006).

The Cosmic Lens All-Sky Survey (CLASS), is an international (USA, UK and Netherlands) collaborative project to map more than 10,000 radio sources in order to create the largest and best studied statistical sample of radio-loud gravitationally lensed systems. CLASS is aimed at identifying lenses where multiple images are formed from compact flat-spectrum radio sources. The lens configurations should be easily identifiable in the radio maps. Thus, CLASS is most efficient at finding galaxy-mass lenses (which will dominate the counts for surveys not targeted at clusters) with separations of around a few arcseconds.

The Very Large Array (VLA) is being used as the primary instrument for the CLASS survey, together with the Multi-Element Radio Linked Interferometer Network (MERLIN), and the Very Long Baseline Aarray, and resulted in 22 lens systems.

The SLACS survey is an efficient Hubble Space Telescope snapshot imaging survey for new galaxy-scale strong gravitational lenses. SLACS lens candidates are selected from within the spectroscopic database of the Sloan Digital Sky Survey (SDSS) for the presence of two galaxies along the same line of sight in the sky, one much more distant than the other. Such spectra occur with a frequency of only 1 in 500 to 1 in 1000, so a survey

such as the SDSS - with nearly a million galaxy spectra - is crucial to obtaining a statistically significant sample. Following this selection, the SLACS targets are observed with the Advanced Camera for Surveys (ACS) aboard the Hubble Space Telescope (HST). The exquisite angular resolution of the HST often reveals the image of the more distant galaxy distorted into a ring by the gravity of the nearer galaxy. The HST images allow us to measure the angular size of these Einstein rings, which in combination with the distances measured from the SDSS spectra provide direct measurements of the enclosed masses of the lens galaxies. These masses are then combined with measurements of the sizes, brightnesses, and stellar velocities of the lens galaxies to yield insights into their structure and evolution. The survey has been optimized to detect bright early-type lens galaxies with faint lensed sources, in order to increase the sample of known gravitational lenses suitable for detailed lensing, photometric, and dynamical modeling.

Some of the major results of the survey includes:

1. the radial mass density profile of the SLACS lenses is inconsistent with a model wherein the optical light traces mass
2. this radial mass density profile is approximately "isothermal" (i.e. density proportional to the inverse square of radius in three dimensions)
3. in combination with previous results, this profile seems not to have evolved significantly since redshift $z = 1$

The SLACS survey (2003-2010) has discovered about 100 new lens systems and obtained a large number of solid scientific results, e.g. measurements of the Hubble constant H_0, strong constraints on galaxy density profiles and their evolution, micro-lensing by stars in galaxies, possibly a first indication of CDM substructure through flux-ratio anomalies. Many of these studies are limited by the relatively small suitable sample sizes (dozens), and several orders of magnitude more suitable lens systems are required.

Major radio and optical-IR survey telescopes are planned to become operative in the next years, with the ability of gathering large samples of galaxy-scale lenses and opening a new discovery space: e.g. in the optical the Large Synoptic Survey Telescope (under construction on the summit of Cerro Pachón, Chile) could yield 10^4 new lenses. In the radio the Expanded Very Large Array (EVLA), e-MERLIN, using e.g. LOFAR for preselection, could gather about 10^2 lenses within the next years, and from the 10% SKA in phase-I one expects 10^3 and up to 10^5 lenses as well.

2.3 Wide Field Imaging and Spectroscopic Redshift Surveys

One way to explain the acceleration of the Universe (see section 1.1) is to invoke dark energy parametrized by an equation of state ϖ_{DE}. Distance measurements provide one set of constraints on ϖ_{DE}, but dark energy also affects how rapidly structure grows: the greater the acceleration, the more suppressed the growth of structure. Upcoming surveys are therefore designed to probe ϖ_{DE} with direct observations of the distance scale and the growth of structure.

Observations of the growth of structure provide a wealth of information about dark matter and dark energy. The **growth function** (i.e. the scaling of the amplitude of growth

vs. cosmic time) constrains dark energy parameters in a way that is complementary to distance measurements. The temporal evolution of the growth is now readily observed by measuring the clustering of galaxies at multiple redshifts, and in the near future gravitational lensing has the potential to measure the same quantity but with the added advantage that it is directly sensitive to the growth of dark matter structures. Furthermore, the cluster of galaxies measured as a function of their mass and redshift, is another probe of cosmological parameters.

The growth of structure and the observation of cluster of galaxies are two probes that provide constraints on dark energy that are complementary to distance measurements by type Ia supernovae, baryon acoustic oscillations, and the CMB (see section 1.1).

Another possibility is that there is no dark energy, but that General Relativity does not describe the laws of physics accurately on large scales. So future experiments should deal also with the possibility to determine whether the acceleration of the Universe is due to dark energy or to modified gravity.

In the forthcoming years new observation are expected, including:

- **ground imaging**, performed, for instance, by the Dark Energy Survey (DES), and the already cited Large Synoptic Survey Telescope (LSST). DES is an on-going, five year survey that, when completed, will map 300 million galaxies and tens of thousands of galaxy clusters in five photometric bands (g, r, i, z and Y) over 5000 deg^2 (see Abbott et al. 2017). The experiment began searching the Southern skies on August 31, 2013. DES uses the 570-megapixel Dark Energy Camera - DECam (see Flaugher et al. 2015) built by the collaboration and deployed on the Cerro Tololo Inter-American Observatory (CTIO) 4m Blanco telescope in Chile, to image the South Galactic Cap. The characteristic 10σ limiting magnitude for galaxies is 23.4 in the g band.

  The Large Synoptic Survey Telescope is an under-construction facility. According to the actual schedule, the telescope will be fully operative at the beginning of 2023 (see `https://www.lsst.org/about/project-status`). LSST will have an effective aperture of 6.7 meters and an imaging camera with field of view of 9.6 deg^2, and will be devoted to a ten-year imaging survey over 20,000 deg^2 south of $+15$ deg (see Abell et al. 2009). Each pointing will be imaged 2000 times with fifteen second exposures in six broad bands from 0.35 to 1.1 microns. LSST will explore properties of supernovae to $z \cong 1$, strong and weak lensing, the large-scale distribution of galaxies and BAO.

- **redshift surveys**, like those that will be performed by the Extended Baryon Oscillation Spectroscopic Survey (eBOSS), and the Dark Energy Spectroscopic Insrument (DESI). The extended Baryon Oscillation Spectroscopic Survey (eBOSS) is a redshift survey within SDSS-IV, observations for which started in July 2014 (see Zhao et al. 2016). The eBOSS cosmology program uses the same 1000-fiber optical spectrographs installed on the 2.5 m-aperture Sloan Foundation Telescope at the Apache Point Observatory (APO) in New Mexico, used for the Baryon Oscillation Spectroscopic Survey (BOSS of SDSS-III. eBOSS will map the Universe over the redshift range $0.6 < z < 2.2$ by observing multiple tracers including luminous red galaxies (LRGs) over 7000 deg^2, emission line galaxies (ELGs) and quasars.

DESI is an under-construction, multi-fiber spectroscopic instrument that will be installed on the Mayall 4-m telescope to enable massively parallel measurements of galaxy redshifts (see Levi et al. 2013). The survey will operate from 2018 through 2022, and it will cover 14,000 - 18,000 deg^2. DESI targets are LRGs, ELGs and quasars including Ly-α forest. The experiment will observe 20-30 million galaxies and quasars for $0.5 < z < 3.5$. Its spectroscopic resolution will be sufficient for redshift error $< 0.001(1 + z)$. The power of DESI is in both the precision and the wide range of redshifts it will cover, making it competitive even with the Euclid space-based mission.

- **space surveys**, that will be performed by Wide Field InfraRed Survey Telescope (WFIRST) and Euclid (see section 2.4). WFIRST is a NASA observatory that will use an existing 2.4-meter telescope hardware, along with heritage instrument, spacecraft, and ground system architectures and hardware (see Content et al. 2013). The payload is composed of a wide-field instrument and an optional coronograph. The wide-field instrument includes two channels, a wide-field channel and an integral field unit (IFU) spectrograph channel. The wide-field channel includes three mirrors and a filter/grism wheel to provide an imaging mode covering 0.76 – 2.0 μm and a spectroscopy mode covering 1.35 – 1.95 μm. The wide-field focal plane HgCdTe detectors arranged in a 6×3 array, providing an active area of 0.281 deg^2

The combination of these observations will provide high-precision measurements of the growth of structure out to redshift of most of the sky. These measurements will, in turn, strongly constrain the equation of state of dark energy and, more generally, the expansion history of the Universe over the past 10 billion years.

2.4 The Euclid Space Mission

Euclid is a Medium Class space mission of the European Space Agency belonging to the Cosmic Vision 2015-2025 programme. The spacecraft will be carried out into a direct transfer orbit by a Soyuz ST 2-1b launch vehicle from Europe's spaceport located in French Guaiana. The target orbit, from which Euclid will observe the sky, is a large amplitude *halo orbit* around the second Sun-Earth Lagrangian point L2. This point is situated approximately 1.5 million kilometers from the Earth, and from this point Euclid can observe the sky being undisturbed from our star (see figure 2.3). Currently the launch is foreseen in 2021.
The nominal mission duration is 6 years and the observations will be done in step-and-stare mode. Image dithering will be achieved at spacecraft level to fill detector gaps and allow correction for cosmic rays (see section 2.4.5).

2.4.1 Mission Science Case

Euclid is an ESA mission to map the geometry of the dark Universe, trying to cope with questions about the nature of dark energy and dark matter discussed in section 1.1 like:

- is dark energy a merely cosmological constant?
- is dark energy instead a manifestation of a break-down of General Relativity and deviations from the law of gravity?

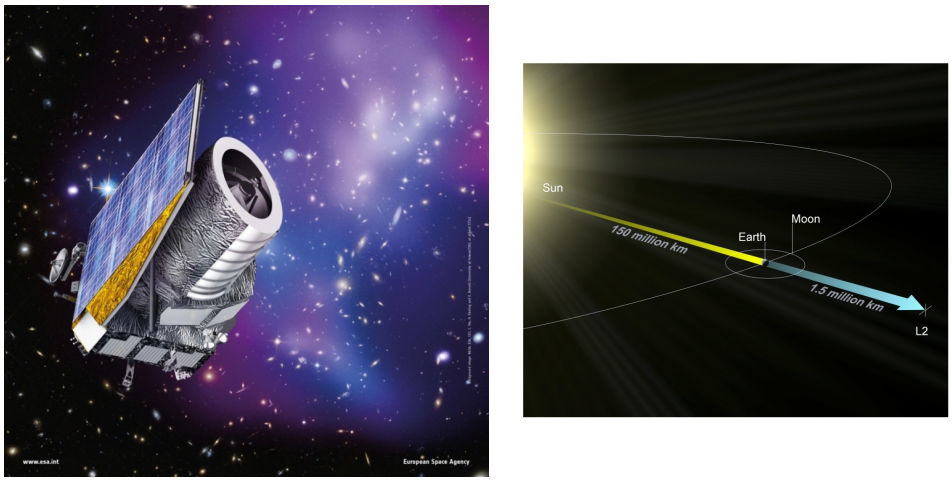

Figure 2.3: ***Left****: an artist view of the Euclid Satellite. Credits: ESA* ***Right****: the second Sun-Earth Lagrange point (L2) is situated about 1.5 million kilometers from the Earth on the line defined by the Sun and Earth. At L2, the outward directed force from the rotation around the Sun counterbalances the gravitational attraction by the Earth, Moon and Sun. Euclid will rotate in an orbit around L2; this orbit, which has a diameter of about 1 million kilometers, is roughly situated in a plane perpendicular to the Sun-Earth line. Credits: ESA*

- what are the nature and properties of dark matter?
- what are the initial conditions which seed the formation of cosmic structure?

The mission is centered on weak lensing and baryon acoustic oscillations (see section 1.6), two powerful and robust probes of the dark Universe. Using these cosmological probes Euclid will measure the distance-redshift relation and the growth of structures. For the convenience of the reader, we briefly remind here that:

1. the weak gravitational lensing method relies on the fact that the distribution of mass along the line of sight distorts the apparent shapes and orientation of galaxies. The matter distribution, and hence cosmological structures, is obtained from the inferred gravitational field causing the weak lensing. This provides a measurement of the effect of dark energy on both the geometry and the growth of structure
2. with baryon acoustic oscillation it is possible to infer the distribution of matter using a redshift survey. The characteristic scale length of structure which can be accurately determined from the cosmic microwave background is used as a standard ruler. By measuring this characteristic scale in the galaxy power spectrum one directly probes the expansion history and thus the equation of state of dark energy ϖ_{DE}. At the same time, the statistical distortion of the clustering pattern is a direct consequence of the growth of structure.

Observing from space avoids sources of systematic errors caused by the Earth's atmosphere and thermal variations, which seriously limit similar observations from ground. This will give an unprecedented improvement in the dark energy characterization in comparison to what can be achieved from ground only.
A single space mission appears capable of providing multiple probes of DE, including sets that can measure expansion and growth histories independently. The primary virtue

of a space mission is that it offers opportunities to reduce significantly the systematic uncertainties associated with all methods.

The statistical study of structures in a large volume of the Universe requires a survey of a large fraction of the extragalactic sky. The Euclid **wide survey** will produce a visible image of a large fraction of the extra-galactic sky (15,000 deg^2) at a diffraction limited spatial resolution not possible from ground due to the high background emission from the atmosphere. This wide survey will enable the measurement of shapes and redshifts of galaxies up to to redshift $z = 2$ as required for weak lensing and BAO.

The photometric redshifts will be derived from three additional Euclid near-infrared (NIR) bands (Y, J, H in the range $0.92 - 2.0\mu m$) reaching AB magnitude $AB_{mag} = 24$ in each band, plus information coming from ground based photometry in visible bands derived through collaborations with ground based projects.

To measure the shear from the galaxy ellipticities a tight control is imposed on possible instrumental effects and will lead to the variance of the shear systematic errors to be less than 10^{-7}.

The BAO are determined from a spectroscopic survey with a redshift accuracy of $\delta z \leq 0.001(1+z)$. This accuracy is comparable to that of DESI (see section 2.3), that should be operative starting from 2018.

Euclid will perform spectroscopy using a slitless spectrometer with constant $\lambda/\delta\lambda = 500$, which will detect mainly H_α emission line galaxies. The limiting line flux level will enable the gathering of 70 million galaxy redshifts with a success rate (i.e. the fraction of the total amount of detectable galaxies from which the redshifts can be determined) of 35%.

Euclid's additional **deep survey** will cover 40 deg^2. This survey will be 2 magnitudes deeper than the wide survey, by frequently visiting the same regions in the wide survey observing mode.

2.4.2 The Service Module and Payload Module

The spacecraft is composed of the two following sub-systems:

- the Service Module (SVM)
- the Payload Module

The **Service Module** sub-systems (see figure 2.4) include the sunshield, the star trackers and gyros, the thrusters, the micro-motions and slews control systems, with hydrazine and cold gas tanks, the Attitude and Orbital Control System (AOCS), the solar panel and electric power system, the thermal regulation system and the downlink communication system.

The structural/thermal architecture is designed with the aim to provide a high degree of thermal isolation to the payload module (PLM) as well as high thermal stability. The sunshield provides the main thermal barrier with respect to the solar heat load. The

thermal isolation between the back of the sunshield and the top of the service module (SVM) with the PLM is performed with high performance multi-layer insulation (MLI).

The **Payload Module** (see figure 2.5) comprises the telescope, the PLM thermal control system, the Fine Guidance Sensor (FGS), the VIS and NISP instruments and the detectors.

The telescope is a 1.2 m on axis 3-mirror Korsch cold telescope providing a field of view of $1.25 \times 0.727\ deg^2$. Mirror 1 (M1, see figure 2.5) is maintained at temperature below 130 K with thermal stability better than 50 mK. The mirrors and structures are all made in Silicon Carbide, a material with excellent thermo-elasticity and stiffness and immune to radiations. The telescope design comprises a 3 degree-of-freedom mechanism for Mirror 2 (M2) focus and tilt correction that allows to meet all requirements on the image quality for weak lensing science (ellipticity, FWHM, R2 and encircled energy) .

The weak lensing experiment requires a high pointing stability to ensure optimum width and ellipticity stability of the point spread function (PSF). To meet the relative pointing error requirements the AOCS include a fine guidance sensor (FGS) for accurate attitude measurement. The FGS uses the same CCD type as the VIS instrument and share the same optical field of view.

The **Visible Instrument** (VIS) is used to measure the shapes of galaxies. Its focal plane is composed of a matrix of 6×6 4096×4132 12 micron pixel CCDs, specially optimized for the Euclid mission. The VIS fiocal plane covers a field of view of about 0.5 deg^2 (twice the angular size of the full Moon and about 450 times the field of view of the Hubble Space Telescope ACS camera) with 0.1 arc-second pixels.

The instrument is be equipped with one single very broad band filter covering the wavelength range from 550 nm to 900 nm with a mean image quality of about 0.23 arc-second.

2.4.3 The NISP Instrument

The **Near Infrared Spectrometer and Photometer** (NISP) instrument aims at providing near infrared (between 900 and 2000 nm) photometry of all galaxies observed also with VIS and near infrared low resolution spectra and redshifts of millions galaxies. The near infrared photometry will be combined with ground based photometry to derive photometric redshifts and rough estimates of distances of galaxies seen by VIS.

The near infrared spectra will be used to derive accurate redshifts and distances of galaxies and their 3-dimensional position in the Universe. The NISP spectroscopic data will primarily be used to describe the distribution and clustering of galaxies and how they changed over the last 10 billion years under the effects of the dark matter and dark energy content of the Universe and of gravity.

The instrument focal plane is composed of a matrix of 4×4, 2040×2040, 18 micron pixel detectors covering a field of view of about 0.5 deg^2 shared with VIS, with 0.3 arc-second pixels. The photometric channel will be equipped with 3 broad band filters (Y, J and H) covering the wavelength ranges 900-1192 nm, 1192-1544 nm and 1544-2000 nm,

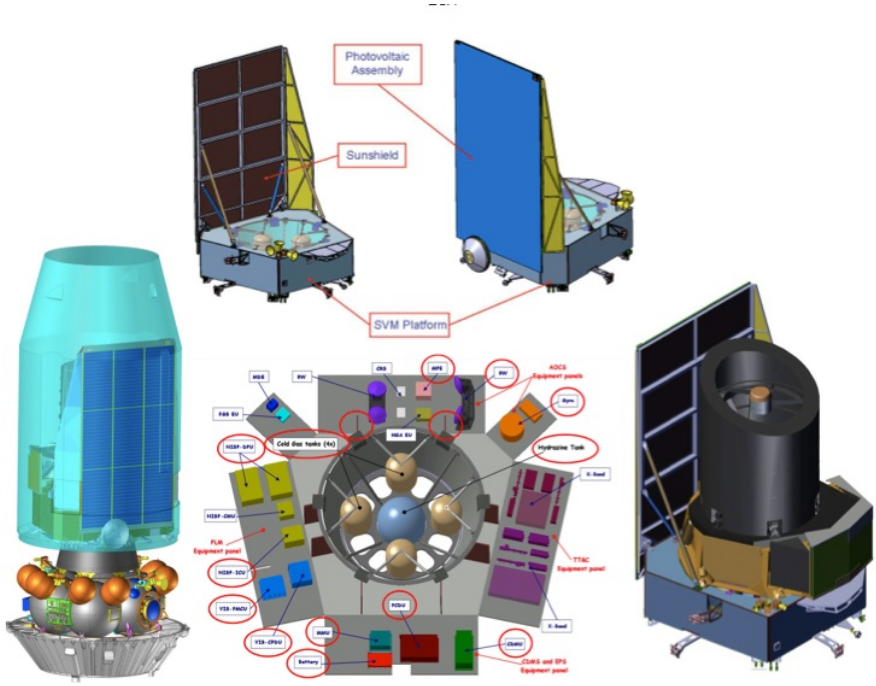

Figure 2.4: Detailed views of the Euclid spacecraft elements. The left panel shows the satellite inside the top end of the Soyuz Fregate rocket. Credits: `https://www.euclid-ec.org/?page_id=2686`

respectively, with a mean image quality delivering.

The spectroscopic channel will be equipped with 4 different low resolution near infrared grisms (R=380 for a 0.5 arc-second diameter source), 3 "red" (1250 nm – 1850 nm) and 1 "blue" (920 nm – 1250 nm), but no slit ("slitless spectroscopy"). The three red grims will cover the same wavelength range but will provide spectra with three different orientations (0°, 90°and 180°) in order to decontaminate each slitless spectrum from possible overlapping spectra of other sources in the field.

The instrument is composed of different units, organized in three main assemblies:

1. the Opto-Mechanical Unit (NI-OMA, see figure 2.6) composed of the mechanical structure and its thermal control and the optical elements. It comprises the Grism Wheel Assembly (NI-GWA), holding the four dispersing elements for the spectroscopic mode, the Filter Wheel Assembly (NI-FWA), holding the three filters for the photometric mode, and the Calibration Unit (NI-CU), injecting calibration signal in the optical beam for calibration purposes

2. the Detector System Assembly (NI-DS), composed of The Focal Plane Array (NI-FPA) and the Sensor Chip System (NI-SCS)

3. and the Warm Electronic Assembly (NI-WE), composed of the Instrument Data Processing Unit (NI-DPU), the Detector Control Unit (NI-DCU) and the Instrumental Control Unit (NI-ICU).

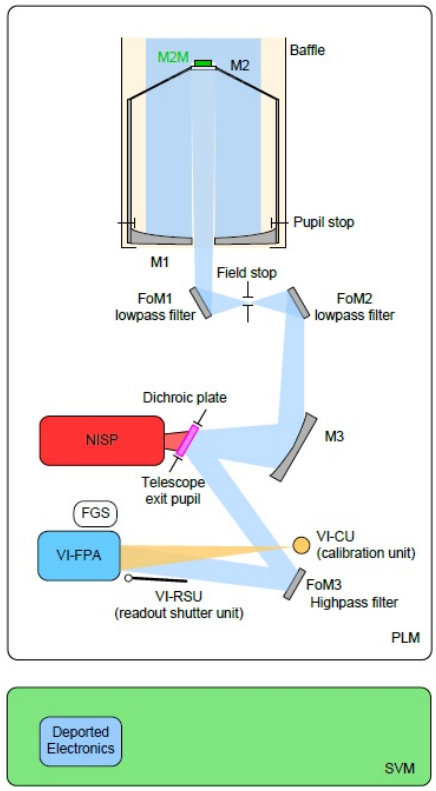

Figure 2.5: The Euclid Payload Module. Credits: `https://www.euclid-ec.org/?page_id=2639`

2.4.4 Scanning Strategy

Euclid will survey the sky in "step-and-stare" mode: the telescope will point to a position on the sky and imaging and spectroscopic measurements will be performed on an area of about 0.5 deg^2 around this position. The sky coverage strategy is driven by the wide-survey requirement to cover 15,000 deg^2 of extragalactic sky during the mission lifetime of 6 years (see section 2.4).

The main considerations behind the survey strategy are:

- the L2 orbit and spacecraft viewing constraints (see figure 2.7)
- maintaining the thermal stability
- the fundamental exposure times of the instruments and the size of a field of view, which is 0.5 deg^2.

For the imaging channels, dithering is required to over-sample the point-spread-function to fill the gaps between the detectors, and to ensure that the field is completely covered. During each frame VIS and NISP carry out exposures of the sky simultaneously. At the end of the last frame, a slew towards the next field is performed. Figure 2.8 shows an

Figure 2.6: The NISP Opto-Mechanical Unit and Detector System mock-up. Credits: `http://www.mpe.mpg.de/391950/gallery`

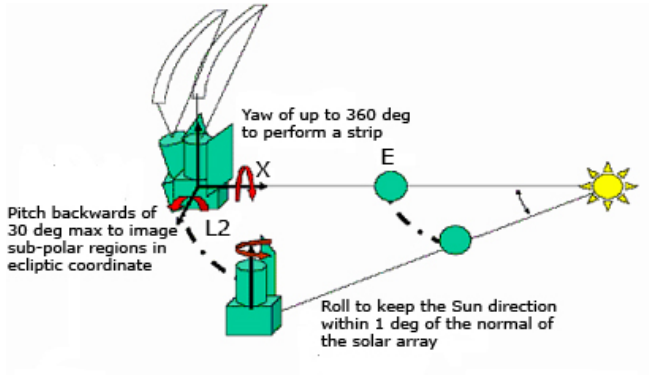

Figure 2.7: The Euclid survey strategy depends on the imposed viewing constraints at L2. Credits: `http://sci.esa.int/euclid/46682-euclid-survey-strategy/`

example of the operational time sequence of one frame.

For each frame the nominal integration time in the VIS and NISP is 590 seconds, followed by NISP photometric measurements with integration time: Y band = 88 seconds, J band = 90 seconds, H band = 54 seconds. Then, because of image disturbing vibration from filter wheel rotation, VIS has its shutter closed during the remaining exposures taken for NIR imaging.

The dithering strategy covers the gaps between detectors. It also mitigates the impact of cosmetics defects and cosmic rays on science data, and improves the sampling of the images. In the case of NISP spectroscopy, the four dithers are used to obtain slitless spectra.

Based on initial AOCS performance estimates, the following times have been used to construct a realistic reference survey: 64 seconds for a dither, and 280 seconds for a field-

to-field slew.

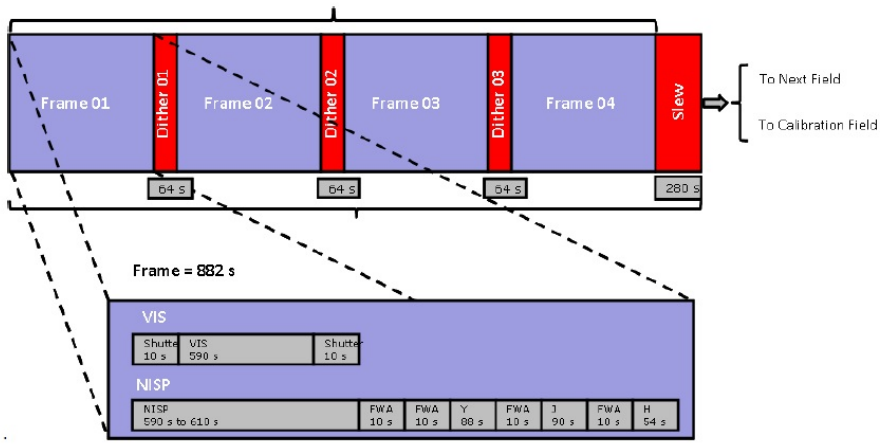

Figure 2.8: Schematic timeline of an observation sequence of one field. Each frame (blue) starts with a simultaneous VIS and NIS exposure, followed by three NISP photometric exposures. The three dither-to-dither slews and the field-to-field slew are marked in red. The time allocations for the VIS shutter and the filter wheel movements of the filter wheel assembly (FWA) are indicated. Credits: `https://arxiv.org/ftp/arxiv/papers/1110/1110.3193.pdf`

2.4.5 The Euclid Ground Segment

The Euclid data processing system is organized in different processing levels connected with logical data **Processing Functions** (PF), which are part of the Science Ground Segment. In particular, the SIR PF is in charge of producing fully calibrated spectral images and extracts the spectra in the slitless spectroscopic frames taken by the NISP instrument.

It is customary for those elements of a space mission which are in a close functional relationship to be combined into one segment. This makes it possible to divide the entire space mission into just a few major segments. With their help, the complex interrelationship of a space mission can be more easily and generally described. Often a space mission is divided into three segments:

1. the **launch segment**, comprising the launch system, the launch service and the necessary infrastructure
2. the **space segment**, comprising the development of all spacecraft equipment, the payload, the system engineering activities and tests
3. and the **ground segment**, including the ground infrastructure, the equipment, the hardware and software for linking the space segment and the mission control center, and the data processing and archiving facilities.

The Euclid ground segment consists of two blocks: the **Operational Ground Segment** (OGS), and the **Science Ground Segment** (SGS). The SGS is composed of the Science Operations Center (SOC); and it is responsible for the end-to-end handling of the Euclid data, and production and archiving of the Euclid mission products.

The Euclid ground segment is composed mainly by:

1. the **Mission Operations Center** (MOC), in charge of all mission operations planning, execution, monitoring and control of the spacecraft and operations ground segment
2. the **Ground Station** network, managed entirely by ESA. The Ground Station supports a daily telemetry communications period of nominally 4 hours during nominal operations and longer during the commissioning and performance verification phases. The ground based data have to undergo Euclid specific processing in order to be consistently handled with the Euclid data.
3. the **Science Operation Center** (SOC), see figure 2.9, managed by ESA. It is in charge of scientific operations planning, performance monitoring of the payload using spacecraft and instrument files delivered by MOC. It receives the telemetry from MOC, does a first level processing and quality check to the science data and delivers these data to the **Science Data Centers** (SDCs) for further processing. SOC is also responsible for the public releases of the data via its legacy archive. The SDCs will host the instrument operation teams, which are responsible for monitoring the health of the instruments and the understanding of instrumental effects in the science data.

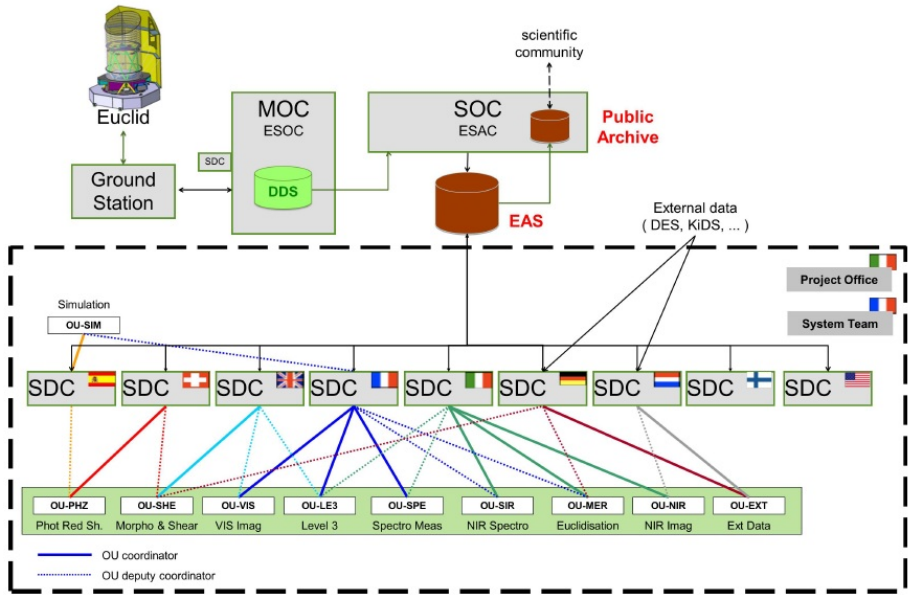

Figure 2.9: Sketch of the 2016 Euclid Ground Segment (SGS) organization (see Dubath 2015)

The **Euclid Consortium** (EC) provides the fraction of the Ground Segment performing the data processing from telemetry down to the mission data products. It is also responsible, for example, for developing the algorithms and writing the software for the entire processing system. The SGS is physically composed of a number of Science Data Centers (SDCs), in charge of instrument-related processing, production of science data products, simulations, ingestion of external data and in general all science-driven data processing.

Two **Instrument Operation Teams** (IOTs), one for each instrument, guarantee instrument maintenance and operations. The computational needs of the IOTs are supported by the SDCs.

Integrating help provided by the Euclid consortium, one of the SOC tasks is to decode the telemetry packets and store the raw data in the form of computer readable numbers. These "level 1" raw data are the starting point of the functional decomposition. The low-level cleaning and corrections, such as bias subtraction, flat fielding, cosmic ray removal and charge transfer inefficiency corrections of the CCD frames as well as their astrometric and photometric calibration are divided into different tasks according to the data type. They are grouped into the VIS, NIR, SIR and EXT processing functions for the visible image, the near infrared image, the near infrared spectra and the ground CCD frames, respectively.

The processing of science data can be decomposed in ten self-contained processing units called **Processing Functions** (PF) (see figure 2.10 and table 2.1).

Processing Function	**Task**
LE1	Telemetry unscrambling
VIS	Processes the Visible imaging data from edited telemetry to fully calibrated images; source lists for quality check purposes
NIR	Processes the Near-Infrared imaging data from edited telemetry to fully calibrated images; source lists for quality check purposes and to allow spectra extraction)
SIR	Processes the Near-Infrared dispersed imaging data from edited telemetry to fully calibrated spectral images and extracted spectra
EXT	Enters in the Euclid Archive all of the external data that are needed to proceed with the Euclid science
SIM	Provides the simulations needed to test, validate and qualify the whole pipeline
MER	Performes the merging of all information, providing stacked images and source catalogues where all the multi-wavelength data (photometric and spectroscopic) are aggregated
SPE	Extracts spectroscopic redshifts from the SPE spectra
PHZ	Computes photometric redshifts from the multi-wavelength imaging data
SHE	Computes shape measurements on the visible imaging data

Processing Function	**Task**
LE3	computes shape measurements on the visible imaging data

Table 2.1: Processing Functions constituting the Euclid data analysis functional decomposition

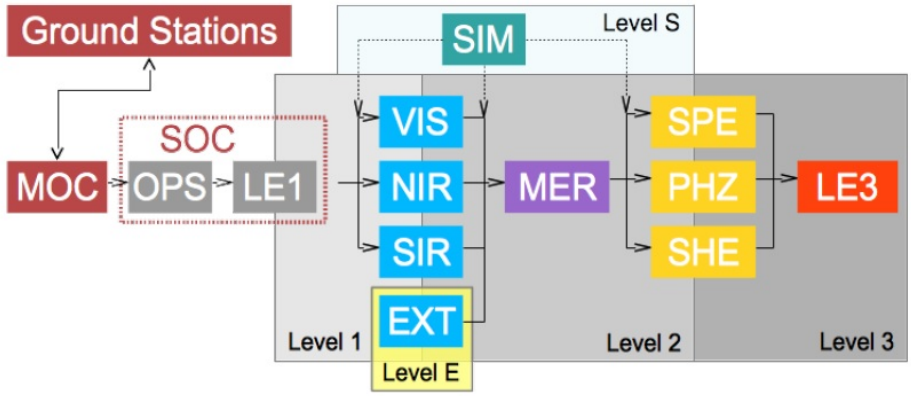

Figure 2.10: Simplified picture of the Euclid data analysis functional decomposition (see Dubath 2015)

CHAPTER 3

An End-to-End Mission Performance Simulator for the Euclid Space Mission

3.1 Introduction

The design of a space mission is a long and complex process. The support of dedicated software tools is necessary, especially for the performance analysis of the mission itself. The request is then for specific tools that can simulate the complete behavior of the probe, its payload (i.e. those elements of the spacecraft specifically dedicated to producing mission data), and scientific data acquisition starting from synthetic scenes. These software tools, called "**End-to-End Mission Performance Simulators**" (E2ES), are promoted by the European Space Agency (ESA) with the goal of consolidating the instrument and mission requirements as well as optimizing the implemented data processing algorithms.

A mission performance simulator assumes a level of performance for the payload and assesses its ability to meet mission objectives. At early development phases, the E2ES is usefull then:

- to asses the mission performance
- to support the consolidation of the conceptual design, and of the technical and scientific requirements
- to allow end-users to assess the fulfillment of requirements by the mission

Once the design and requirements have been consolidated, the E2ES can be usefully exploited for the validation of the ground data processing pipeline.

The goal of mission simulation is to estimate measures of effectiveness as a function of key system parameters. The simulator must be simple enough to allow making multiple runs, so we can collect statistical data and explore various scenarios and design options.

The mission simulation should include parameters that directly affect key system issues like the orbit geometry, motion or changes in the targets or background, system scheduling, and so on. The problem of excessive detail is best solved by providing numerical models obtained from more detailed simulations of the payload or other system

components. We start with simple models for the individual components and develop more realistic simulation conditions as we create and run more detailed payload or component simulations.

In order to compare options and designs usually a baseline scenario is selected. If you are running a comparative analysis, indeed, you must select a reference simulation to act as the baseline and then compare all other scenarios with respect to this baseline. Repeating multiple times a single scenario allows us to understand the scenario and the system's response to it. We can also establish quantitative differences by showing how different designs respond to the same simulation settings. But this approach tends to mask characteristics that might arise solely from a particular scenario. Thus, we must understand what happens as the baseline changes and watch for chance results developing from our choice of a particular baseline scenario. Finally, mission simulations must generate usable and understandable information that provides physical insight to decision makers.

3.2 Feasibility Study for a Euclid E2ES Simulator

ESA has been widely using mission performance simulators in Earth Observations (EO) programs. The European Space Agency has then promoted several activities in order to reduce the re-engineering effort to generate E2E simulators (promoting reuse in the development of E2ES), and to test the feasibility of a generic environment for space missions. The activity described in the present section and in Chapter 4 has been supported by the ESA contract no. IPL-PTE/GLC/al/241.2014. The contract had a duration of one year: it started in June 2014 and ended in October 2015.

The goal of the contract is the realization of a feasibility study for the design and the implementation of a E2E simulation environment similar to that already present for EO missions (see section 3.3) for a generic space mission. Due to its complexity (see section 2) the Euclid mission represents a satisfactory test case and a E2ES is highly desirable to verify the performance of the onboard instrumentation, and the mission scientific capabilities. Furthermore, a End-to-End simulator can also be a tool to mimic test scenarios in order to assess the mission performance as a function of changes in the instrument configuration and to analyze possible error sources.

A "**proto E2E simulator**" and a "**full E2E simulator**" have been defined: the proto-E2ES has reduced features, is limited to spectroscopic simulations (NISP-S) and the modules are implemented in a simplified version. In its full version, the proposed Euclid E2ES is designed to include both the NISP and VIS instruments. Given the complexity of the Euclid mission, the analysis has been limited to a very specific science case: the determination of spectroscopic redshifts for galaxy clustering. Simulations have then been restricted to the Euclid/NISP-S detection system and corresponding optical system.

Three people from "Università degli Studi di Trieste" have been involved in the study: Dr. A. Gregorio, Dr. E. Romelli and myself. I focused mainly on the verification and validation of the proto-E2ES, conceiving test cases, preparing and executing test sequences and producing test reports. Dr. E. Romelli has been the main developer of the script and test executor of those sequences dedicated to software verification.

The work has been performed under the supervision of Dr. A. Gregorio and followed these development phases:

1. identification of the requirement baseline for the EUCLID E2ES
2. definition of the architectural design of the E2ES for the Euclid mission
3. implementation of the "proto-E2ES"
4. verification and validation of the "proto-E2ES"

3.3 Review and Analysis of E2ES Mission Performance Simulators

Given the past experience of the European Space Agency in simulators dedicated to Earth observation, a review of EO E2ES has been a necessary first step in the designing process of a general E2ES applicable also to space science (see Battaglia & Romelli 2014).

As a guideline for this analysis we used the final report of the ARCHEO-E2E project (see Archeo E2E Team 2013): an activity promoted by ESA whose main objective is that of defining a reference architecture for E2ES. In order to have the widest selection of mission simulators available, several EO missions have been reviewed. Among these are EUMETSAT, ENVISAT, GOSAT, NPOESS, SCISAT, NESDIS, METEOSAT, SWARM and SENTINEL-2.

Our review shows that an E2ES, typically, is composed of several modules reproducing the experiment processing flow. Usually, the first release of the simulator is developed as a prototype tool to support the initial performance assessment of the mission. It is expected that the simulator will evolve to support the detailed mission design during the development phases.

The modular architecture, indeed, gives to E2ES the flexibility and ability to support "extensive" and "evolutionary growth", i.e.:

- the ability to include more effects (extensive growth)
- the ability to achieve more accuracy in the simulator (evolutionary growth)

The basic idea is to define at first an essential architecture that contains the basic modules for the E2ES and to provide the required flexibility to the architecture to grow in both the extensive and evolutionary sense in order to include more modules as well as different modules that implements different models.

Our analysis showed that the following aspects may affect the definition of a reference architecture for E2E simulators (see figure 3.1):

1. **the number of satellites composing the mission**: single platform (e.g. ENVISAT, ERS, SMOS, METEOSAT) or multiple platform (e.g. SWARM, Sentinel-2). In case of multiple platform, other sub-criteria can be established, like formation flying, combined/separate measurement, identical/different instruments on-board
2. **the number of instruments on-board the spacecraft**. A detailed survey of the instruments flown on-board EO missions is important in order to identify common-

alities and to define the optimum architecture for each case. The most significant criteria for the definition of a reference architecture are: the region of the spectrum at which the measure are taken, if the instrument is passive (e.g. waveguides) or active (e.g. amplifier), the target of the measurement (i.e. atmosphere, land, ocean, snow and ice, other) and the type of retrieval products

3. **the scientific objective of the mission**, which could not be unique.The mission could investigate one or more objectives and there is not a direct relation between the number of scientific objectives and the number of satellites or instruments onboard of a single spacecraft.

4. **links with other missions**. There are missions with requirements asking for loose formation flying configuration with respect to an existing mission. The final objective of these missions is to obtain measurements that are temporally and spatially co-registered with those from the existing mission, in order to combine the data at some point in the retrieval. This criterion is practically identical to the case of having two spacecraft of the same mission combining measurements.

5. **orbit characteristics**. Orbit selection is constrained by the scientific objective of the mission and the instrumental setup. The great majority of EO missions are placed at Sun synchronous orbits, while Euclid will observe the sky from a halo orbit around the Sun-Earth L2 position (see paragraph 2). Since this position follows our planet in its revolution around the Sun we must take into consideration background contaminants that vary on a seasonal scale, e.g. The Zodiacal light

6. **scanning strategy**. Depending on the instruments onboard, but also on the scientific objective of the mission, it will be defined for the mission a observation strategy or scanning method. The Euclid mission requires dithering in order to fill gaps between detectors. A good knowledge of the dither pattern is then required in order to simulate the on-board instrumentation.

The identification of reference architecture and generic building blocks for E2ES simulators lies also in the search of commonalities at different levels, including also a detailed survey of the instrument flown onboard past, current, and planned EO missions. This will help also in defining the optimum architecture for each case. Only those criteria that have an impact on the definition of the reference architecture have been analyzed: e.g. the region of the spectrum at which the measure are taken (optical or infrared in the Euclid case); if the instrument is active or passive; the type of retrieval products; the calibration method (on board calibration vs ground calibration).

3.4 The Architecture of the Euclid E2ES Simulator

A high-level architecture has been proposed (see figure 3.2) in response to the global system description and requirements provided in the ESA internal reports "*EUCLID E2ES Requirement Baseline*" (see Battaglia & Romelli 2015b) and "*EUCLID E2ES Design Definition*" (see Battaglia & Romelli 2015a).

The starting point for the design activities has been requirements definition. All requirements must begin with short and well defined user and customer mission needs, focusing on the critical functional and operational requirements, without unnecessarily

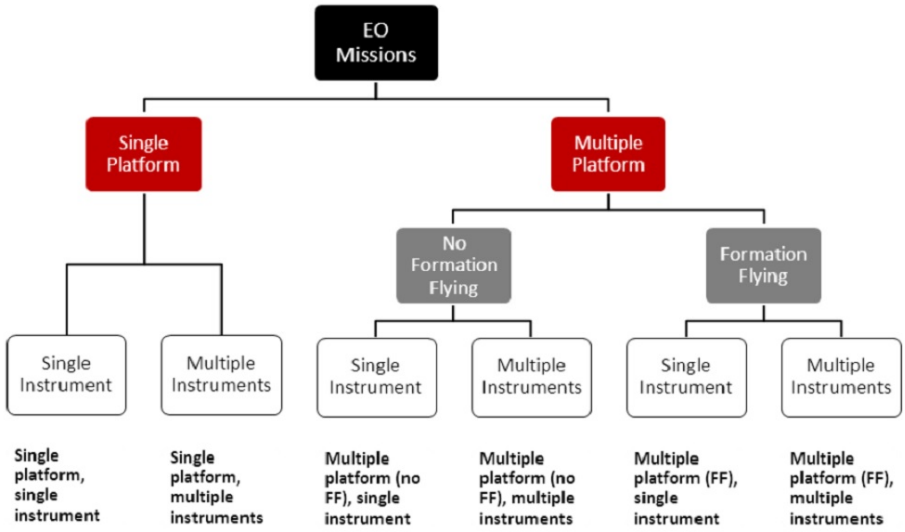

Figure 3.1: Categorization of EO Missions by number of satellites and number of instruments in the mission. The "Multiple-Platform" case rarely apply to space missions (e.g. the Laser Interferometer Space Antenna). Credits: Archeo-E2E Final Report, (see Archeo E2E Team 2013)

constraining or dictating the design. Mission requirements concerning launch, operation, or maintenance may establish the design domain but not dictate the design. On the other hand, the user must also be a party to the system design as it converges, to identify design characteristics likely to produce operational problems.

Balancing requirements, constraints and goals, a modular structure has then been proposed for the simulator, so that the different components of the E2ES remain unaffected by possible required improvements or changes in part of the modules. Thanks to its modular structure, the simulator allows the user to run not only the whole chain, but also a single module or a subset of them, according to his/her purposes. The following eight modules have been defined:

1. **Euclid Survey Strategy** (ECSS): it defines an observing strategy according to the scientific scenario to investigate
2. **Simulated Sky** (SS): it simulates a given region of sky according to the defined survey strategy
3. **Spacecraft and Environment** (SCE): it handles the attitude of the spacecraft and its orbital status during the operations foreseen by the simulated strategy
4. **Optical Model** (OM): it provides an optical model to be convolved with the simulated sky, taking into account possible attitude modifications
5. **Detection System** (DS): it simulates the behavior of the on board instrumentation and the effects of the detection chain
6. **On-Board Data Generation** (OBDG): it handles the telemetry (both instrumental and spacecraft housekeeping) data and the on-board data compression

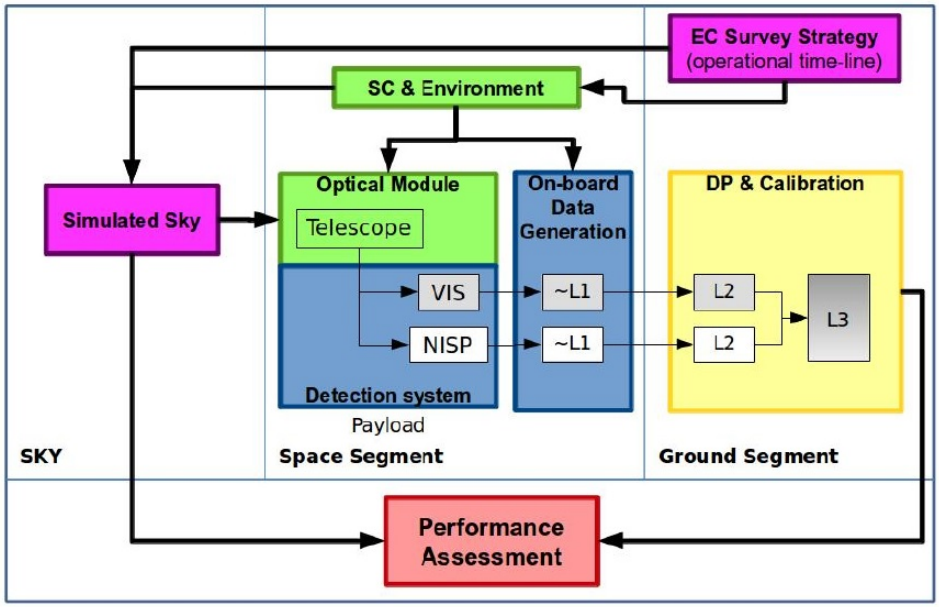

Figure 3.2: The proposed high-level architecture for the Euclid E2ES. Magenta modules represent the sky simulation (ECSS and SS). Green represents the spacecraft and telescope environment (SCE and OM). Light blue modules refer to the instrumental environment (DS and OBDG). Yellow represents the ground based environment (DPC), while red refers to the performance assessment (PA). Image credit: EUCLID E2ES Design definition, (see Battaglia & Romelli 2015a)

7. **Data Processing and Calibration** (DPC): it runs a simplified version of the ground-based data processing pipeline

8. **Performance Assessment** (PA): it checks the good functioning of the whole E2ES, comparing the input of the simulation chain, i.e. the simulated sky, with the output of the simulator

The color code used to identify the modules in figure 3.2 is linked to the logical macro-area each module belongs to. The magenta modules represent the sky simulation (ECSS and SS); green ones represents the spacecraft and telescope environment (SCE and OM); light blue modules refer to the instrumental environment (DS and OBDG); yellow ones are the ground based environment (DP), while red blocks refers to the performance assessment (PA).

The high-level architecture has been designed considering two different versions of the simulator: a prototype version, called **proto-E2ES**, and a complete version, the **full-E2ES**.

The full-E2ES, which is conceived to include both the Euclid NISP and VIS instruments, will be able to assess the synergy between the two instruments embarked on the mission, the observation strategy and the operations.

The proto-E2ES has reduced features, is limited to spectroscopic simulations (NISP-S)

and the modules are implemented in a reduced version, avoiding all the housekeeping data generation and, as a consequence, implementing the calibration chain in a simplified way. It will deal with wide survey strategy only.

3.4.1 Euclid E2ES Modules Description

This section runs through the simulation chain, and gives a detailed description of the modules and their functionality. Below we give a description of all the modules conceived in the reference architecture. In the proto-E2ES, due to its reduced simulation capabilities, some of these modules have not been implemented (see section 3.5).

The first module we encounter in the simulation chain is the **ECSS** (see figure 3.3). Once the observation target has been defined, the ECSS module provides the observing strategy by the means of an operational time-line. The time-line:

1. contains the instrument exposure times, and the spectral band (for NISP spectroscopic channel only) in which the user wants to perform the simulation
2. is meant to store attitude parameters, such as the Solar Aspect Angle (SAA) of the satellite (i.e. the angle between the pointing direction and the vector to the Sun) and the parameters needed to simulate one of the major background contaminants for the Euclid mission, the Zodiacal Light Emission (ZLE)
3. is designed to take into account the fact that Euclid observes the sky trough a Wide Survey and a Deep Survey.

The **Simulated Sky** module is meant to create a simulated region of sky through catalogs of sources. The catalog must contain the spatial coordinates and additional parameters linked to the nature of the source (i.e. point-like or extended), such as, for instance, the half-light radius of the source. The sizes of galaxies are, indeed, difficult to measure since they don't possess clearly defined boundaries. Most galaxies simply get fainter in their outer regions, and the apparent size of the galaxy depends almost entirely on the sensitivity of the telescope used and the length of time for which the object is observed. To overcome this ambiguity, astronomers define the "half-light" radius as the radius within which half of the galaxy's luminosity is contained.

This module is meant to handle the simulation of possible background or foreground sources, focusing on ZLE as a major contaminant. The simulator observes sky regions (for details of the sources input catalog see section 4.3) within a VIS or NISP field of view, taking as input pointing coordinates and exposure times from the ECSS operational time-line.

The **Spacecraft and Environment** module simulates the attitude and control system and deals with disturbances that can affect the pointing and can bring to thermal or mechanical perturbations on the payload.

The **Optical Module** handles telescope and instrument optics, and it provides an optical model to be convolved with the simulated sky. The optical model is parametric, with values of the optical parameters stored in a configuration file, which is the input of the Detection System module. Deviations from ideal optics are treated modifying the

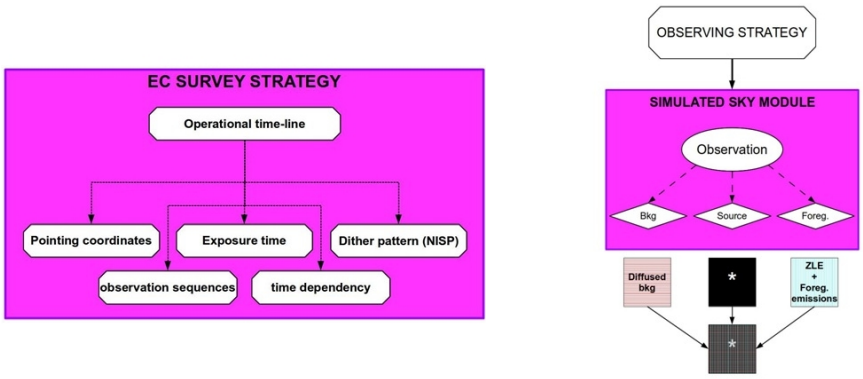

*Figure 3.3: **Left**: ECSS Module **Right**: SS Module. (Image credit: EUCLID E2ES Design definition, (see Battaglia & Romelli 2015a)*

values of the parameters via transfer functions. This module is strictly linked to the Euclid mission database and it is meant to evolve together with the mission database itself.

The **Detection System** module simulates the effect of the detection chain, i.e. the behavior of the detectors. This module is split in two different chains: one for the VIS instrument and one for NISP. The NISP chain is divided in two sub-chains: NISP-P for the photometric simulations and NISP-S dealing with spectroscopy. This module treats instrumental noise and systematic effects, the readout and the instrumental timescales such as the opening/closing of the dithers and the exposure times. Inputs to this module are the catalogs from the SS module, together with the information contained in the ECS operational time-line and the OM configuration file.

A complete simulation of the on-board data generation is beyond the scope of an E2ES for performance assessment. For that reason the **On Board Data Generation** module is meant to simulate only simplified data structures, if required for the E2ES purpose. The module is split in two different chains:

- the housekeeping data chain. It takes input data directly from the SCE as the housekeeping data are not affected by the optical environment and the detection system
- the science data chain. It handles the proper scientific data and the housekeeping of the instruments. Not all the telemetry will be simulated.

The OBDG should also handle the compression of data. Data compression for Euclid is mostly loss-less and no major problems due to decompression of data are foreseen. Compression will not then be implemented neither in the proto-E2ES nor in the full-E2ES.

The **Data Processing and Calibration** module simulates the ground-based data processing and calibration. It takes simulated high level data from the DS and provides, as an output, processed data. Satisfying the calibration requirements corresponds to simulate a set of calibration observations and this is beyond the scope of an E2ES. For that reason, calibration in this module is treated in a simplified version. Processed data are then used

by the PA module.

The **Performance Assessment** module is meant to verify the good functioning of the whole E2ES, comparing the input of the simulation chain (i.e. the simulated sky from the SS) with the output of the simulator. It takes the final product of the simulation chain and checks that these products fulfill the desired requirements, given defined metrics or a defined figure of merit (see figure 3.4). The figure of merit defined for the proto-E2ES are:

1. redshift measurement. This is the main parameter to be used for the performance assessment. It is compared with the input value given by the catalog
2. three scientific parameters: **Completeness** (i.e. the fraction of spectra measured above a given line flux limit), **Purity** (the fraction of spectra correctly measured above a given line flux limit, and **Redshift errors** and **detection limit**. All parameters are compared with input values given by the catalog.

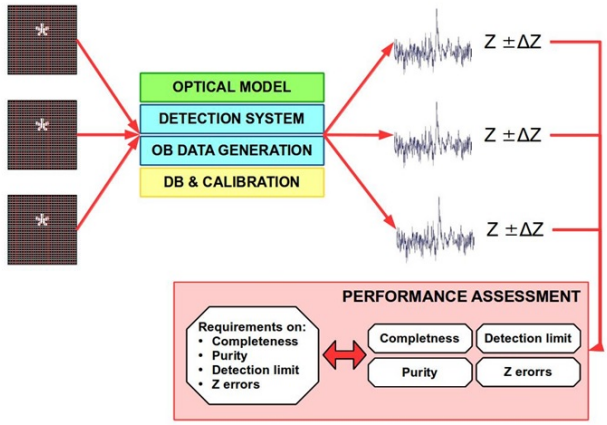

Figure 3.4: The image shows an example of the functioning of the simulator. A set of simulated sources, from the Simulated Sky Module, are treated by the modules of the simulator. The simulator gives as output spectra, redshift measurements and L-2 and L-3 data. The module compares them with the requirements to be fulfilled. If the requirements are correctly achieved the simulator can be considered as performing. Image credit: EUCLID E2ES Design definition, (see Battaglia & Romelli 2015a)

3.5 The Euclid E2ES Prototype

Two versions of the proto-E2ES simulator have been implemented:

1. the proto-E2ES v1.0 - preliminary simulator delivered to ESA as one of the final products of the work supported by contract IPL-PTE/GLC/al/241.2014
2. the proto-E2ES v2.0 - a version meant to be compliant with the Euclid software framework.

The proto-E2ES has been successfully verified and validated by means of a "verification and validation plan" (see Battaglia & Romelli 2015c). Section 4 contains a detailed

description of the test campaign conducted on the simulator and its results.

3.5.1 Proto-E2ES Version 1.0

The simulator is a Python script. The code is open source (under the terms of the GNU Lesser General Public License),and wraps dedicated Python libraries and three external software tools: TIPS, aXeSIM, and IRAF.

TIPS (This Is a Pixel Simulator) is a simulation tool which produce the expected images of an observation for a given instrument. The current version of TIPS is based on aXeSIM, an image simulator developed for Hubble Space Telescope (aXeSIM, Kuemmel et al. 2007 and 2009, http://axe.stsci.edu/axesim/), and it is able to simulate the 16 detectors of the NISP spectrometer. The current version include an automatic mode which was conceived to be easy to use, and it is able to manage several inputs formats.

aXeSIM is a dedicated simulation package that is able to extract spectra in slitless spectroscopy observations. It has been developed as part of the support for Wide Field Camera (WFC) 3 slitless spectroscopic modes. While the package was initiated for exploitation of WFC3 slitless grism modes, it is equally applicable to other slitless spectroscopy modes of the Hubble Space Telescope, such as the Advanced Camera for Surveys (ACS) and the Near Infrared Camera and Multi-Object Spectrometer (NICMOS).

Finally, **IRAF** is a general Image Reduction and Analysis Facility providing a wide range of image processing tools for the user. IRAF is a product of the National Optical Astronomy Observatories and was developed for the astronomical community. The IRAF core system provides the user with a wide selection of image processing tools using a command line interface.

The proto-E2ES has reduced capabilities with respect to the full version (see paragraph 3.4. The Spacecraft Environment (SCE), Optical Model (OM) and On-Board Data Generation (OBDG) modules have not been implemented in the prototype since SCE and OBDG modules simulate the attitude and control system and the on-board data generation process, and both are not created by the prototype pipeline. An OM has not been implemented since TIPS is able to deal with optical setup at a satisfactory level for the proto-E2ES.

The simulation workflow of the proto-E2ES is summarized in table 3.1). Please note that:

- the configuration file contains the catalog and configuration file names, the storing directory name and configuration flags to run the proper modules
- zodiacal light simulation is not integrated in version 1.0. Nevertheless, the operational time-line contains also parameters to simulate the Zodiacal Light Emission (ZLE)
- TIPS needs both photometric and spectral data of sources contained in the input catalog. The Simulated Sky module accept two different input methods: a catalog with photometric and spectral information for the sources, or a catalog with the coordinates of the sources and thumbnails of images and spectra

- the error on redshift (z) computed by IRAF using extracted and combined spectra is given by a propagation of error on the wavelength (λ): $\sigma_z = \sigma_\lambda / \lambda_{rest}$, where σ_λ is given by the FWHM of the best fit profile on the emission line.

Step	Module	Task	Input - Output	Notes
1	N/A	Read and load catalog and configuration flags	GlobalConfigurations.dat	Global configuration file name hardcoded with operational timeline and logfile names
2	N/A	Cleaning previous simulations	GlobalConfigurations.dat	Avoid spurious output. Action recorded in log file
3	ECSS	Read pointing data (pointing index and coordinates), and exposure time	N/A - OperationalTimeline_lite.csv	
4	SS	Create a TIPS-compliant version of the source catalog	Operational timeline, Input catalog - TIPS compliant catalogs	Implemented in simple version. SS module can run with both TIPS input methods
5	DS	Run TIPS simulation	TIPS compliant catalogs, optical parameters - Slitless images	Needs also a TIPS configuration file for optical and instrumental parameters. Each TIPS simulation produces 16 x 4 slitless images
6	DPC	Spectra extraction	Slitless images - Final products	Spectra extraction is performed by aXeSIM for each source in all dithers. They are combined and saved in IRAF compliant format
7	DPC	Spectral lines identification by IRAF	Combined extracted spectra	Each line treated as H_α emission line. Possible redshift (z) of the spectrum given
8	PA	Display simulation results, compute statistics for assessment	Final products, catalogs - Performance assessment	Compute completeness, purity and redshift error (see paragraph 3.4). One spectral line is enough to source detection.

Table 3.1: The table describes, step by step, the simulation workflow as managed by the Euclid E2ES (version 1.0)

3.5.2 Proto-E2ES Version 2.0

The scientific verification of the proto-E2ES version 1.0 revealed some issues (see section 4.4.2) which have been fixed by producing a second version of the simulator. Specifically the main topic is relative to the spectral line identification which, at proto-E2ES version 1.0 level, is performed by the IRAF software. The first version of the simulator is able to correctly detect only two out of the three spectral lines associated at each sources. The faintest one has never been observed and there have also been some spurious detections (see figure 4.18).

Spectral line identification has then been improved by substituting the IRAF software with a dedicated algorithm. The new spectral line identification algorithm implements a simple procedure to identify and fit spectral structures. The code takes as input spectra extracted from TIPS slit-less images by the aXe software. On the input spectrum the algorithm performs a smoothing in order to reduce the effect of the noise, applying to the spectrum a moving average filter. The maximum values of the smoothed spectrum are then searched by taking the derivative of the smoothed spectrum itself and looking for which points the sign of the derivative changes from positive to negative.

Maximum values are selected only above an adaptive threshold in order to ensure that the selected ones are good candidates to be flux peaks. The algorithm provides a list of selected peaks and performs a Gaussian fit within a window of twenty pixels centered on the peak position. For each spectral line the fit provides the line central wavelength λc, the line peak flux f and the line sigma σ_λ. Results on a test spectrum are shown in figure 3.5. For each line of the spectrum the red dot is the point $(\lambda_c; f)$ representing the peak position and flux. In red, the best Gaussian fit on each line is reported.

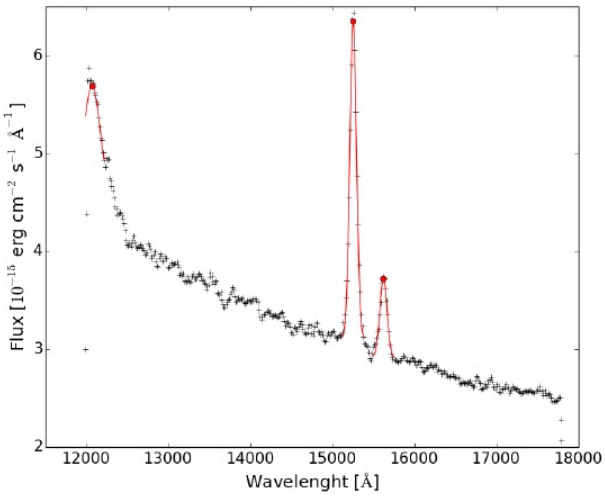

Figure 3.5: Results on a test spectrum of the new algorithm for spectral line identification. In red the Gaussian fit of the identified emission lines. Red dots represent peak positions and fluxes. For each line, the best-fit Gaussian is reported. Credits: (see Gregorio et al. 2016)

As minor topics, the file structure has been reorganized and the input-output interface has been reviewed from version 1.0 in order to make the simulator compliant with the software framework defined for Euclid and with the Euclid coding rules (see Bagot 2015)

The global configuration file has been redesigned in xml format, in order to store more information and to configure not only the input-output file names but their path also. This allows a better control on the E2ES. The output products saving system has been improved in order to store less files containing more information. The environment settings are unchanged, with scripts providing however the correct path to external dedicated libraries, since IRAF is no more integrated in this version of the simulator.

CHAPTER 4

The Verification and Validation of the Euclid E2ES Prototype

4.1 Introduction

The software verification and validation process is the one devoted to determine whether the requirements for a system or component are complete and correct, the products of each development phase fulfill the requirements or conditions imposed by the previous phase, and the final system or component complies with specified requirements.

According to ANSI/IEEE definition (see IEEE Standards Board 1990) the **verification** process is the act of "evaluating software to determine whether the products of a given development phase satisfy the conditions imposed at the start of that phase".
Verification is a static practice of verifying documents, design, code and program. It includes all the activities associated with producing high quality software: inspection, design analysis and specification analysis. Verification will help to determine whether the software is of high quality, but it will not ensure that the system is useful. Verification is concerned with whether the system is well-engineered and error-free.
The method of verification is the "**static testing**", i.e. reviewing and inspections.

Validation is "the process of evaluating software during or at the end of the development process to determine whether it satisfies specified requirements". Validation is the process of evaluating the final product to check whether the software meets the customer requirements. It is a dynamic mechanism of validating and testing the actual product.
The method of verification is the "**dynamic testing**". This testing technique is executed using a set of input values and its output is then examined and compared to what is expected. Dynamic execution is applied as a technique to detect defects and to determine quality attributes of the code.

Whatever the size of project, software verification and validation greatly affects software quality. Typically, 20 to 50 errors per 1000 lines of code are found during development, and 1.5 to 4 per 1000 lines of code remain even after system testing (see Gibson 1992). Each of these errors could lead to an operational failure or non-compliance with some requirements.

Every project must verify and validate the software it produces. This is done by (see ESA Board for Software Standardization and Control 1995):

- checking that each software item meets specified requirements
- checking each software item before it is used as an input to another activity
- ensuring that the amount of verification and validation effort is adequate to show each software item is suitable for operational use

Figure 4.1 shows the life cycle verification approach. In particular:

1. software requirements must be verified with respect to the user requirements by means of the SVVP and system test
2. the architectural design must be verified with respect to software requirements by means of the SVVP and detailed design and production
3. unit tests verify that the software subsystems and components work correctly in isolation, and as specified in the detailed design
4. integration tests verify that the major software components work correctly with the rest of the system, and as specified in the architectural design
5. system tests verify that the software system meets the software requirements
6. acceptance tests verify that the software system meets the user requirements

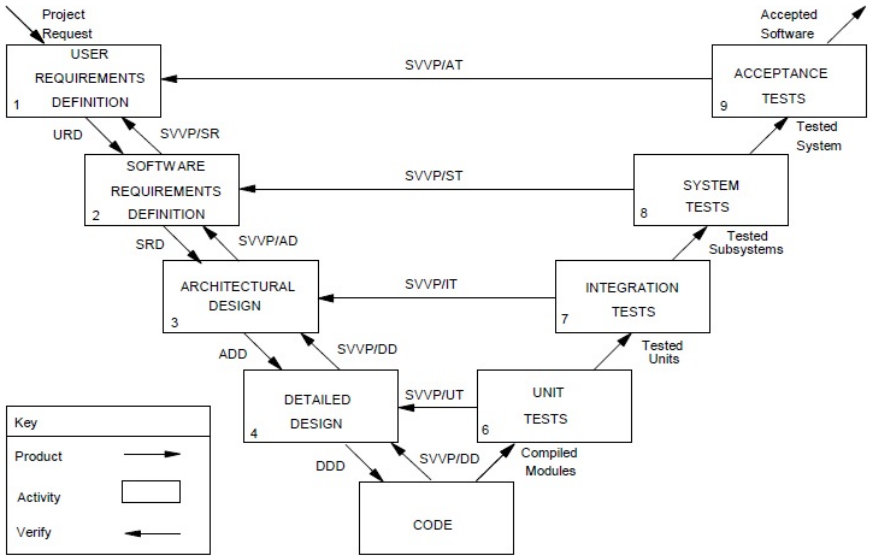

Figure 4.1: Life cycle verification approach (see ESA Board for Software Standardization and Control 1995)

The activities to be conducted during the software verification and validation phase are described in the **Software Verification and Validation Plan** (SVVP).

4.2 The Euclid proto-E2E Verification and Validation Plan

A "**Euclid E2ES Verification and Validation Plan**" has been prepared (see Battaglia & Romelli 2015c) for the implemented proto-E2ES to define:

1. a **Software Verification Plan**
2. a **Scientific Verification Plan**

4.2.1 The Software Verification Plan

The goal of the **Software Verification Plan** is to check the consistency and meaningfulness of output data resulting from the entire simulation chain, i.e. that the input data correctly propagates through the different modules of the integrated proto-E2ES, and that simulation output products are within the identified figure of merit (see paragraph 3.4.1). The software verification plan defines the test cases that have been used for the verification of the EUCLID E2E at system level with the following assumptions:

- the EUCLID proto-E2ES verification starts after the software integration within the framework. The software integration within the framework includes tests at module level, and it also checks that the behavior of each module within the infrastructure is identical to the stand-alone behavior (see figure 4.2).
- the EUCLID E2E verification is performed at system level. The verification process evaluates the correct integration between the modules and it checks the interfaces at functional level for correct information exchange.

The software verification focuses, then, on the functional propagation of the data along the simulator chain, checks the correct implementation of the EUCLID proto-E2ES architecture and interfaces and the consistency of the output data at functional level, and provides the required test data and tools. Four tests have been conceived (see table 4.1)

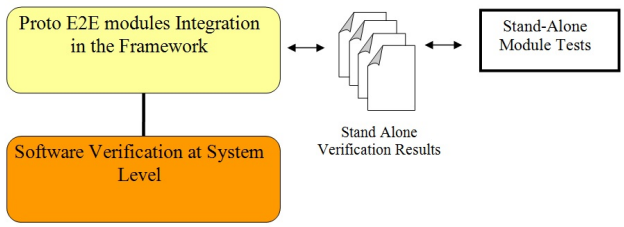

Figure 4.2: Software Integration and Verification activities (see Battaglia & Romelli 2015c)

as well as step-by-step procedures (see figure 4.3).

Test Name	Task	Input	Expected Output
Installation Test (SW_VER_001)	Check the correct reception of the delivery package; verify the correct installation of SW Verification environment	Euclid proto-E2E version delivery package	The installed Euclid proto-E2ES in the verification environment and an installation log file
Integration Test (SW_VER_002)	Verify the correct integration in the framework. It includes test at module level to check that the behavior of each module within the infrastructure is identical to the stand-alone behavior	The installed Euclid proto-E2ES in the verification environment with input file for test at module level	Simulator Status log file with indicators of the functioning of the simulator module by module and modules output files
Architecture and Interfaces Verification Test (SW_VER_003)	Verify the correct implementation of the architecture and interfaces of the Euclid proto-E2ES	The installed Euclid proto-E2ES in the verification environment. A run has already been performed	SimulatorStatus.log file and all the results/output files after the execution of the session
Performance Test (SW_VER_004)	Check the correct interactions between the different modules in the framework, and that the proto-E2ES is able to simulate observations for a predefined scenario in 1 hour	Complete previous run and the baseline scenario	Output files of the modules and running time

Table 4.1: List of test cases for the Software Verification check

4.2.2 The Scientific Verification Plan

The objective of the **Scientific Verification** is to determine whether or not the simulator software complies with the scientific requirements established in the baseline requirements document (see Battaglia & Romelli 2015b), i.e. that the simulator provides output products within the identified figure of merit (see section 3.4.1). Simulation outputs have not been validated for cosmology analysis.

A Scientific Validation Plan defines the test cases that have been used for the scientific validation and evaluates the outputs of the simulator with respect to figures of merit. The Euclid proto-E2ES scientific validation assumes that the software has already been integrated within the environment and it has been verified (see paragraph 4.2.1). Two

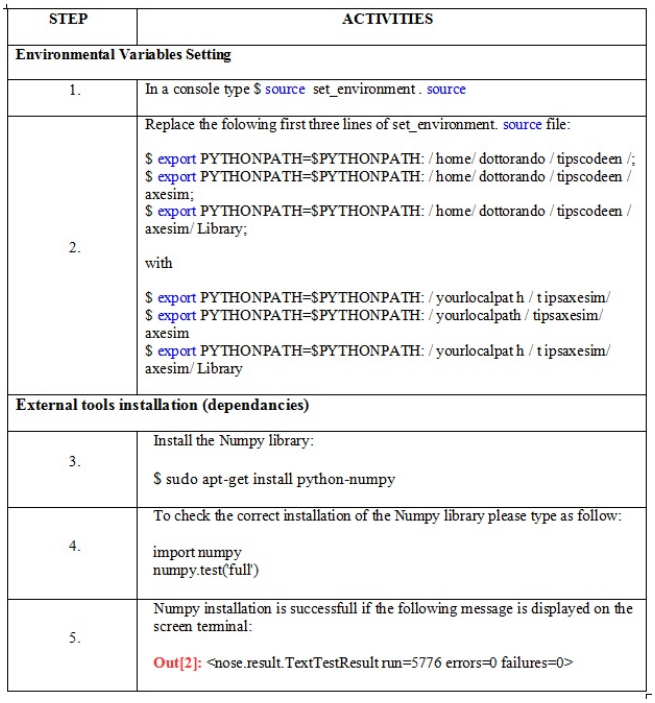

STEP	ACTIVITIES
Environmental Variables Setting	
1.	In a console type $ source set_environment . source
2.	Replace the folowing first three lines of set_environment. source file: $ export PYTHONPATH=$PYTHONPATH: /home/ dottorando / tipscodeen /; $ export PYTHONPATH=$PYTHONPATH: /home/ dottorando / tipscodeen / axesim; $ export PYTHONPATH=$PYTHONPATH: /home/ dottorando / tipscodeen / axesim/ Library; with $ export PYTHONPATH=$PYTHONPATH: /yourlocalpat h / t ipsaxesim/ $ export PYTHONPATH=$PYTHONPATH: /yourlocalpath / tipsaxesim/ axesim $ export PYTHONPATH=$PYTHONPATH: /yourlocalpat h / t ipsaxesim/ axesim/ Library
External tools installation (dependancies)	
3.	Install the Numpy library: $ sudo apt-get install python-numpy
4.	To check the correct installation of the Numpy library please type as follow: import numpy numpy.test('full')
5.	Numpy installation is successfull if the following message is displayed on the screen terminal: Out[2]: <nose.result.TextTestResult run=5776 errors=0 failures=0>

Figure 4.3: Example of step-by-step procedure extracted from Installation Test (see Battaglia & Romelli 2015c)

tests have been conceived (see table 4.2) as well as step-by-step procedures.

Test Name	Task	Input	Expected Output
SC_VER_001	Check that the E2ES is able to • simulate observations for a baseline scenario (see 4.3) • simulate sky scenes of 1 deg square • perform the execution of all simulations resulting from the variation of the specified input parameters (sensitivity analysis)	GlobalParameters.dat (baseline scenario); OperationalTimeline_lite.csv	PA module plots
SC_VER_002	Check the extracted spectra and redshifts	GlobalParameters.dat (baseline scenario); OperationalTimeline_lite.csv	Spectra and redshifts

Table 4.2: List of test cases for the Scientific Verification check

4.3 Baseline Scenario and Testing Facilities

The testing activities described in section 4.2.1 and 4.2.2 have been performed using a very simple input catalog prepared by INAF-IASF Milano. This test scenario, called **baseline scenario**, even if it is not a realistic case, enables a representative simulation to verify the entire pipeline.

The input test catalog is composed of 320 copies of the same source (mag = 15) grouped in 64 sets, each containing five sources (see figure 4.4). Each source has a sequential identification number starting from 1 (lower-left source in the pattern, red circle) to 320 (upper-right source in the pattern). The same spectrum has been associated to the 320 sources constituting our catalog (see 4.5). It is a template stellar spectrum extracted by the Pickles Atlas (`http://www.stsci.edu/hst/observatory/crds/pickles_atlas.html`), representative of a galaxy spectrum for an intermediate-age stellar population, to which three strong emission lines, λ_1, λ_2, λ_3 (see figure 4.4) have been added: $\lambda_1 = 15252\mathring{A}$ (corresponding to the Hα line of the Balmer series), $\lambda_2 = 15665\mathring{A}$ and $\lambda_3 = 17212\mathring{A}$.

The catalog covers a sky patch ranging from 150.04 deg to 151.40 deg in R.A. and from 1.04 deg to 2.48 deg in DEC. The patch of sky is nearly $1.36 \times 1.44\ deg^2$. We know from TIPS (see paragraph 3.5.1) documentation that its field of view is 0.17 deg^2 for a single detector and 0.466 deg^2 for the whole detector array. Figure 4.4 shows the distribution of the sources in our catalog, and the field of view of one detector (gray square) and of the whole array (light red square). To cover the whole catalog, since TIPS uses the lower-left pixel of detector 1 as pointing reference, we need 4 pointings (see figure 4.4). The operational timeline and pointings for the baseline scenario is displayed in table 4.3.

The redshift extraction has been performed by mean of a very simple algorithm, which associates to each of the three emission lines in the source spectrum the Hα line of the Balmer series. The Hα line is commonly used to measure the redshift parameter z and has a wavelength, at rest, equal to 656.28 nm. Taking this into consideration, the extracted redshift can assume the following three values: 1.324 for λ_1, 1.387 for λ_2 and 1.623 for λ_3.

Pointing ID	R.A. [deg]	Dec [deg]	Exposure Time [s]	Band
1	150.04	1.04	560	J
2	150.72	1.04	560	J
3	150.04	1.76	560	J
4	150.72	1.76	560	J

Table 4.3: Operational timeline and pointings for the baseline scenario

The proto-E2ES has been fully installed (dependances included) on a personal computer (Intel i7 @2.20 Ghz, Ram 8 GB, Linux Mint 17.2 Rafaela 64 bit). The Python version used for the E2E development is the 2.6.7.
The software tools that have been used for the proto-E2ES system verification are:

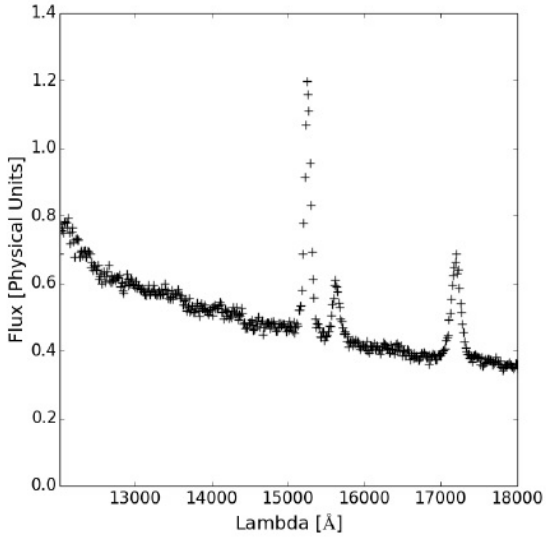

Figure 4.4: The spectrum associated to all the 320 sources constituting the test input catalog. The spectrum has three emission lines at 15252, 15665 and 17212 Å.

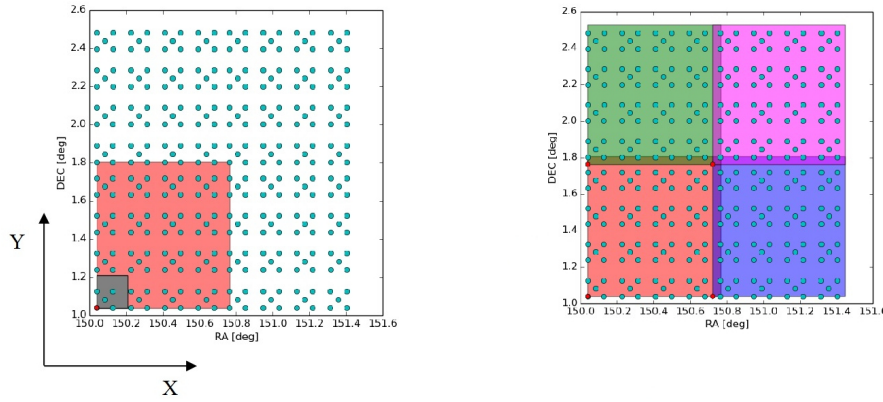

Figure 4.5: ***Left:*** *distribution of the sources in the input catalog for baseline scenario simulation. Gray square: single detector field of view; Red square: field of view of the whole array.* ***Right:*** *Pointing strategy for the baseline scenario simulation. Overlapped areas are due to dithering.*

- IRAF/pyraf
- STSDAS software package
- TIPS
- cvs_table
- ZEUS

with the following python libraries:

- numpy
- scipy
- matplotlib
- pyfits

4.4 Euclid Proto-E2ES Version 1.0 Verification Results

A simulation on the entire input test catalog has been performed. Software verification tests have been executed with success. The performance test (see table 4.1) produced as output a total running time of 40 minutes (request: 1 hour). Details in table 4.4.

Module	**Running Time [s]**
ECSS	0.2
SS	0.2
SCE	0.2
OM	0.2
DS	330 per pointing
OBDG	0.2
DPC	240 per pointing
PA	2 per pointing
Total	2400 (4 pointings)

Table 4.4: Running time recorded during Performance Test execution

Results of the scientific verification have been reported in section 4.4.1, with details of sensitivity analysis outputs (SC_VER_001, see table 4.2), and section 4.4.2.

4.4.1 Scientific Verification: Sensitivity Analysis Results

Scope of the first scientific verification test is to perform a "sensitivity analysis". In this analysis we modify an input parameter (see table 4.2) and check if the simulator output is consistent with modifications.

The investigation has been performed on all parameters contained in the ECSS module operational time-line: the pointing coordinates (R.A. and DEC) and the exposure time.

Pointing Coordinates

In this test we start from a reference point ($R.A._{ref} = 150.7°, DEC_{ref} = 1.8°$) and give a deviation ϵ on one of the coordinates, defining a set of three pointings:

1. reference point, p_{ref}
2. p_{ref} with R.A. or DEC shifted by -ϵ
3. p_{ref} with R.A. or DEC shifted by +ϵ

What we expect, if the simulator is working properly, is that for big deviations applied to one of the two pointing coordinates, the number of sources detected in both the reference pointing and the shifted one is significantly different with respect to the number of sources in the reference pointing alone.

Right ascension and declination have been analyzed separately and we report first the results relative to the **right ascension** analysis.

For each shifted pointing we computed the $\mathbb{H}$ parameter, defined as:

$$\mathbb{H} = \frac{[\text{counts in } \epsilon] \cap [\text{counts in } p_{ref}]}{[\text{counts in } p_{ref}]} \tag{4.1}$$

where the "counts in ϵ" are the detected sources in the shifted pointing and the "counts in p_{ref}" are the detected sources in the reference pointing. The parameter $\mathbb{H}$ gives an estimation of how many sources are detected both in the reference pointing and in the shifted one, with respect to the reference pointing counts. We provide a table (see table 4.5) with the values of the $\mathbb{H}$ parameter, together with the value of the relative shift ϵ. Figure 4.6 and figure 4.7 shows, respectively, the results of the sensitivity analysis for source detection when $\epsilon = 0.1°$, and the results of the sensitivity analysis for redshift estimation. In both cases (i.e. $p_{ref} - \epsilon$ and $p_{ref} + \epsilon$) about 75% of the expected sources have been detected.

Table 4.5 shows that, as expected, the discrepancy in the detected sources becomes smaller as ϵ decreases. The best agreement is for $\epsilon = 0.0005°$ (see 4.8), when all sources are detected in the $p_{ref} - \epsilon$ case, and 99% of the sources are detected in the $p_{ref} + \epsilon$ one.

$\epsilon[°]$	$\mathbb{H}$	$\epsilon[°]$	$\mathbb{H}$
-0.1	0.72	+0.1	0.75
-0.05	0.79	+0.05	0.93
-0.01	0.99	+0.01	0.94
-0.005	0.95	+0.005	0.95
-0.001	0.96	+0.001	0.99
-0.0005	1.00	+0.0005	0.99

Table 4.5: Sensitivity analysis on R.A. parameter. Estimation of how many sources are detected both in the reference pointing and in the shifted one, with respect to the reference pointing counts ($\mathbb{H}$ parameter) computed for different shifts ϵ. Shift values are not directly related to the pointing precision achieved by the Euclid mission.

We now report the results of the similar analysis performed modifying the **declination** of the reference point. Again, a set of three pointing has been obtained:

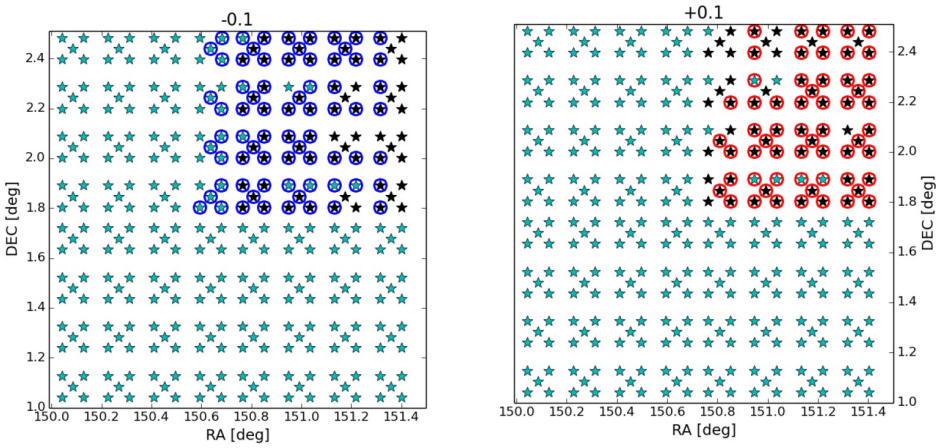

Figure 4.6: Source detection - Sensitivity analysis results for $R.A. \pm \epsilon = 0.1°$. Black stars are the sources detected simulating the reference point; blue circles are the sources detected simulating the $R.A. - \epsilon$ pointing, while red circles are those for $R.A. + \epsilon$ pointing.

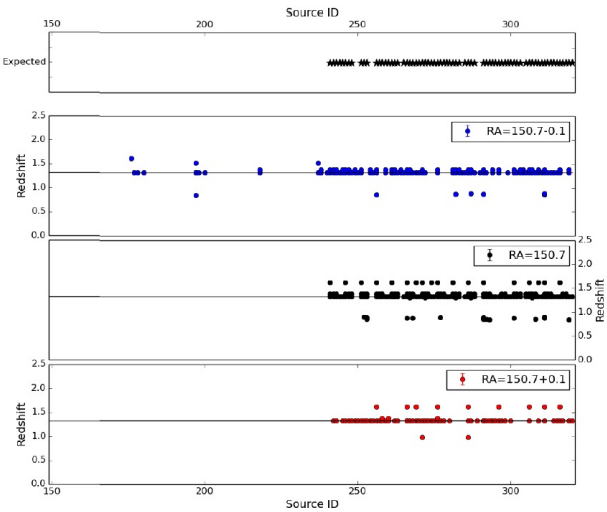

Figure 4.7: Redshift z vs. ID plot - Sensitivity analysis results for $R.A. \pm \epsilon = 0.1°$. Color coding is the same as for source detection plots (see 4.6). Expected detected sources (i.e. sources detected in p_{ref} simulation) are in the top plot. The shift in R.A. can truncate the spectrum of some sources in one pointing and that of other sources in another pointing. This is the reason for the observed statistics in the redshift extracted in the three pointings.

1. $R.A._{ref}, DEC_{ref}$
2. $R.A._{ref}, DEC_{ref} - \epsilon$
3. $R.A._{ref}, DEC_{ref} + \epsilon$

Figure 4.10 and figure 4.11 shows, respectively, the sensitivity analysis results for source detection on DEC variation when $\epsilon = 0.1°$, and for redshift estimation. For $DEC_{ref} -$

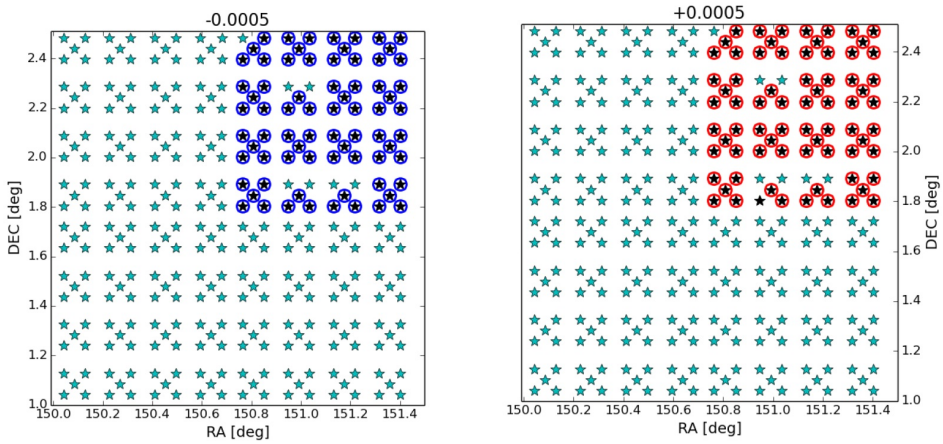

Figure 4.8: Source detection - Sensitivity analysis results for $R.A. \pm \epsilon = 0.0005°$. Black stars are the sources detected simulating the reference point; blue circles are the sources detected simulating the $R.A. - \epsilon$ pointing, while red circles are those for $R.A. + \epsilon$ pointing.

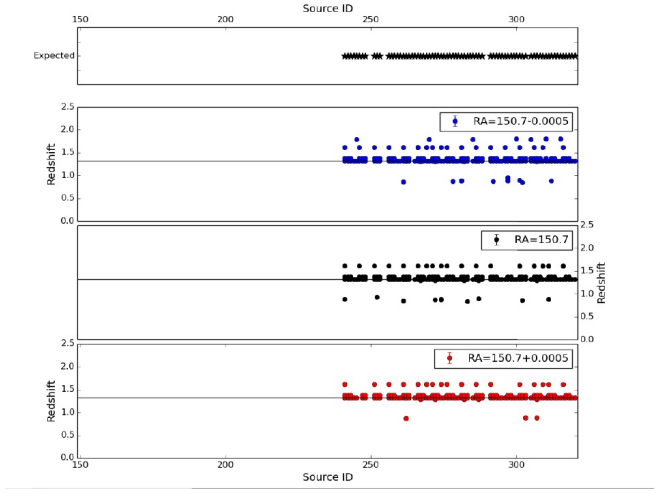

Figure 4.9: Redshift z vs. ID plot - Sensitivity analysis results for $R.A. \pm \epsilon = 0.0005°$. Due to the small shift in R.A., the redshift extracted in the three pointings are very similar.

ϵ 77% of the sources have been detected, while in the case $DEC_{ref} + \epsilon$ only 46% of the expected sources have been detected. The discrepancy observed in the two cases ($DEC_{ref} - \epsilon$ and $DEC_{ref} + \epsilon$) is due to the fact that when a shift is applied in DEC some sources exit from the catalog. The best agreement is obtained for $\epsilon = 0.0005$, when in both $DEC_{ref} \pm \epsilon$ cases the 99% of the expected sources have been detected (see also table 4.7).

$\epsilon[°]$	$\mathbb{H}$	$\epsilon[°]$	$\mathbb{H}$
-0.1	0.77	+0.1	0.46

$\epsilon[^\circ]$	$\mathbb{H}$	$\epsilon[^\circ]$	$\mathbb{H}$
-0.05	0.74	+0.05	0.69
-0.01	0.86	+0.01	0.60
-0.005	0.83	+0.005	1.00
-0.001	0.97	+0.001	0.99
-0.0005	0.99	+0.0005	0.99

Table 4.6: Sensitivity analysis on DEC parameter. Estimation of how many sources are detected both in the reference pointing and in the shifted one, with respect to the reference pointing counts ($\mathbb{H}$ parameter) computed for different shifts ϵ. Shift values are not directly related to the pointing precision achieved by the Euclid mission.

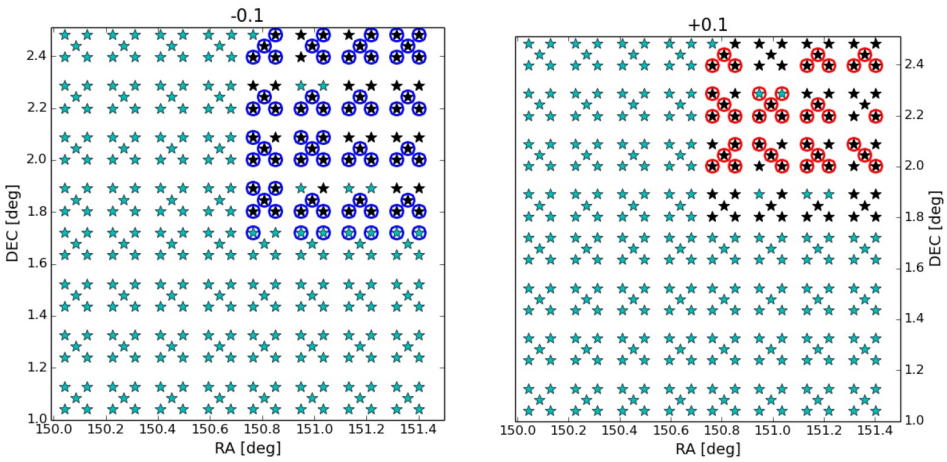

Figure 4.10: Source detection - Sensitivity analysis results for $DEC \pm \epsilon = 0.1°$. Black stars are the sources detected simulating the reference point; blue circles are the sources detected simulating the $DEC - \epsilon$ pointing, while red circles are those for $DEC + \epsilon$ pointing.

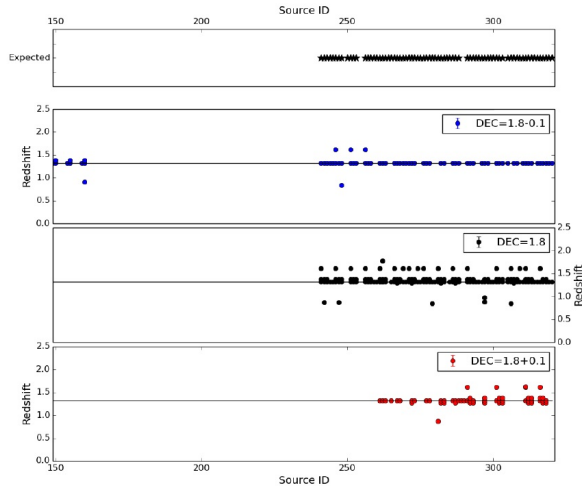

Figure 4.11: Redshift z vs. ID plot - Sensitivity analysis results for $DEC \pm \epsilon = 0.1°$. Color coding is the same as for source detection plots (see 4.6). Expected detected sources (i.e. sources detected in the reference point simulation) are in the top plot.

Exposure Time

In this second analysis we varied the NISP exposure time and verified the behaviour of the simulator. To perform this test the "Exposure Time Calculator" (ETC-42) software tool has been used (see Gross et al. 2015). ETC-42 is an "open" ETC that is usable by standard astronomical community and by instrument specialists. It is generic enough to be adaptable to any new project : site, instrument, target and operation mode. As any ETC, the goal is to estimate the exposure time needed with respect to source, site, instrument and observation parameters specifications.

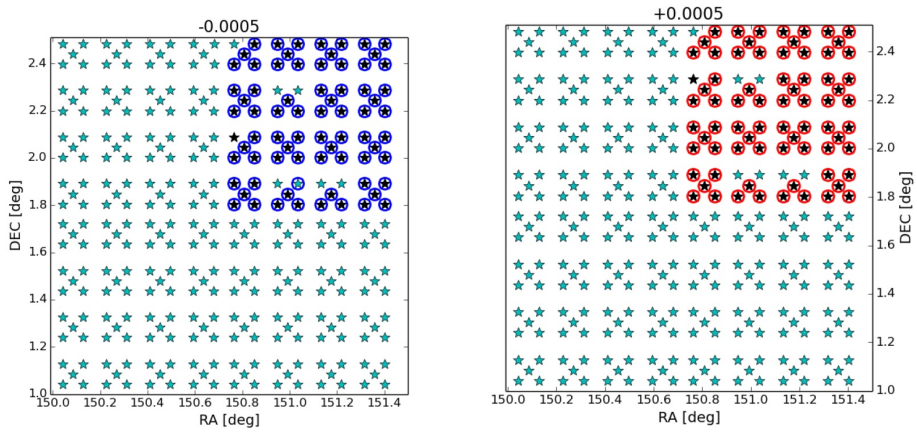

Figure 4.12: Source detection - Sensitivity analysis results for $DEC \pm \epsilon = 0.0005°$. Black stars are the sources detected simulating the reference point; blue circles are the sources detected simulating the $DEC - \epsilon$ pointing, while red circles are those for $DEC + \epsilon$ pointing.

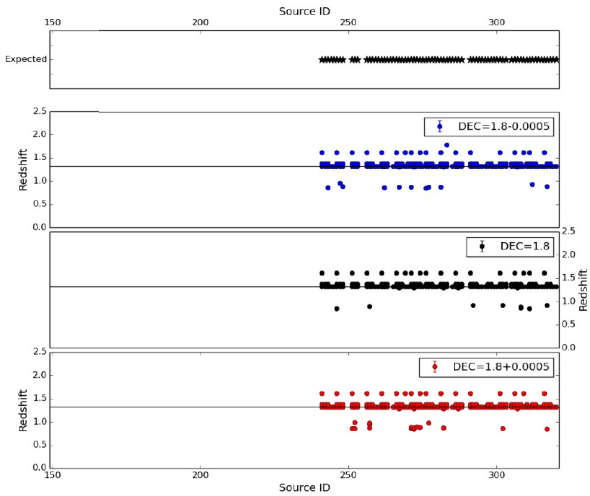

Figure 4.13: Redshift z vs. ID plot - Sensitivity analysis results for $DEC \pm \epsilon = 0.0005°$.

Using ETC-42 we verified that the exposure time considered up to now (i.e. 560 s) is the one required to meet the specified NISP flux limit of $3 \times 10^{-16}\,\mathrm{erg\,cm^{-2}}$ [1] at $1600\,\mathrm{nm}$ with a $SNR > 3.5$. We used the NISP instrumental parameters used as input by TIPS to configure the instrumental environment (i.e. dark noise $= 0.1\,\mathrm{electrons\,pixel^{-1}\,s^{-1}}$; readout noise $= 6.0\,\mathrm{electrons\,pixel^{-1}}$, and pixel scale $= 0.3\,\mathrm{arcsec\,pixel^{-1}}$) and we simulate the exposure time needed to detect a $1600\,\mathrm{nm}$ line with the required NISP flux limit. The exposure time found is of $561.88\,\mathrm{s}$ in accordance with the NISP instrument requirements.

[1] This number has been recently changed to $2 \times 10^{-16}\,\mathrm{erg\,cm^{-2}}$.

The sensitivity analysis has been performed by simulating the reference point ($R.A._{ref} = 150.7°, DEC_{ref} = 1.8°$) with different exposure times, and using as figure of merit the $\mathbb{H}$ parameter and purity (i.e. the fraction of spectra correctly measured above a given line flux limit, see 3.4.1). The investigation shows that the minimum exposure time requested from the E2ES in order to be able to detect the sources and extract the spectra is 100 s (see figure 4.14, 4.15 and table 4.7). This is in agreement with the fact that the sources contained in our input catalog have magnitude equal to 15.

Exposure Time [s]	**Purity**	$\mathbb{H}$
1	0.05	0.68
10	0.29	0.88
100	0.99	1.00
140	1.00	0.99
280	0.99	1.00
560	0.99	1.00

Table 4.7: Sensitivity analysis on exposure time. All sources are detected with 99% purity starting from an exposure time of 100 s.

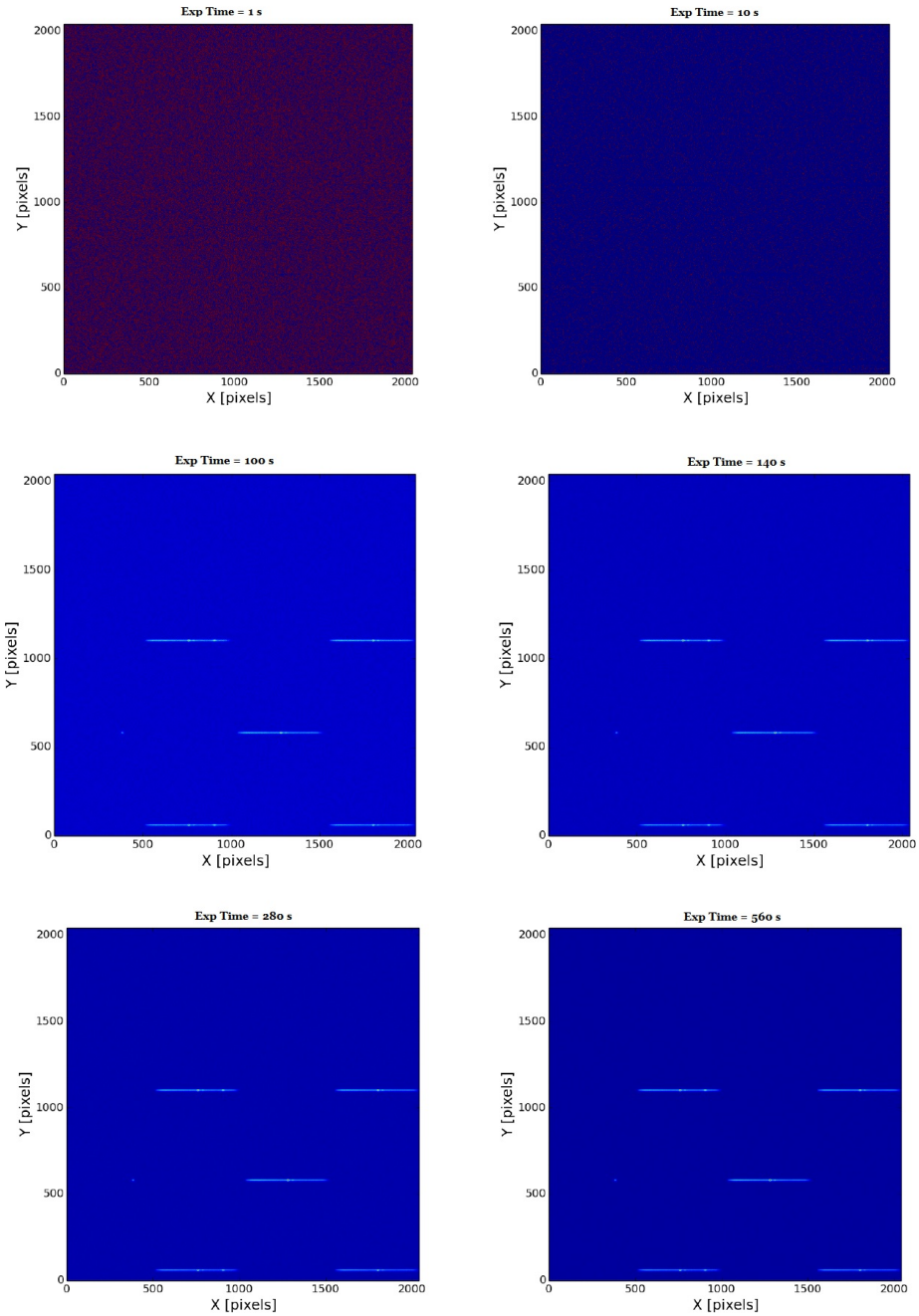

Figure 4.14: Exposure Time - Sensitivity analysis results for six different exposure times. Low exposure times images are very noisy: source detection is possible starting from an exposure time of 100 s.

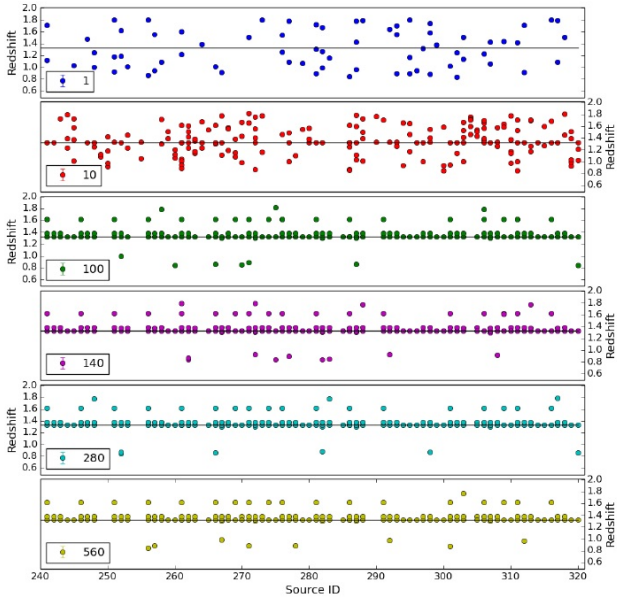

Figure 4.15: Exposure Time - Sensitivity analysis results for six different exposure times. Low dispersion on redshift evaluation starting from an exposure time of 100 s.

4.4.2 Scientific verification: Extracted Spectra and Redshifts

The goal of the second scientific verification test is to check the extracted spectra and redshifts with respect to the following figures of merit: the redshift measurement, completeness, purity, redshift errors and detection limit (see section 3.4.1). A simulation has been performed using our test catalog. Table 4.8 shows the values obtained for completeness, purity and redshift errors. Figures 4.16 and 4.17 display, respectively, the sources detected by the simulator with respect to the complete input catalog, and the redshift values measured for each source.

Figure of merit	**Simulation Output**	**Requirement**
Completeness	0.82	0.45
Purity	0.77	0.80
Redshift Error min	0.002	0.002
Redshift Error max	0.017	0.0027
Redshift Error mean	0.005	n/a

Table 4.8: Completeness, purity and error on redshift measurement for a complete input catalog

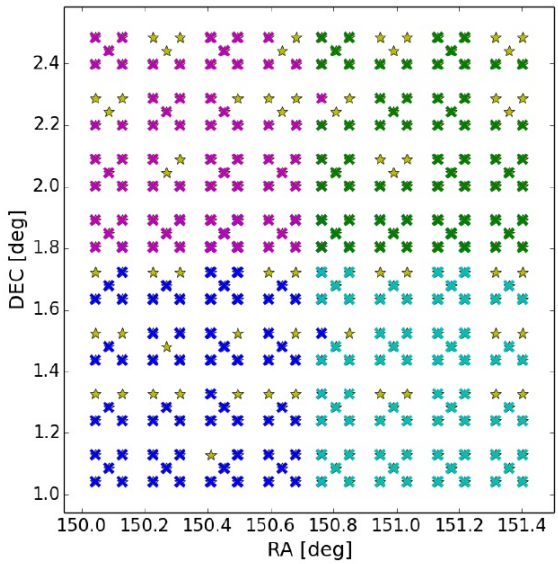

Figure 4.16: The image show the complete input catalog (yellow stars) with the sources detected by the E2ES (crosses with different colors for the four pointings). For mission requirements (see Euclid Project Team 2013)

An analysis of the results show that:

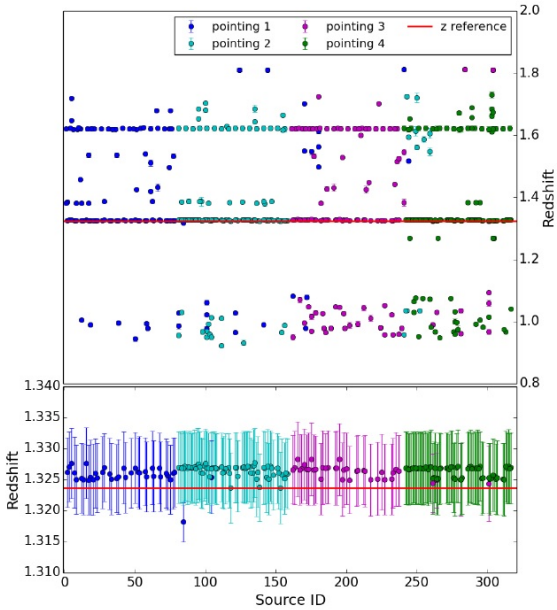

Figure 4.17: The image show, in the upper part, the redshift values measured for each source with respect to the reference redshift (red line). The lower part of the plot display a magnification of the correct redshift values.

1. we achieve a completeness of 0.82 with respect to a required 0.45. This is due to the fact that our input catalog contains sources of magnitude $m \cong 15$, while it is expected that Euclid will observe sources down to magnitude $m \cong 24$.
2. we detect the 77% of the input sources, instead of the required 80%. This is due to the fact that purity is computed considering all the sources in which one of the identified lines corresponds to the real H_α line. The algorithm for redshift extraction is indeed still not able to assign a reliability value to the measured redshift.
3. two lines are detected for the majority of the sources: $\lambda 1 \cong 1525.2nm$ ($z1 \cong 1.324$), $l2 \cong 1721.2nm$ ($z1 \cong 1.623$). The algorithm is still not able to identify and remove spurious detection (see scattered regions in the upper part of figure 4.17)
4. the measured redshift values for the correct H_α line are higher than the input catalog ones
5. 45% of the total detected sources corresponds to a single redshift measure. Measures which are not related to one of the redshifts of our input catalog (i.e. 1.324, 1.387 and 1.623) have been labeled as "spurious". The percentage of "single redshift sources" associated to the redshifts contained in the input catalog are as in figure 4.18. Only 5% of the single redshift sources are related to spurious measures.

The error on measured redshifts is related to the spread in the spectral line, and it has been obtained by propagation of uncertainty. Sky simulation and spectra extraction are performed by external tools (i.e. TIPS and aXe). Therefore it is not possible for us make

second order corrections and redshift error can be considered as upper limits on the uncertainty of the redshift measurement.

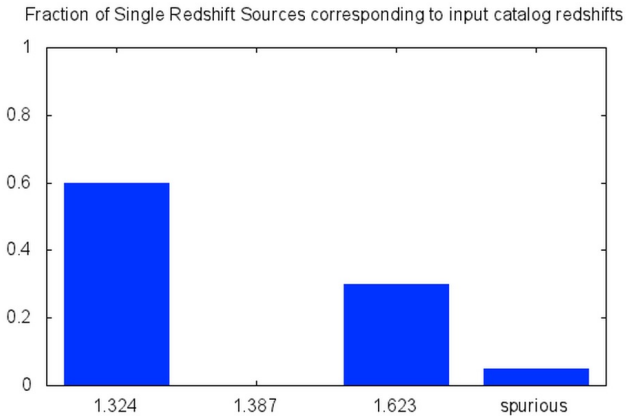

Figure 4.18: Percentage of single redshift sources associated to the redshifts contained in the input catalog. "Spurious" sources are those with a redshift not associated to one of the three contained in the input catalog.

4.5 Euclid Proto-E2ES Version 2.0 Verification Results

The same test scenario used for validate the proto-E2ES version 1.0 has been used also for testing the version 2.0 of the simulator. The check on extracted spectra and redshifts with respect to figures of merit produced the following results:

Figure of merit	**Simulation v1.0 Output**	**Simulation v2.0 Output**	**Requirement**
Completeness	0.45	0.99	0.82
Purity	0.80	0.90	0.77
Redshift Error min	0.003	0.002	0.002
Redshift Error max	0.0013	0.0027	0.017
Redshift Error mean	0.007	n/a	0.005

Table 4.9: Completeness, purity and error on redshift measurement for a complete input catalog simulated by version 1.0 and version 2.0 of the proto-E2ES

The increase in the completeness and purity output parameters comes from the improvement in spectral line detection obtained by substituting the IRAF software with a dedicated algorithm. The faintest spectral line also is now detected for the majority of the sources (see figure 4.19). Furthermore, the scatter between the correct redshift and the catalog value is negligible, and scattered regions are thinner.

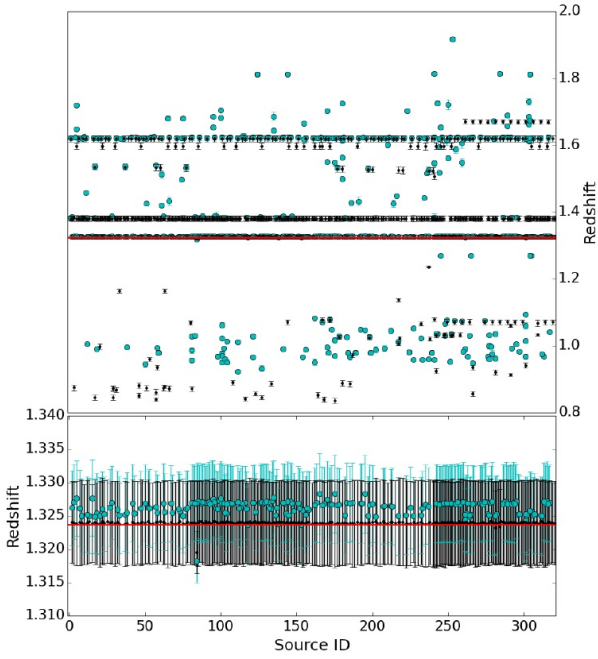

Figure 4.19: The image show, in the upper part, the redshift values measured from E2ES version 1.0 (cyan dots) and from version 2.0 (black dots) for each source of the input catalog. Red line is the reference redshift. The lower part of the plot display a magnification of the correct redshift values.

CHAPTER 5

Development of a Validation Process for the NISP Spectra Location

5.1 Introduction

During the foreseen six years of the survey, Euclid will deliver an unprecedented large volume of data for an astronomical space mission. The spacecraft will collect more than 500,000 visible and near infrared images that will be transferred to Earth on daily basis cadence. Furthermore, a large volume of ground-based data from optical surveys like DES, Pan-STARRS or others is used for calibrations, quality control tasks and scientific data reduction, specifically for obtaining photometric redshift. Overall, the Euclid input images represent several million of images and about 30 Petabytes of image data (see `https://www.euclid-ec.org/?page_id=2625`).

Detailed data quality control is essential to manage the mission, process data and achieve the science goals. Quality control is performed at the different levels of data processing: quick quality checks are done by the Science Operation Center (SOC), more elaborate quality controls involving full pipeline reductions and calibrations are done by the Instrument Operation Teams.

The spectroscopic data produced by the NISP instrument will be validated (i.e. determine whether they satisfy specified requirements, see 4.1) through the verification of the SIR Processing Function (see section 5.2) data products. It is important to stress here that the accuracy of the spectroscopic redshift measurements performed by Euclid depends very strictly on the accuracy of the spectroscopic data wavelength calibration. This in turn depends on the determination of the wavelength scale zero point, which relies on the precise measurement of the position of each object in the NISP field of view during the spectroscopic exposures. These positions are not directly observable using the spectroscopic data themselves. It will therefore be necessary to use zeroth-order spectra produced by relatively bright stars within each spectroscopic exposure.

Exploiting the experience gained on the validation of the Euclid proto-E2ES (see section 4), from May 2016 I have been involved in a collaboration with INAF-IASF Milano to assess if the wavelength calibration accuracy can be validated using spectra of bright stars within the spectroscopic data set produced by the SIR PF. Activities have been performed under the supervision of the SIR OU leader, Dr. M. Scodeggio.

5.2 The SIR Processing Function: Architecture and Validation Approach

The SIR PF is the function in charge of the reduction of the NISP spectroscopic data, starting from raw data to produce one-dimensional spectra that are fully wavelength and flux calibrated, and corrected for contamination from nearby objects. The PF is divided into two main blocks: the *pre-processing* block, to remove detector signature (bad pixels, dark current, pixel non linearity, detector persistence, cosmic), and the *spectra extraction* one. Spectra extraction is performed through the following steps (see figure 5.1)

1. coarse and fine spectra location
2. global background estimation and subtraction
3. extraction of 2D spectrum
4. estimation of wavelength-dependent pixel illumination and flat fielding
5. two-dimensional spectrum wavelength assignment
6. two- diemnsional spectrum de-contamination flagging
7. one-dimensional spectrum extraction
8. combination of spectra between different detectors and pointing
9. final one-dimensional spectra production

With the final one-dimensional spectra production the SIR PF tasks end. The emission line fitting and the redshift determination are then executed by the SPE PF (see figure 2.10). The final outputs are catalogs of objects with fitted line wavelengths and redshift.

The SIR PF has a number of fundamental relations with other processing functions. Some of them are presented in the list below:

- from LE1 (see table 2.1) it receives raw NISP spectroscopic frames and housekeeping data
- with NIR it shares the task of preserving information on the previous illumination history of NISP detectors pixels, to help keeping track of detector persistence effects
- with NIR it will share the task of the pre-reduction of the NISP photometric and spectroscopic frames, and the definition of the data products resulting from this pre-reduction
- from MER it will receive the photometric target catalog that will be used for the extraction of spectra, and their de-contamination
- from NIR/MER it will receive information on the astrometric calibration of the NISP focal plane, in order to monitor possible variations in the physical layout of the NISP detectors during the mission, and therefore its impact on the wavelength calibration of the spectra
- from SPE it will receive requirements on the format of the extracted one-dimensional and two-dimensional spectra

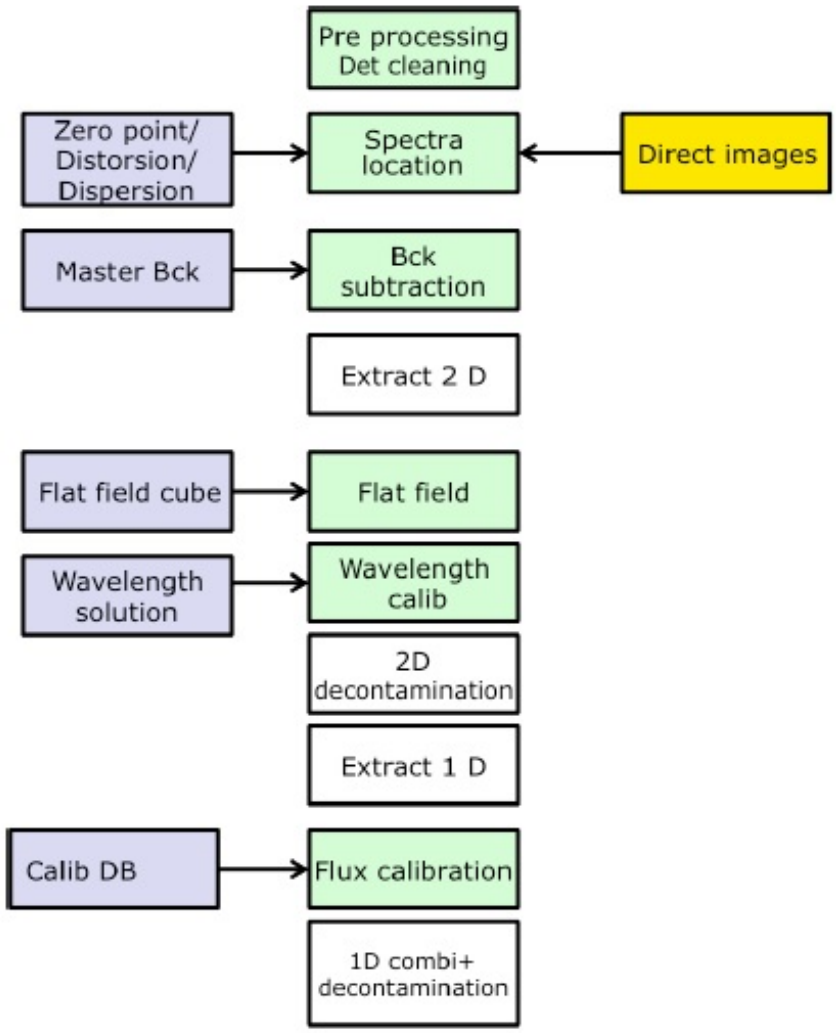

Figure 5.1: The spectroscopy processing chain (see Ealet 2016)

- from SPE it will receive measurements of line position and flux, to be used for validation purposes
- to SPE it will deliver the extracted and calibrated one-dimensional and two-dimensional spectra, for redshift measurements

In parallel to the **scientific pipeline**, within the SIR processing function there are also a **calibration pipeline**, and a **validation pipeline**. Both calibration and validation pipelines are a collection of specific processing elements. The calibration pipeline is in charge of reducing the calibration observations and of preparing the calibration data needed by the scientific pipeline. The **validation processing blocks** have the goal of determine whether SIR PF data products satisfy specified requirements contained in the "Euclid

SGS SIR Requirements Specification Document" (see Scodeggio 2015b).

The high-level architecture of the processing blocks constituting the validation pipeline originates from the "Euclid SGS SIR Processing Function Validation Plan" (see Scodeggio 2015a), whose goal is that to define the validation approach, together with tools and test cases. The validation process is divided into:

- software validation, i.e. the validation of the various processing elements that compose the SIR PF
- data validation, i.e. the validation of the SIR PF data products

Visual inspection of the SIR PF data products is an integral part of all validation steps. Therefore the appropriate data visualization tools are needed throughout the whole validation process. The validation process will evolve with time, and with the availability of different sets of data to be used in the validation procedure.

At the beginning validation is carried out exclusively on the basis of simulated NISP data. Afterward it will be possible to integrate the simulated data with real NISP data obtained during the instrument tests, and finally it will be possible to carry out the final validation based on real NISP in-flight data. This will allow the validation process to be run based on the best available data at any point in time.

The pipeline inherits important **constraints from mission scientific goals**. The accuracy of the spectroscopic redshift measurements, indeed, depends very strictly on the accuracy of the spectroscopic data wavelength calibration. This in turn depends on the accuracy of the dispersion solution across the NISP field of view, and on the determination of the wavelength scale zero point. The spectroscopic redshift accuracy of each detected galaxy shall be better than (see section 2.3):

$$\Delta z \leq 0.001(1+z) \tag{5.1}$$

The redshift z is defined as (see section 1.2) $z = \Delta\lambda/\lambda$. Since $\Delta\lambda << \lambda$, $\sigma_z = \sigma_{\Delta\lambda}/\lambda$.

For small redshifts, $\sigma_z < 0.001$; for high redshifts, $\sigma_z < n$, with $n > 0.001$. Since the requirement on redshift accuracy must be satisfied for all z, it is enough to meet the most stringent condition, i.e. $\sigma_z < 0.001$. For the central frequency of NISP spectra (i.e. $\lambda = 15,000\mathring{A}$), thus, we have:

$$\sigma_{\Delta\lambda} < 15,000\mathring{A} \times 0.001 \tag{5.2}$$

which leads to

$$\sigma_{\Delta\lambda} < 15\mathring{A} \tag{5.3}$$

Since a pixel of the infrared NISP detector corresponds to $13.4\mathring{A}$, we obtain a $\sigma_{\Delta\lambda} \cong 1.1$ pixels. Such error has to be shared between wavelength zero point and dispersion solution as specified by the two following requirements contained in the requirements specification document (see Scodeggio 2015b):

1. **R-SIR-CAL-F-020** "Wavelength Zero Point": the SIR Cal PF shall be able to determine the spectral wavelength zero point of any detected object to better than 0.63 pixels
2. **R-SIR-CAL-F-030** "Wavelength Dispersion Solution": The SIR Cal PF shall use all relevant calibration data to give a spatially varying wavelength solution across the field-of-view, accurate to a level of 0.4 pixels (rms).

The error for the wavelength zero point determination defined in the "R-SIR-CAL-F-020" requirement has a further partition (see Ealet 2016). The factors entering into the accuracy of the wavelength zero point for a single object are:

1. the accuracy of transferring direct image position to grism image (1 σ) is 0.5 pixel, where 0.3 pixel are given to the accuracy of the centroid on the direct image from NISP-P and the other part to the zero order determination in NISP-S
2. the accuracy of transferring the zero order solution to each first order position in the image is 0.3 pixel (trace solution)

Table 5.1 summarizes the wavelength zero point budget.

Reference	**Description**	**Requirement**
R-CAL-B-NS-1110	NISP-P position error	The position of the objects in NISP-P image should be known with a precision better than 0.3 pixel
R-CAL-B-NS-1120	NISP-S zero point determination of NISP-S images	The transfer of the NISP-P position to the NISP-S solution should introduce an error less than 0.5 pixel on the wavelength error
R-CAL-B-NS-1150	NISP-S trace order position determination	The zero order position should be transferred to the first order position wavelength position with an error less than 0.3 pixel

Table 5.1: The Wavelength Zero Point error budget as split out in the NISP Calibration Plan (see Ealet 2016)

The wavelength scale zero point has to be derived:

- for each individual object in the NISP field of view
- for each exposure of the Euclid spectroscopic survey.

The wavelength zero point calibration is part of the "core validation" for SIR PF. This verification relays on the precise measurement of the position of each object in the NISP field of view during the spectroscopic exposures, but the positions of the objects are not directly observable using the spectroscopic data themselves.

It will therefore be necessary to use zeroth-order spectra produced by relatively bright stars within each spectroscopic exposure to map the offset between the directly observable object positions during the photometric imaging exposure, and their non-observable counterpart during the spectroscopic exposure.

As the zeroth-order spectrum has a shape that depends on the spectral energy distribution of the star generating it, it will be necessary to derive a calibration of the zeroth-order position vs. star color-spectral type relation before the beginning of the spectroscopic survey.

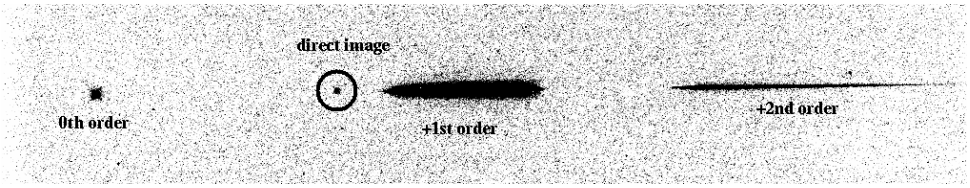

Figure 5.2: Grism observations of a given target field should always be accompanied by a direct image, which is used to locate sources and determine source sizes. The location of sources in direct images is used to establish the wavelength zero-point for extracted spectra. The grism zeroth order, only detectable for brighter objects since it contains about 3% of the total flux, can be mistaken for an emission line. The direct image can be used to determine the position of the zeroth order, and for brighter sources, distinguish unequivocally between the zeroth order and an emission line. Credits: `http://documents.stsci.edu/hst/wfc3/documents/handbooks/cycle22/c08_slitless4.html`

5.3 Description of the code for the validation of the NISP spectra location

Following the coding standards contained in the "SGS Coding Standards" (see Bagot 2015) a validation process for the NISP spectra location has been developed using the Python programming language. The code is open source (under the terms of the GNU Lesser General Public License) and can be found in detail in Appendix A.

The development of the code has been performed in the *LOcal DEvelopment ENvironment* (LODEEN), version 1.2. It is a virtual machine image of a ready to use desktop for Euclid software development on top of developers laptop. The main goal of LODEEN is to provide the same environment for all Euclid developers. This environment has to be as close as possible to the production environment, so developers avoid compatibility problems of their code on production servers. The virtual machine has a Scientific Linux desktop, plus compilers, software and scientific libraries to be Euclid Development Environment (EDEN) compliant. An Integrated Development Environment (with support for C++ and python) and a platform to manage code quality are also included.

The following Python libraries have been used:

1. h5py, to read and write HDF5 files (see http://www.h5py.org/)
2. numpy, for numerical algorithms (see http://www.numpy.org/)
3. matplotlib.pyplot, for plot generation

4. scipy, for interpolation, signal processing, curve fitting, and minimization (see http://www.scipy.org/)

The scope of the code is to validate the NISP spectra location with respect the two following requirements (see section 5.2 and table 5.1):

- the zero order position should be transferred to the first order wavelength position with an error less than 0.3 pixel
- the SIR Cal PF shall use all relevant calibration data to give a spatially varying wavelength solution across the field-of-view, accurate to a level of 0.4 pixels (rms)

The code starts loading the observed stellar spectra from the input catalog, which is provided in the Hierarchical Data Format 5 (HDF5) file format (see HDF Group 2017). HDF5 is an open source technology suite for managing data collections.

All spectra are stored into a dictionary data structure (i.e. associative arrays) where each spectrum is represented by an object of a custom defined class - the "*Spectrum*" class. This class is able to describe a spectrum which is sampled at arbitrary wavelengths, and provides also some methods to process the spectrum itself:

- the *get_resampl_shifted_spectrum* method is used to resample the spectrum at different (arbitrary) wavelengths. The basic idea is to start defining an interpolation on the original spectrum; then we evaluate the interpolation on the final wavelengths array which has been enriched with additional points in order to have ten times the resolution; and finally apply a low-pass filter and decimation to recover the values sampled at the final wavelengths only. The low-pass filtering and decimation is done through the *decimate* function from Signal Processing Library (available here: `https://github.com/mubeta06/python/blob/master/signal_processing/sp/multirate.py`). The entire process is performed in order to avoid loosing fine details that would be under-sampled in the final wavelengths. In this way any arbitrary deformation of the spectrum is possible
- the *remove_zeros* method is used to remove zero valued samples present at the beginning and at the end of the spectrum. These samples are found in input catalog spectra and they correspond not to real measured fluxes, but to undefined values that must be ignored
- the *trim_wavelength* method is used to keep only a desired interval of wavelengths.

Reference stellar spectra, called *templates*, are loaded through the *template_spectrum* function. Templates are read from text files and stored in a dictionary. The following spectral types have been used as templates: F5, G4, K5, and M4 (see 5.3).

The spectra that will be obtained with the Euclid NISP grism are affected by deformations due to the non-ideal nature of the instrument. The mapping between pixels and wavelengths is obtained via a third order polynomial. This is done via the *spectrum_deformation* function, which applies a third degree polynomial to the wavelengths of the input spectrum in the following way:

$$\lambda_{deformed} = \lambda_c + a_0 + a_1 \times (\lambda_{original} - \lambda_c) + a_2 \times (\lambda_{original} - \lambda_c)^2 + a_3 \times (\lambda_{original} - \lambda_c)^3 \quad (5.4)$$

where λ_c is the central wavelength of the original spectrum. In this way the fixed point of the non-zero degree transformations is in the center of the spectrum, and the correlation between the coefficients is then reduced. a_0 represents the **shift** of the spectrum, a_1 is the **rescale factor**, a_2 and a_3 are higher order deformations. The spectrum is not deformed for $a_0 = 0$, $a_1 = 1$, $a_2 = a_3 = 0$.

The displacement in pixel depending on each coefficient of the polynomial can be obtained by computing it at the ends of the spectrum using the actual pixel size and number of pixels in the spectrum. The displacement in pixel for each coefficient is given by:

1. $P_0 = a_0/13.4\mathring{A}$
2. $P_1 = a_1 \times 200$
3. $P_2 = a_2 \times 13.4\mathring{A} \times 200^2$
4. $P_3 = a_3 \times (13.4\mathring{A})^2 \times 200^3$

In order to match the template with the deformed spectrum we apply a deformation to the template (see figure 5.4, and figure 5.5) with a set of coefficients which is varied until the best match is found.

The best match between the observed deformed spectrum and template is obtained through the evaluation of a **merit function**, depending on the coefficients of the polynomial used to deform the template. The merit function is implemented in the code as *normalized_correlation*.

The *normalized_correlation* function takes as arguments the spectrum and the template, and the set of coefficients defining the deformation to be applied to the template. The operations performed by the function are the following:

1. apply the deformation to the template
2. resample the template on the same wavelengths where the stellar spectrum is sampled. Templates are, indeed, sampled with non-constant step, on a wavelength range from $8033.61\mathring{A}$ to $24235.30\mathring{A}$ (4183 points)
3. remove the continuum from the spectrum and the template
4. compute the correlation

The correlation is defined as

$$correlation = \frac{\sum_i S_i \cdot T_i}{\sqrt{(\sum_i S_i^2)(\sum_i T_i^2)}} \tag{5.5}$$

where S_i are the samples of the spectrum and T_i are those of the template both with the continuum removed.

Usually the continuum, which does not carry information about the wavelength, is stronger than spectral lines, so we need to remove it. Otherwise we are dominated by the continuum itself and we lose the weak spectral features. The continuum subtraction is performed by the *get_spectrum_without_continuum* function, which uses, in turn, a python translation of a C source code from the SIR pipeline (see figure 5.6).

In order to find the set of parameters that maximizes the correlation between the spectrum and the template we use a minimization algorithm from the scipy.optimize library, i.e. the "SLSQP" (Sequential Least SQuares Programming) algorithm. The correlation is evaluated for each spectrum-template pair; the resulting set of parameters and correlation values are saved in an array.

5.4 Wavelength Zero Point Validation Results

We investigated the possibility of exploiting stellar spectra as validation tools for the wavelength scale zero point using the spectral library of the NASA InfraRed Telescope Facility (IRTF) on Mauna Kea, Hawaii, USA.

The IRTF Spectral Library is a collection of stellar spectra observed over a wavelength range $0.8 to 5.0 \mu m$ with a resolution of $R \equiv \lambda/\Delta\lambda \approx 2000$ with the medium-resolution spectrograph, SpeX, at the NASA Infrared Telescope Facility (IRTF) on Mauna Kea. The current release covers mainly solar-metallicity late-type stars with spectral types between F and M and luminosity classes between I and V, but also includes AGB stars, carbon and S stars, and L and T dwarfs.

The predicted number of stars contained in a certain sky area has been derived from the Galaxy model called "Trilegal". It is a theoretical tool conceived to help in the science verification of the European Southern Observatory (ESO) imaging public surveys. The software originates from many different pieces of C code developed at Instituto de Física da UFRGS, Max-Planck-Institut für Astrophysik, and Dipartimento di Astronomia di Padova (see `http://stev.oapd.inaf.it/cgi-bin/trilegal`). Five random patches at fixed galactic latitude have been selected (each one 2 squared degrees, i.e. an Euclid pointing), and combined, to build a virtual 10 squared degrees patch, that has been used for counting stars. Results are displayed in the table 5.2 for galactic latitude equal to 80 degrees (worst case, since far from the galactic plane).

Considering the performed analysis, from the IRTF library 66 different spectra have been extracted and processed varying the signal-to-noise ratio to simulate stellar observations of 16 different J-band magnitudes, ranging from 13.0 to 20.5, for a total of 1056 spectra. Spectra have been processed with TIPS (see section 3.5.1) to generate NISP-like ones, which have been extracted with the SIR pipeline with a sampling of $13.4 \mathring{A}$ (i.e. the size of one pixel of the NISP detectors). The wavelength range is between $12,000 \mathring{A}$ and $18,000 \mathring{A}$. The extracted spectra are not contaminated, not deformed, and do not contain cosmic rays hits.

Magnitude Limit	**Number of Stars (mag. limit)**	**Magnitude Bin**	**Number of Stars (mag. bin)**
J_AB < 12.0	267	J_AB = 12.0 (0.5 mag bin)	92
J_AB < 13.0	550	J_AB = 13.0 (0.5 mag bin)	192
J_AB < 14.0	1028	J_AB = 14.0 (0.5 mag bin)	319
J_AB < 15.0	1892	J_AB = 15.0 (0.5 mag bin)	602

Magnitude Limit	Number of Stars (mag. limit)	Magnitude Bin	Number of Stars (mag. bin)
J_AB < 16.0	3402	J_AB = 16.0 (0.5 mag bin)	975
J_AB < 17.0	5949	J_AB = 17.0 (0.5 mag bin)	1563
J_AB < 18.0	9719	J_AB = 18.0 (0.5 mag bin)	2343
J_AB < 19.0	15303	J_AB = 19.0 (0.5 mag bin)	3321
J_AB < 20.0	23031	J_AB = 20.0 (0.5 mag bin)	4288

Table 5.2: Number of stars at different AB magnitudes predicted by the Trilegal model in a 10 squared degrees patch of sky located at b = 80 degrees.

Once the input catalog has been fixed, we started considering the varying of the correlation between stellar spectra and templates as a function of the shift, i.e. the **cross-correlation**. The shift, indeed, is the most critical parameter for determining the location of the spectrum in the field of view.

The correlation has been evaluated for different shift steps on a range from $-220\mathring{A}$ to $+200\mathring{A}$ in order to select the best step that captures all the features of the correlation function without increasing too much the computation load. For each step we computed the RMS difference between the correlation function evaluated with the current step, and the correlation function evaluated with the previous step (resampled at the current step). The RMS difference approaches zero when a further reduction of the step size does not change the correlation function anymore. In this way we can select the best step size.

This analysis has been performed for the first 50 objects of the input catalog. All other sources are, indeed, of a rare spectral type and they are not, then, statistically useful for the validation work. Results are shown in figure 5.7.

A similar investigation has been performed on the scale factor. The correlation has been evaluated for different number of steps taken on a range from 0.9 to 1.1. Since the assessment performed on shift steps showed similar results for all templates, the scale factor analysis has been performed only for F5 and G4 templates. Results are shown in figure 5.8.

At this point, in order to validate the wavelength zero point scale and the dispersion solution with respect to requirements, respectively, *R-CAL-B-NS-1120* and *R-SIR-CAL-F-030* (see 5.1 and section 5.2), the correlation has been computed for all stellar spectra of the input catalog (with shift and scale factor as for assessment output results), and templates. The scatter of the correlation peak position has been evaluated for each magnitude bin, and plotted against magnitude. Figures 5.10 and 5.11 show the results for shift and scale factor, respectively.

A **heat map** (see figure 5.10) has been saved in the "xcorr_template_assessment.h5" file, only for best correlation (i.e. stellar spectrum - matching template case). The heat map represents the values of the correlation as a function of shift and scale factor. These plots have been used to evaluate the behavior of the correlation function near the peak, in

order to ensure that there is a wide enough area of convergence for the minimization algorithm, that is to exclude the presence of local maxima.

Afterwards the correlation has been computed for stellar spectra including second order deformation also. This time only one spectrum for magnitude bin has been selected. Table 5.3 shows the parameters settled for the assessment and the ones computed by the minimization algorithm. Figures 5.12, 5.13 and 5.14 show the error between settled values for a_0, a_1, and a_2 coefficients and the values of the same coefficients computed by the minimization algorithm plotted against magnitude and correlation value.

Parameter	**Settled Value**	**Computed Value**	**Magnitude Bin**	**Correlation Value**
$a_0[\mathring{A}]$, a_1, $a_2[\mathring{A}^{-1}]$	4.0, 1.030, $5{\cdot}10^{-6}$	4.4, 1.029, $5.000{\cdot}10^{-6}$	13.0	0.80
$a_0[\mathring{A}]$, a_1, $a_2[\mathring{A}^{-1}]$	4.0, 1.030, $5{\cdot}10^{-6}$	8.1, 1.028, $5.000{\cdot}10^{-7}$	13.5	0.70
$a_0[\mathring{A}]$, a_1, $a_2[\mathring{A}^{-1}]$	4.0, 1.030, $5{\cdot}10^{-6}$	5.3, 1.030, $2.660{\cdot}10^{-6}$	14.0	0.80
$a_0[\mathring{A}]$, a_1, $a_2[\mathring{A}^{-1}]$	4.0, 1.030, $5{\cdot}10^{-6}$	4.5, 1.029, $5.000{\cdot}10^{-6}$	14.5	0.72
$a_0[\mathring{A}]$, a_1, $a_2[\mathring{A}^{-1}]$	4.0, 1.030, $5{\cdot}10^{-6}$	4.2, 1.028, $6.000{\cdot}10^{-6}$	15.0	0.70
$a_0[\mathring{A}]$, a_1, $a_2[\mathring{A}^{-1}]$	4.0, 1.030, $5{\cdot}10^{-6}$	4.3, 1.028, $3.000{\cdot}10^{-6}$	15.5	0.68
$a_0[\mathring{A}]$, a_1, $a_2[\mathring{A}^{-1}]$	4.0, 1.030, $5{\cdot}10^{-6}$	7.3, 1.028,$4.000{\cdot}10^{-7}$	16.0	0.60
$a_0[\mathring{A}]$, a_1, $a_2[\mathring{A}^{-1}]$	4.0, 1.030, $5{\cdot}10^{-6}$	2.5, 1.031, $4.000{\cdot}10^{-6}$	16.5	0.38
$a_0[\mathring{A}]$, a_1, $a_2[\mathring{A}^{-1}]$	4.0, 1.030, $5{\cdot}10^{-6}$	6.6, 1.027, $9.726{\cdot}10^{-7}$	17.0	0.61
$a_0[\mathring{A}]$, a_1, $a_2[\mathring{A}^{-1}]$	4.0, 1.030, $5{\cdot}10^{-6}$	3.8, 1.028, $5.493{\cdot}10^{-6}$	17.5	0.46
$a_0[\mathring{A}]$, a_1, $a_2[\mathring{A}^{-1}]$	4.0, 1.030, $5{\cdot}10^{-6}$	4.6, 1.030, $4.190{\cdot}10^{-6}$	18.0	0.50
$a_0[\mathring{A}]$, a_1, $a_2[\mathring{A}^{-1}]$	4.0, 1.030, $5{\cdot}10^{-6}$	7.3, 1.016, $2.533{\cdot}10^{-7}$	18.5	0.45
$a_0[\mathring{A}]$, a_1, $a_2[\mathring{A}^{-1}]$	4.0, 1.030, $5{\cdot}10^{-6}$	3.2, 1.019, $5.671{\cdot}10^{-8}$	19.0	0.30
$a_0[\mathring{A}]$, a_1, $a_2[\mathring{A}^{-1}]$	4.0, 1.030, $5{\cdot}10^{-6}$	1.4, 1.004, $-5.857{\cdot}10^{-7}$	19.5	0.30
$a_0[\mathring{A}]$, a_1, $a_2[\mathring{A}^{-1}]$	4.0, 1.030, $5{\cdot}10^{-6}$	1.7, 1.034, $2.280{\cdot}10^{-6}$	20.0	0.145
$a_0[\mathring{A}]$, a_1, $a_2[\mathring{A}^{-1}]$	4.0, 1.030, $5{\cdot}10^{-6}$	0.397, 1.003, $2.379{\cdot}10^{-8}$	20.5	0.048

Table 5.3: Correlation assessment results for stellar spectra including second order deformation. The table shows the values of the polynomial coefficient settled and those found by the minimization algorithm (i.e. the Sequential Least SQuares Programming algorithm). A drop in the correlation value is evident for fainter stars.

Also in this case heat maps have been produced in order to exclude the presence of local maxima. Figure 5.15 show three example of such heat map for a high, medium and low magnitude source.

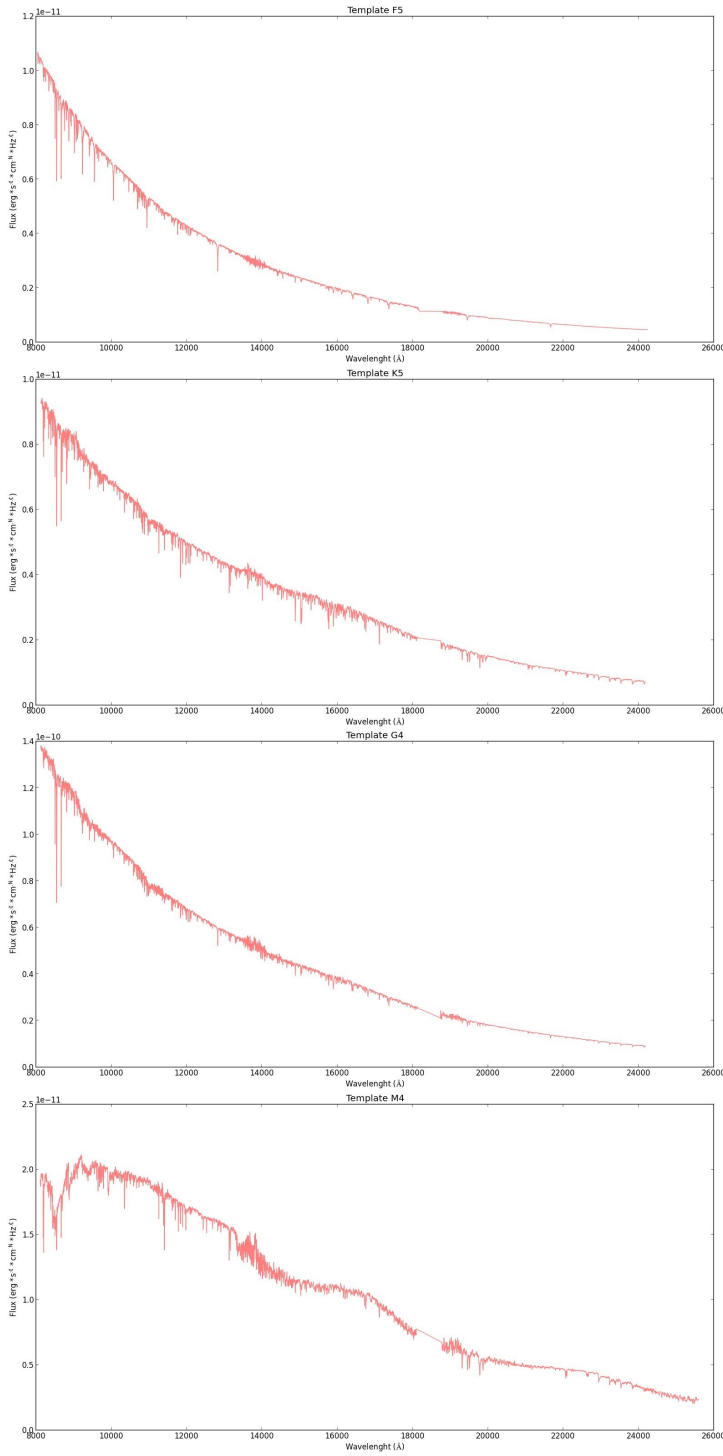

Figure 5.3: The reference stellar spectra used for zeroth order calibration with respect to spectral type.

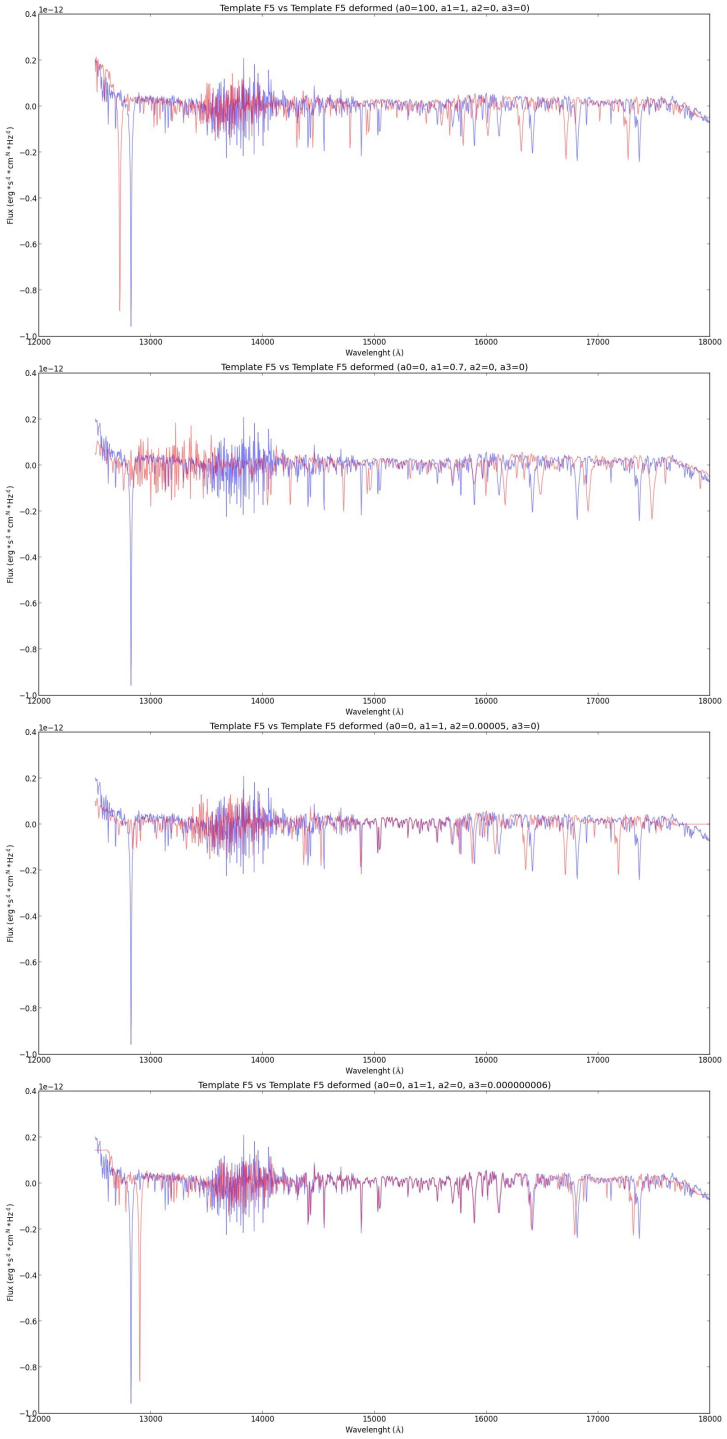

Figure 5.4: F5 template with continuum subtracted and deformed in different ways (from top to bottom): 100Å shift, rescale only ($a_1 = 0.7$), second order deformation only ($a_3 = 5 \times 10^{-5}$), and third order deformation only ($a_3 = 6 \times 10^{-9}$).

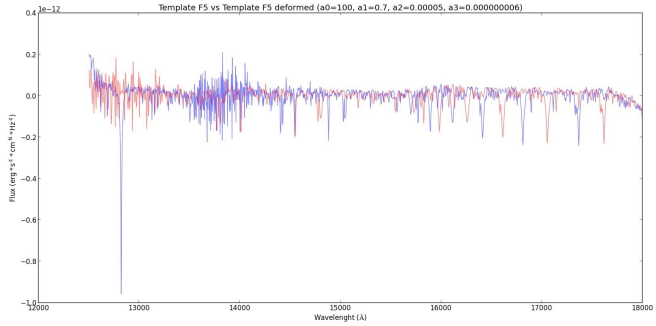

Figure 5.5: F5 template with continuum subtracted and deformed in a complex way. Coefficients of the polynomial are the following: $a_0 = 100$, $a_1 = 0.7$, $a_2 = 5 \times 10^{-5}$, $a_2 = 6 \times 10^{-9}$.

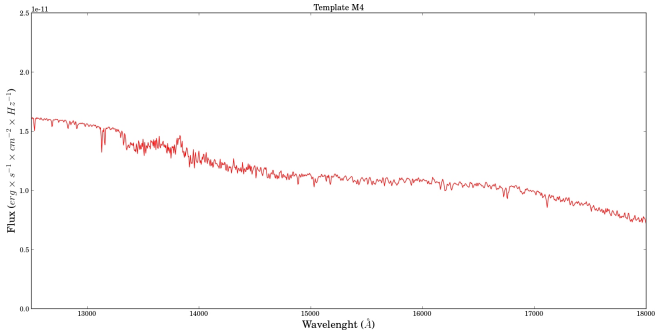

Figure 5.6: The resampled M4 stellar template with continuum removed using the get_spectrum_without_continuum. No deformation applied.

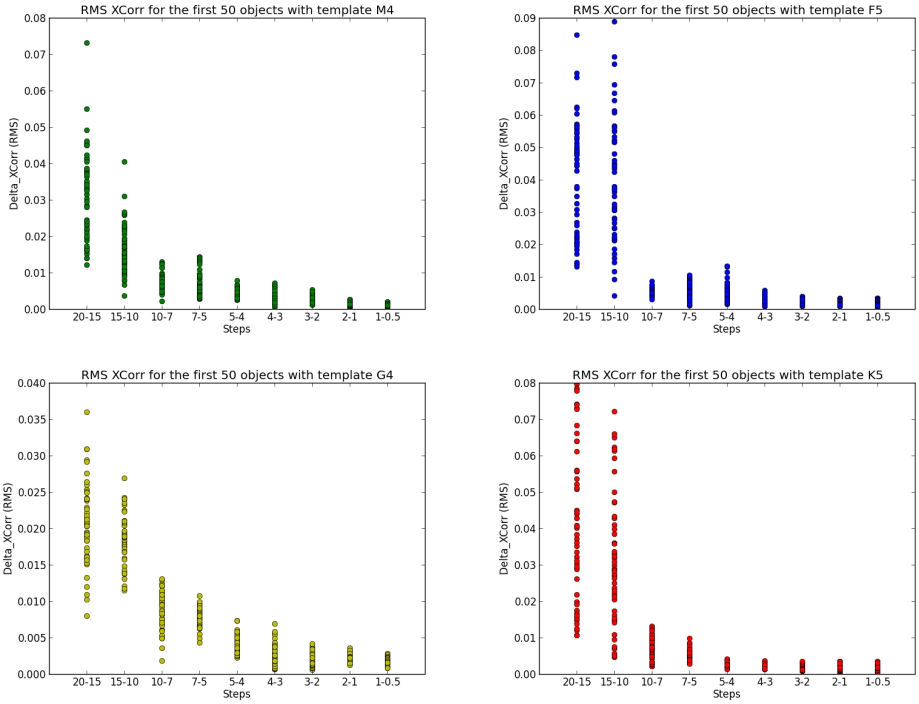

Figure 5.7: Plots show the RMS difference between the correlation function evaluated with a shift step, and the correlation function evaluated with the previous shift step. The analysis has been performed for the first 50 stars of the input catalog cross-correlated with all templates. A shift step of 4Å resulted as the best choice.

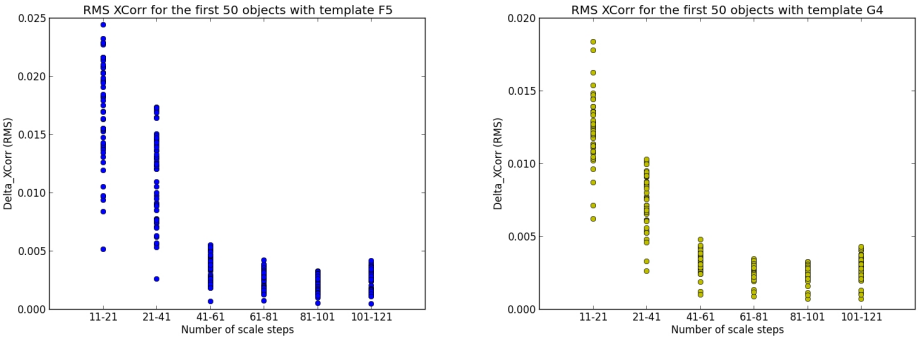

Figure 5.8: Plots show the RMS difference between the correlation function evaluated with a number of scale factor steps, and the correlation function evaluated with the previous number of scale factor steps. The analysis has been performed for the first 50 stars of the input catalog correlated with F5 and G4 templates. A number of scale factor steps of 80 (i.e. a spectrum resolution of 0.0025) resulted as the best choice.

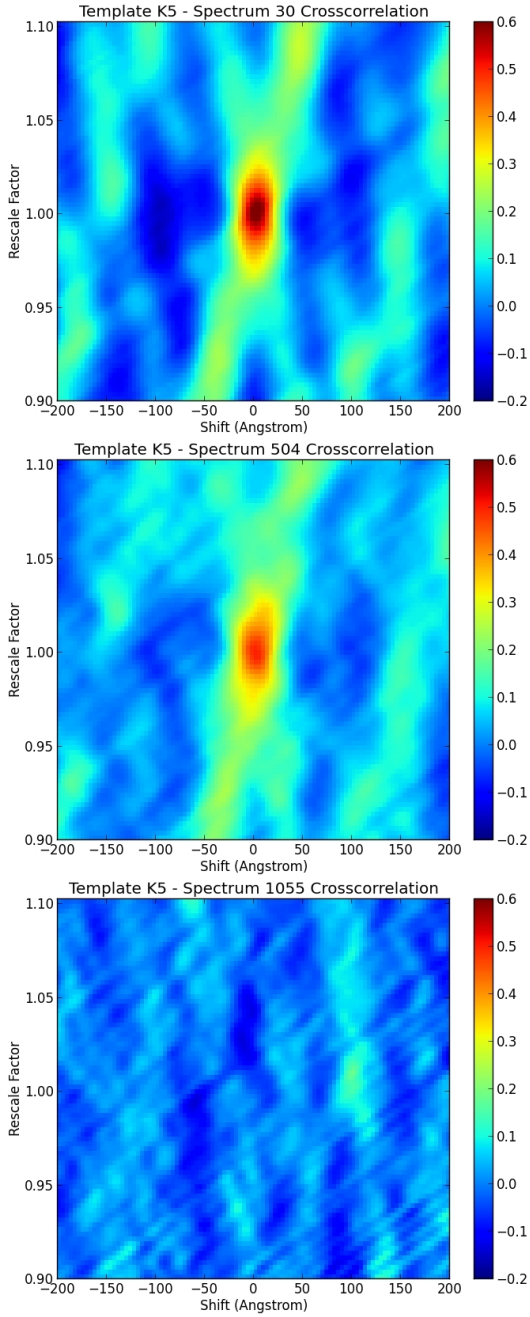

Figure 5.9: Heat maps showing the correlation as a function of shift and scale factor for K5 template and stellar spectra of AB magnitude, from top to bottom, equal to 13.0, 16.5 and 20.5 respectively. For brighter stars a correlation peak is well visible for shift (a_0) = 0 and scale factor (a_1) = 1. On the contrary, the spectrum of the faintest star is too noisy to produce a correlation peak. One can see that the correlation function shows "ridges" that cross at the peak. These ridges are due to the presence of small, localized spectral features (i.e. spectral lines) that are put in the matching position with the template lines for a whole set of parameters, and not only at the peak. The set of parameters includes the peak, and each different feature has a different set.

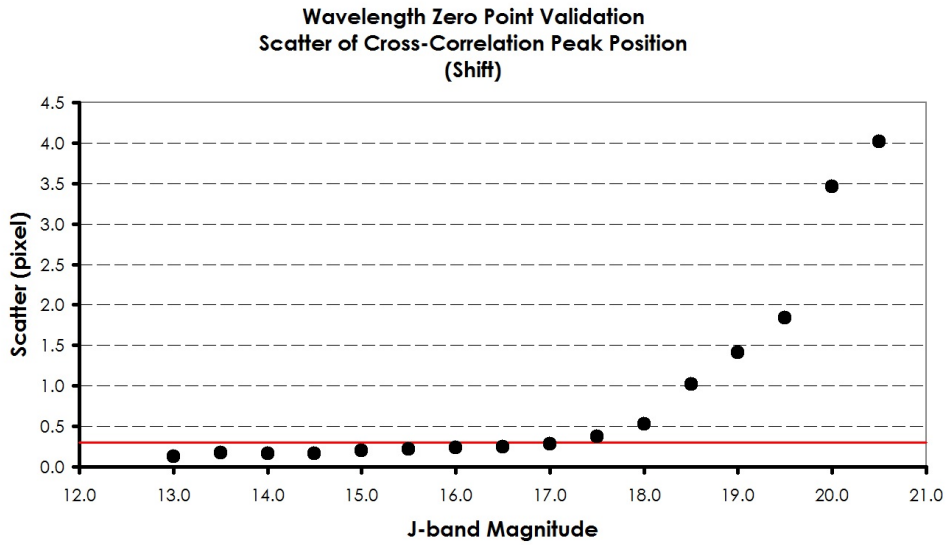

Figure 5.10: Wavelength zero point validation results. The scatter of the cross-correlation peak position for the different magnitude bins has been plotted against the magnitude itself. The red line marks the requirement. Results show that the error in the wavelength zero point is less than 0.3 pixel for stellar spectra up to J-band magnitude = 17.0

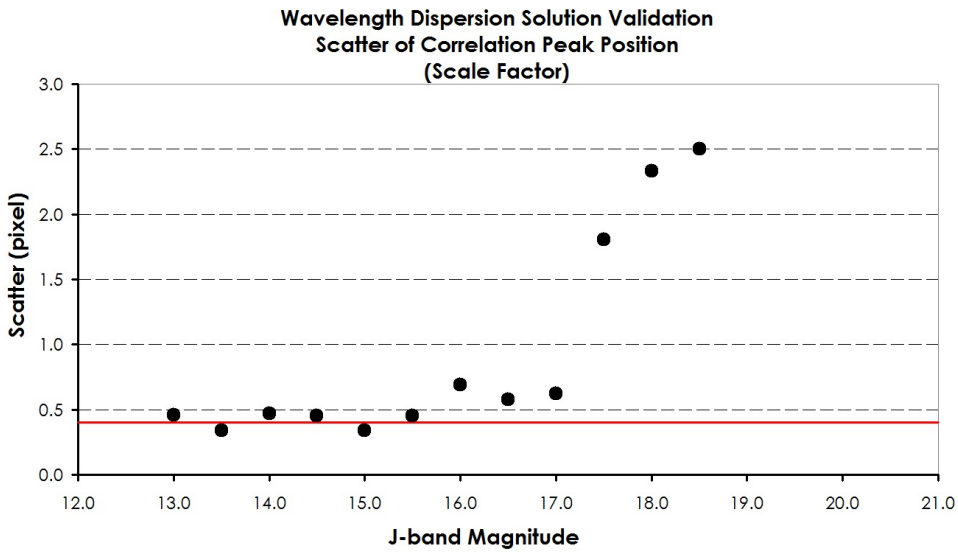

Figure 5.11: Dispersion solution validation results. The scatter of the cross-correlation peak position for the different magnitude bins has been plotted against the magnitude itself. The red line marks the requirement. Results show that the spatially varying wavelength solution across the field-of-view is accurate to a level of 0.4 pixels for stellar spectra up to J-band magnitude = 15.5

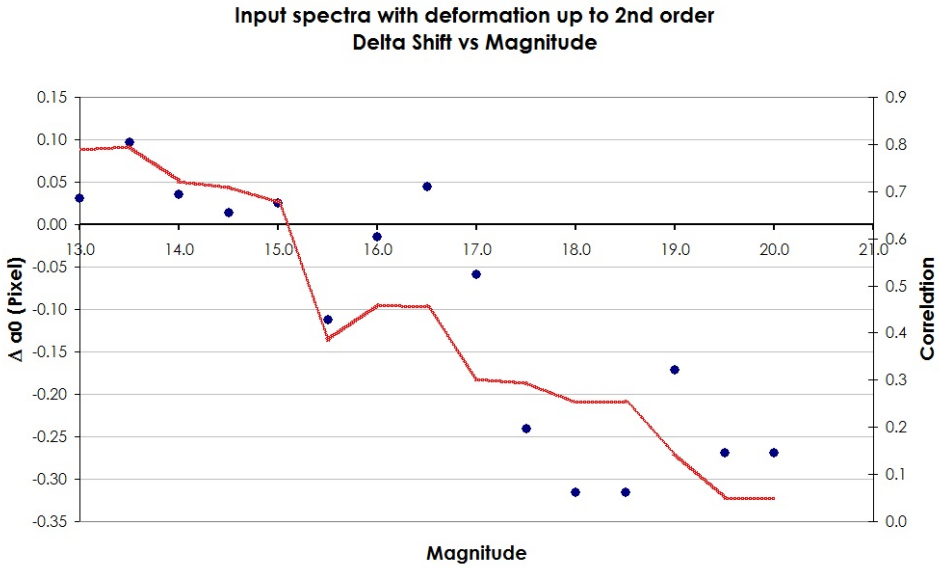

Figure 5.12: Correlation assessment results for stellar spectra including second order deformation. The plot show that the error on a_0 parameter using the Sequential Least SQuares Programming algorithm is smaller than validation requirement, at least up to J-band magnitude = 17.0.

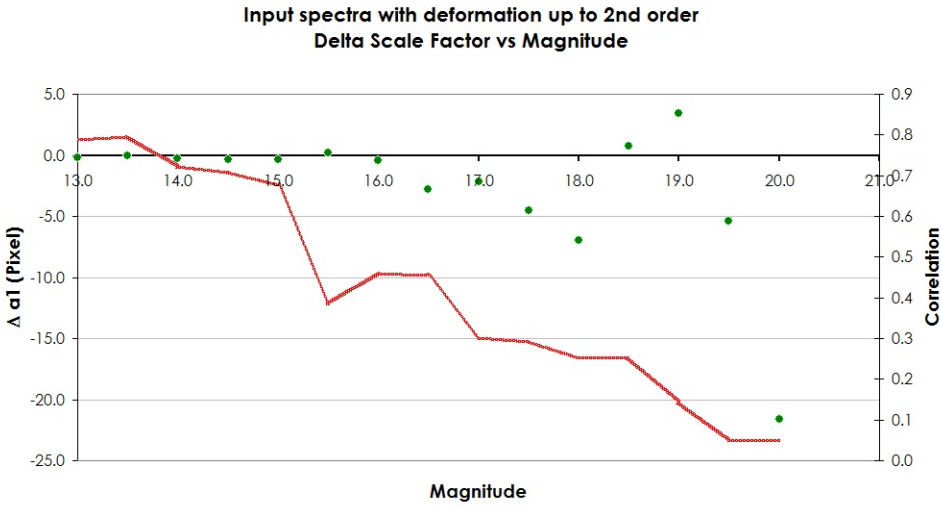

Figure 5.13: Correlation assessment results for stellar spectra including second order deformation. The plot show that the error on a_1 parameter using the Sequential Least SQuares Programming algorithm is smaller than validation requirement, at least up to J-band magnitude = 16.0.

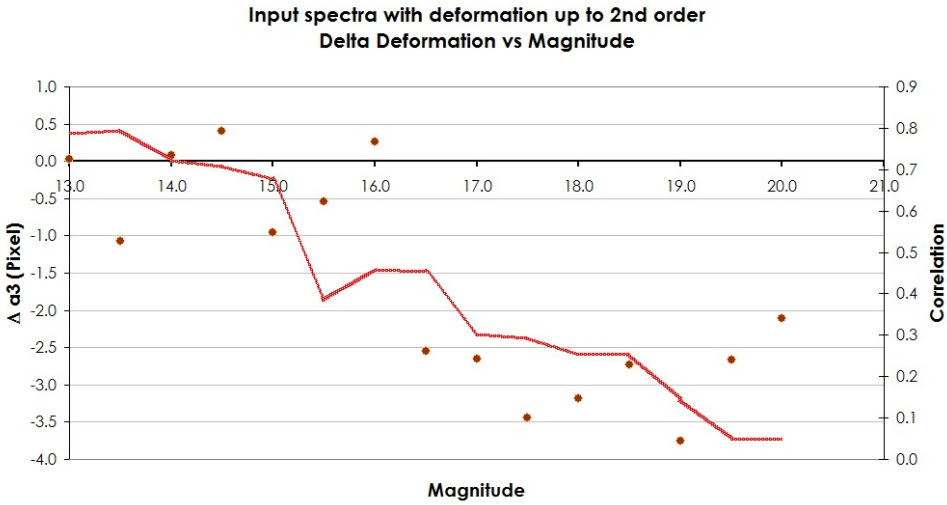

Figure 5.14: Correlation assessment results for stellar spectra including second order deformation. The plot show that the error on a_2 parameter using the Sequential Least SQuares Programming algorithm has a small dispersion up to J-band magnitude = 16.0.

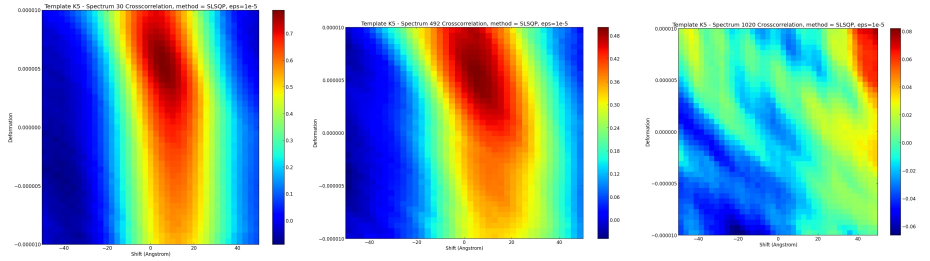

Figure 5.15: Correlation assessment results for stellar spectra including second order deformation. Heat maps showing the correlation as a function of shift and second order deformation for stellar spectra of AB magnitude, from left to right, equal to 13.0, 16.5 and 20.5 respectively. For brighter stars a correlation peak is well visible for shift $a_0 = 0$ and second order deformation $a_2 = 0.000005$. On the contrary, the spectrum of the faintest star is too noisy to produce a correlation peak for the correct couple of coefficients.

General Conclusions and Future Directions

The work presented in this PH.D thesis describes my research project, which has been devoted to the development of software tools aimed at improving the wavelength calibration of the Euclid Near Infrared Spectrometer and Photometer (NISP) instrument spectroscopic data.

The main task described above has been achieved through the development of

1. an End-to-End (E2ES) mission performance simulator for the Euclid NISP instrument
2. a validation process for the NISP spectra location inside the SIR Processing Function

Euclid is a Medium Class space mission of the European Space Agency (ESA) devoted to the mapping of the so-called dark Universe.

The extensive review of the actual knowledge of the Universe content presented at the beginning of this work (see section 1) shows that the ordinary matter ("baryonic matter") constitutes only a mere 4% of the content of the Universe. The remaining 95:1% is split up as follows: 26:3% is a form of non-luminous matter called the dark matter and 68:8% is dark energy.

The study of dark matter and dark energy is very challenging. In section 2 we showed how two powerful and robust probes of the dark Universe are weak lensing and baryon acoustic oscillations. Euclid will use these cosmological probes to measure the distance-redshift relation and the growth of structures. Observations are performed through the Visible Instrument (VIS, used to measure the shapes of galaxies) and NISP (used to provide near infrared photometry of all galaxies observed also with VIS and near infrared low resolution spectra and redshifts of millions galaxies).

The design of a space mission is a long and complex process. This is the reason why space agencies are interested in the development of dedicated software tools (i.e. mission performance simulators) that can simulate the complete behavior of the probe, its payload (i.e. those elements of the spacecraft specifically dedicated to producing mission data), and scientific data acquisition starting from synthetic scenes. Mission performance simulators are called "End-to-End" (E2ES) simulators.

ESA has a great and satisfying experience in using mission performance simulators in Earth Observations (EO) programs. The European Space Agency has recently promoted activities to define a reference architecture for E2ES and to test the feasibility of a generic simulation environment also for space missions.

The Euclid Mission has been selected as test case for the design and the implementation of an E2ES simulation environment similar to that already present for EO missions. All the activities related to the development of the E2ES have been supported by the ESA contract no. IPL-PTE/GLC/al/241.2014 of the duration of one year (end date: October 2015).

We started performing an extensive review of the E2ES dedicated to EO. This analysis showed us that:

- only a modular architecture can guarantee flexibility (i.e. ability to evolve in order to support the detailed mission design during the development phases) to our E2ES
- several aspects affect the definition of a reference architecture for E2E simulators (e.g. the scientific objective of the mission, the orbit characteristics, if instrument is active or passive, etc.)

We designed, then, a modular E2ES. Each module is designed to simulate a particular aspect of the measurement, from the definition of the pointing strategy to the extraction of the interesting parameter, passing through optics, detection chain and data processing pipeline simplified simulations. At the end of the simulation chain a cross-check between input and output results is performed in order to assess the correct functioning of the whole E2ES chain and the fulfillment of the mission requirements.

We realized a prototypical version of the E2ES, i.e. the "proto-E2ES". The proto-E2ES has reduced features, is limited to spectroscopic simulations (NISP-S) and the modules are implemented in a simplified version.

Two different versions of the proto-E2ES have been implemented: a preliminary version, delivered to ESA as one of the final products of the work supported by contract IPL-PTE/GLC/al/241.2014 and a more mature version, aimed at closing a major software issue.

In order to test the functionality and the performance of our proto-E2ES with respect to system requirements, we realized a Software Verification and Validation Plan. The final test phase showed that the simulator is able to correctly simulate the spectral extraction and the correct redshift is always measured for each source of the selected test catalog. Even with its basic functions, the prototype allows us to perform a sensitivity analysis on the pointing parameters and represents a useful tool in order to understand where open points are still present and to test, in a simplified way, possible solutions.

Future developments of the simulator should include:

1. a more realistic input catalog, with a higher number of sources distributed in a "sky representative" way
2. include in simulation the major source of contamination for the NISP instrument, i.e. Zodiacal Light Emission
3. simulate detector persistence. Image persistence in the IR array occurs whenever a pixel is exposed to light that exceeds more than about half of the full well of a pixel

in the array. Persistence can occur within a single visit, as the different exposures in a visit are dithered. Persistence also occurs from observations in a previous visit of completely different fields (see http://www.stsci.edu/hst/wfc3/)

4. more visualization tools for software verification and validation.

Exploiting the experience gained on the validation of the Euclid proto-E2ES (see section 4), in the second part of my work I investigated the possibility of validate the spectra location of the NISP instrument spectroscopic data using the observed stellar spectra.

The accuracy of the spectroscopic redshift measurements performed by Euclid depends, indeed, very strictly on the **accuracy of the spectroscopic data wavelength calibration**

This in turn depends on the determination of the **wavelength scale zero point**, which relays on the precise measurement of the position of each object in the NISP field of view during the spectroscopic exposures. Such positions are not directly observable and measurable using the spectroscopic data themselves. Is then possible to exploit bright stellar spectra? Can we expect to observe a suitable number of bright stars?

The error budget allocated to the spectra location requires that:

- the zero order position should be transferred to the first order position wavelength position with an error less than 0.3 pixel
- the pipeline shall use all relevant calibration data to give a spatially varying wavelength solution across the field-of-view, accurate to a level of 0.4 pixels (rms)

We derived, at first, the predicted number of stars contained in a certain sky area using the Galaxy model called "Trilegal". Five random patches at fixed galactic latitude have been selected (each one 2 squared degrees, i.e. an Euclid pointing), and combined, to build a virtual 10 deg^2 patch, that has been used for counting stars. For each Euclid pointing a thousand stars are expected.

We built an input catalog containing 1056 stellar spectra with J-band magnitudes ranging from 13.0 to 20.5.

Using the Python programming language a code has been developed which performs the verification through the following steps:

1. the observed stellar spectra are loaded from the input catalog and stored into a dictionary where each spectrum is represented by an object of a custom defined class
2. reference stellar spectra, called templates, are loaded through a specific function and stored into a dictionary
3. the continuum is subtracted from spectra and template
4. the observed spectra are deformed in order to take into account the deformation introduced by the NISP instrument due to the non-ideal nature of the instrument itself. This operation is done via a function, which applies a third degree polynomial to the wavelengths of input spectra. The fixed point of the non-zero degree transformations is in the center of the spectrum. The two most significant deformations are the **shift** of the spectrum (controlled by the constant term of the polynomial), and the **rescale factor** (supervised by the first order term)

5. a deformation is applied to templates, in order to match templates themselves with deformed spectra with a set of coefficients which is varied until the best match is found. The best match between the observed deformed spectrum and template is obtained through the evaluation of a merit function, the **correlation function**
6. the set of parameters that maximizes the correlation between the spectrum and the template is found using a minimization algorithm
7. the correlation is evaluated for each spectrum-template pair
8. the resulting set of parameters and correlation values are saved in an array

Firstly, we considered the varying of the correlation between stellar spectra and templates as a function of the shift (i.e. the cross-correlation), being the shift the most critical parameter for determining the location of the observed spectrum in the field of view. The correlation has been evaluated for different shift steps on a range from $-220\mathring{A}$ to $+200\mathring{A}$ in order to select the best step that captures all the features of the correlation function without increasing too much the computation load. This analysis has been performed for the first 50 objects of the input catalog. A similar investigation has been performed on the scale factor.

The correlation has then been computed for all stellar spectra of the input catalog (with shift and scale factor as for assessment output results), and templates. The scatter of the cross-correlation peak position for the different magnitude bins has been plotted against the magnitude itself. Results show that NISP spectra location validation can be successfully performed using stellar spectra, i.e.:

1. wavelength zero point validation - the error in the wavelength zero point is less than 0.3 pixel for stellar spectra up to J-band magnitude = 17.0
2. dispersion solution validation - the spatially varying wavelength solution across the field-of-view is accurate to a level of 0.4 pixels for stellar spectra up to J-band magnitude = 15.5

The analysis has been repeated, extending the deformation applied to input spectra to the second order. This time only one spectrum for magnitude bin has been selected. Results show that the error on polynomial coefficients using the Sequential Least SQuares Programming algorithm is smaller than validation requirement, at least up to J-band magnitude = 17.0 for a_0, magnitude = 16.0 for both a_1 and a_2.

Future developments of the script should include the possibility to use as input catalog stellar spectra produced by the SIR-MER processing function, with distortions and deformations produced by instrument deviations from ideal behavior.

Appendices

APPENDIX A

Python Script for the Euclid NISP Spectra Location Validation

```
import h5py
import numpy as np
import matplotlib.pyplot as plt
import math
from scipy import interpolate
from scipy import signal
from scipy.optimize import curve_fit, minimize, basinhopping
import time

# Remove continuum: python version of src/methods/pndEzRemoveContinuum.c,
    ↪ revision 9405 (from EZ)

def _localOddMirror (y_input, N, Nreflex, y_out):              # Input: y_input,
    ↪ which has N elemnts. Reflects on border this array y_out extended array
    y_out[Nreflex:Nreflex+N] = y_input[0:N]                    # Copy the centra
        ↪ part
    for j in range(0,Nreflex):
        y_out[Nreflex-j-1] = 2*y_input[0]-y_input[j]
        y_out[N+Nreflex+j] = 2*y_input[N-1]-y_input[N-j-1]

def _localEvenMirror (y_input, N, Nreflex, y_out):
    y_out[Nreflex:Nreflex+N] = y_input[0:N]                   # Copy the central
        ↪ part
    for j in range(0, Nreflex):
        y_out[Nreflex-j-1] = y_input[j]
        y_out[N+Nreflex+j] = y_input[N-j-1]

def _localMedianSmooth (y,n_points, n_range, y_out):          # Take an array
    ↪ lenght N, foreach j element computes median value on interval j-n_range
    ↪ /2,j+n_range/2 an put this value in y_out array
    half = n_range/2
    rest = n_range - 2*half
    for i in range (0, n_points):
        start = max (0, i-half)
        stop = min (i+half+rest, n_points-1)
        y_out[i] = np.median (y[start:stop])

def _localMeanSmooth (y, N, n, y_out):                        # Compute a average
    ↪ smooth
    half = n/2
    rest = n-2*half
    for i in range (0, N):
```

```
        start = max(0, i-half-rest)
        end = min(i+half, N-1)
        y_out[i] = np.mean (y[start:end+1])

def pndMathContinuumSmooth (data, norig, nsmoopix, nmedcycles, nmedsmoo, even,
    ↪ resolution, continuum):

# norig is the number of points in data, nsmoopix is the number of pixel to
    ↪ smooth on (suggested:400), nmedcycles is the number of
# cycles for median (suggested:5), nmedsmoo is the number of of cycles for mean
    ↪ (suggested: 5), even is not important (can be left
# to zero), resolution is delta lambda, continuum is the output array).

    k0 = 0
    k1 = 0
    nreflex = 0
    nbig = 0
    frac = 0.0
    j = 0
    k = 0

    frac = float (nsmoopix)/resolution - math.floor(float(nsmoopix)/resolution)
    nsmoopix = int (nsmoopix/resolution)

    if frac >= 0.5:
        nsmoopix += 1

    nsmoopix = min (nsmoopix, norig/2)

    frac = float(nmedsmoo)/resolution - math.floor(float(nmedsmoo)/resolution)
    nmedsmoo = int (nmedsmoo/resolution)

    if frac >= 0.5:
        nmedsmoo += 1

    nmedsmoo = max (nsmoopix, nmedsmoo)

# Find the first not null element, and put its index in k0

    for j in range (0, norig):
        if data [j] != 0:
            k0 = j
            break

# Find the last not null element, and put its index in k1

    for j in xrange (norig-1, -1, -1):
        if data [j] != 0:
            k1 = j
            break

    for j in range (0, norig):
        if data[j] != 0:
            k += 1

        if k > 10:
            break

# 0<=k0<=k1<=n_orig [k0,k1]="effective spectrum" lenght("effective spectrum")=nd

    nd = k1 - k0 + 1

# Set the reflection size
```

```
    tmp = 0.50 * nd

    if 5.0 * nsmoopix < tmp:
        tmp = 5.0 * nsmoopix

    if tmp < 10.0:
        tmp = 10.0

    nreflex = int(tmp)

# Spectrum reflected size

    nbig = nd + 2*nreflex

# Allocate array

    ysmoobig = np.zeros (nbig)

# Reflect original "effective spectrum" a set it in ysmoobig
# if even==1 reflects spectrum as an even function
# if even==0 reflacts spectrum as an odd function

    if even == 1:
        _localEvenMirror(data [k0:], nd, nreflex, ysmoobig)
    else:
        _localOddMirror(data [k0:], nd, nreflex, ysmoobig)

# WARNING!!! nmedsmoo must be an odd number; otherwise a sorted array will be
    ↪ sorted by the median smooth iterations

# Median smoothing

    temp = np.zeros (nbig)
    for k in range (0, nmedcycles):
        _localMedianSmooth(ysmoobig, nbig, 2*nmedsmoo+1, temp)
        ysmoobig [0:nbig]= temp[0:nbig]

# nmedsmoo must be odd

    nmedsmoo = 2 * (nmedsmoo/2)+1
    for k in range (0, nmedcycles):
        _localMedianSmooth(ysmoobig, nbig, nmedsmoo, temp)
        ysmoobig[0:nbig] = temp[0:nbig]

# Mean smoothing

    temp = np.zeros (nbig)

# Mean smooth size = nsmoopix/4

    _localMeanSmooth(ysmoobig, nbig, nsmoopix/4, temp)
    ysmoobig[0:nbig] = temp[0:nbig]

# Copy spectrum before k0

    for j in range (0, k0):
        continuum[j] = 0.0

# Set continuum inside "effective spectrum"

    for j in range (k0, k1+1):
        continuum[j] = ysmoobig[j-k0+nreflex]
```

```
# Copy spectrum after k1

    if k1+1 < norig:
        for j in range (k1+1, norig):
            continuum[j] = 0.0

# End of python version src/methods/pndEzRemoveContinuum.c, revision 9405


# Defining "downsample" and "decimate" functions from Signal Processing Library.
    ↪ The scipy.signal.decimate function does not work
# properly (introduce a deep spike at the beginning of the wavelength range).

def downsample(s, n, phase=0):
    """Decrease sampling rate by integer factor n with included offset phase.
    """
    return s[phase::n]

def decimate(s, r, n=None, fir=False):
    """Decimation - decrease sampling rate by r. The decimation process filters
    the input data s with an order n lowpass filter and then resamples the
    resulting smoothed signal at a lower rate. By default, decimate employs an
    eighth-order lowpass Chebyshev Type I filter with a cutoff frequency of
    0.8/r. It filters the input sequence in both the forward and reverse
    directions to remove all phase distortion, effectively doubling the filter
    order. If 'fir' is set to True decimate uses an order 30 FIR filter (by
    default otherwise n), instead of the Chebyshev IIR filter. Here decimate
    filters the input sequence in only one direction. This technique conserves
    memory and is useful for working with long sequences.
    """
    if fir:
        if n is None:
            n = 30
        b = signal.firwin(n, 1.0/r)
        a = 1
        f = signal.lfilter(b, a, s)
    else: #iir
        if n is None:
            n = 8
        b, a = signal.cheby1(n, 0.05, 0.8/r)
        f = signal.filtfilt(b, a, s)
    return downsample(f, r)

# This class represent a spectrum

class Spectrum:

    def __init__(self, Waves, Fluxes):
        self.waves = Waves
        self.fluxes = Fluxes

    def plot (self):
        plt.rc('text', usetex=True)
        plt.rc('font', family='serif')
        plt.plot (self.waves, self.fluxes, 'r')
        plt.xlabel(r'Wavelenght (\$\AA\$)',fontsize=12)
        plt.ylabel(r'Flux ($erg \times s^{-1} \times cm^{-2} \times Hz^{-1}$)',
            ↪ fontsize=12)
        plt.title('Spectrum')
        plt.show()

    def get_resampl_shifted_spectrum (self, new_waves, shift):
```

```
# Starting with the creation of a new template spectrum with wavelength
    ↪ resolution higher w.r.t. that of the simulated spectra
# to x-correlate with. In this way I do not loose spectral features below the
    ↪ simulated spectra resolution (13.4 Angstrom).

        first = new_waves[0]
        last = new_waves[new_waves.size - 1]
        points = new_waves.size
        step = (last - first) / (points - 1)
        x = self.waves
            ↪
            ↪ # Template wavelength array
        y = self.fluxes
            ↪
            ↪ # Template flux array
        add_points = 100
        x_start = np.linspace( x[0] - (x[1] - x[0]) * add_points, x[0],
            ↪ add_points, endpoint=False)
        y_start = np.tile(y[0], add_points)
        x_stop =  np.linspace(x[-1] + (x[-1] - x[-2]), x[-1] + (add_points + 1)
            ↪ * (x[-1] - x[-2]), add_points, endpoint=False)
        y_stop = np.tile ( y [-1] ,add_points)
        x_final = np.concatenate ( [ x_start, x, x_stop ] )
        y_final = np.concatenate ( [ y_start, y, y_stop ] )
        f = interpolate.interp1d(x_final, y_final, fill_value=0, bounds_error=
            ↪ False)            # Interpolating wavelength and flux
        xnew = np.zeros(points * 10)
            ↪                                                              #
            ↪ Defining a new wavelength array with a resolution equal to 10
            ↪ times that of the simulated spectra
        for i in range(0, points):
            current_start = new_waves[i]
            if 1 < points-i:
                current_step = (new_waves[i + 1] - new_waves[i]) * 0.1
            for j in range(0, 10):
                xnew[i*10 + j] = current_start + current_step*j
        ynew = f(xnew)
            ↪
            ↪ # Defining a new flux array as an interpolation with the new
            ↪ wavelength array
            ↪                                                          # New
            ↪ template spectrum with right wavelength interval, higher
            ↪ resolution
        resampled_templ_flux = decimate(ynew, 10, n=7)
        resampled_templ_spectrum = Spectrum(new_waves, resampled_templ_flux)
        return resampled_templ_spectrum


    def remove_zeros(self):
        start = 0
        # skip zeros at beginning
        while self.fluxes[start]==0 and start < self.fluxes.size -1:
            start = start+1
        end = self.fluxes.size - 1

        # skip zeros at end
        while self.fluxes[end]==0 and end > start:
            end = end-1

        # recreate y without zero elements
        self.fluxes = self.fluxes[start:end + 1]
        self.waves = self.waves[start:end + 1]
```

```
    def trim_wavelength(self, min_wavelength, max_wavelength):
        start = 0
        # trimming spectrum at beginning
        while self.waves[start] < min_wavelength:
            start = start + 1
        end = self.fluxes.size - 1

        # trimming spectrum at end
        while self.waves[end] > max_wavelength:
            end = end - 1

        # recreate y after trimming
        self.fluxes = self.fluxes[start:end + 1]
        self.waves = self.waves[start:end + 1]

# This class represents a spectrum sampled at a constant interval

class Spectrum_2:

    # xstart is starting point for x (first sample)
    # xstep is the interval between samples
    # y is the array of samples

    def __init__(self, xstart, xstep, y):
        self.xstart = xstart
        self.xstep = xstep
        self.y = y

    def get_x_array (self):
        points = len (self.y)
        return np.linspace(self.xstart, self.xstart + self.xstep*points, points)

# Returns a spectrum 2 by resampling the given spectrum in the interval xstart-
    ↪ xstop and with step=xstep

def get_Spectrum2_from_Spectrum (spectrum, xstart, xstep, points):
    waves = np.linspace(xstart, xstart+xstep*points, points)
    resampled_spectrum = spectrum.get_resampl_shifted_spectrum(waves, 0)
    return Spectrum_2 (xstart, xstep, resampled_spectrum.fluxes)

# Returns a Spectrum object containing the given template

def template_spectrum (template_name):                    # Defining a function to
    ↪ generate template spectrum
    f = open("/home/user/Work/Euclid_SIR_Verif_Valid/templates/" + template_name
        ↪ , "r")

    w_arr = []                                            # Initialize two empty
        ↪ arrays
    f_arr = []

    for line in f:
        wave_templ, flux_templ = line.split()             # Splitting lines into
            ↪ wave and flux elements
        num_wave_templ = float (wave_templ)
        num_flux_templ = float (flux_templ)               # Converting array
            ↪ elements into floating numbers
        w_arr.append (num_wave_templ)                     # Creating waves and flux
            ↪  arrays
        f_arr.append (num_flux_templ)

    waves_templ = np.array (w_arr)                        # Converting waves and
```

```
        ↪ flux arrays into numpy arrays
    flux_templ = np.array (f_arr)

    s_templ = Spectrum (waves_templ, flux_templ)        # Creating the "template
        ↪ spectrum" object
    return s_templ

# Defining a function to obtain a resampled, shifted template with continuum
    ↪ subtracted

def get_spectrum_without_continuum (data, nsmoopix, nmedcycles, nmedsmoo, even,
    ↪ resolution):
    continuum = np.zeros(len(data))
    pndMathContinuumSmooth(data, len(data), nsmoopix, nmedcycles, nmedsmoo, even
        ↪ , resolution, continuum)
    resample_without_continuum_fluxes = data - continuum
    return resample_without_continuum_fluxes

# Code for Gaussian fitting of the cross-correlated spectra

# Gaussian function with pedestal to fit
def Gauss(x, height, position_x, sigma, pedestal):
    return pedestal + height * np.exp(-(x - position_x) ** 2 / (2 * sigma ** 2))


# This function guesses the parameters for a gaussian fit given the x and y data
    ↪  in two arrays
def Guess_Gauss_parameters(x, y):
    # take minimum as pedestal, maximum - minimum as height, maximum position as
        ↪  position_x

    max_index = np.argmax(y)
    min_index = np.argmin(y)
    position_x = x[max_index]
    pedestal = y[min_index]
    height = y[max_index] - y[min_index]

    # compute the half maximum leve

    fwhm_threshold = pedestal + height * 0.5

    # start from the maximum position and go left until we go below the fwhm
        ↪ threshold

    left_side_index = max_index
    while left_side_index > 0 and y[left_side_index] > fwhm_threshold:
        left_side_index -= 1

    # start frtom the maximum position and go right until we go below the fwhm
        ↪ threshold

    right_side_index = max_index
    while right_side_index < len(y) - 1 and y[right_side_index] > fwhm_threshold
        ↪ :
        right_side_index += 1
    fwhm = x[right_side_index] - x[left_side_index]
    sigma = fwhm / 2.35  # ratio between fwhm and sigma for an ideal gaussian
    return (height, position_x, sigma, pedestal)


########################
# Here begin execution #
########################
```

```
# Get current time
start_time = time.time()

# Defining empty dictionary
spectra = {}
templates = {}

# Read spectra in the dictionary
with h5py.File('eos_rank01.h5','r') as hf:
    groups = hf.keys()                              # put into the groups array
        ↪ the names (keys) of all the groups in the .h5 file
    for i in groups:
        gp = hf.get(i +'/COMBINED')                 # take data group, COMBINED
            ↪ subgroup
        arr1 = np.array(gp.get('Waves'))            # build array one containing
            ↪  wavelenghts
        arr2 = np.array(gp.get('Fluxes'))           # build array two containing
            ↪  fluxes
        s = Spectrum (arr1, arr2)                   # build the spectrum object
        spectra [i] = s                             # put the spectrum object in
            ↪  the "spectra" dictionary

print("%s spectra loaded\n" % (len(spectra)))

# Load stellar templates
templates["F5"] = template_spectrum ("templ_F5.dat")
templates["G4"] = template_spectrum ("templ_G4.dat")
templates["K5"] = template_spectrum ("templ_K5.dat")
templates["M4"] = template_spectrum ("templ_M4.dat")

def spectrum_deformation (spectrum, a0, a1, a2, a3):
    spectrum_wavelength_centre = (spectrum.waves[0] + spectrum.waves[-1]) / 2
    spectrum_wavelengths_deformed = spectrum_wavelength_centre + a0 + a1 * (
        ↪ spectrum.waves - spectrum_wavelength_centre) + a2 * (spectrum.waves -
        ↪  spectrum_wavelength_centre) ** 2 + a3 * (spectrum.waves -
        ↪ spectrum_wavelength_centre) ** 3
    resampled_spectrum = spectrum.get_resampl_shifted_spectrum(
        ↪ spectrum_wavelengths_deformed, 0)
    print min(spectrum_wavelengths_deformed), max(spectrum_wavelengths_deformed)
    return Spectrum(spectrum.waves, resampled_spectrum.fluxes)

def normalized_correlation (params, template, spectrum):

    a0 = params[0]          #shift
    a1 = params[1]          #scale
    a2 = params[2]          #deformation^2
    a3 = params[3]          #deformation^3

    # Introducing shift and deformation on template wavelengths
    spectrum_wavelength_centre = (spectrum.waves[0] + spectrum.waves[-1]) / 2
    template_wavelengths = spectrum_wavelength_centre + a0 + a1 * (spectrum.
        ↪ waves - spectrum_wavelength_centre) + a2 * (spectrum.waves -
        ↪ spectrum_wavelength_centre) ** 2 + a3 * (spectrum.waves -
        ↪ spectrum_wavelength_centre) ** 3

    # Resampling the stellar template spectrum
    resampled_template = template.get_resampl_shifted_spectrum(
        ↪ template_wavelengths, 0)

    # Computing template with the continuum removed
    res_template_cont_sub = get_spectrum_without_continuum(resampled_template.
        ↪ fluxes, 400, 5, 5, 1, resampled_template.waves[1] -
```

```
        ↪ resampled_template.waves[0])

    # Computing spectrum with the continuum removed
    spectrum_cont_sub = get_spectrum_without_continuum(spectrum.fluxes, 400, 5,
        ↪ 5, 1,spectrum.waves[1] - spectrum.waves[0])

    # Computing correlation
    correlation = np.dot(spectrum_cont_sub, res_template_cont_sub) / np.sqrt(np.
        ↪ dot(spectrum_cont_sub, spectrum_cont_sub) * np.dot(
        ↪ res_template_cont_sub, res_template_cont_sub))

    return correlation

def rescale_params (params):
        return [
                params[0]*10,
                params[1],
                params[2]*1e-6,
                params[3]*1e-10,
        ]

def minus_normalized_correlation_rescale_params (params, template, spectrum):
    return -(normalized_correlation(rescale_params(params), template, spectrum))

polynomial_fit = open("/home/user/Work/Euclid_SIR_Verif_Valid/
    ↪ Wavelength_Calibration_final/polynomial_fit/Polinomial_3_Fit.txt", "w")
polynomial_fit.write("All␣spectra␣have␣been␣distorted␣using␣the␣following␣
    ↪ parameters:\n")
polynomial_fit.write("a0(shift)␣=␣4.000\n")
polynomial_fit.write("a1(scale)␣=␣1.030\n")
polynomial_fit.write("a2(deformation_2)␣=␣5.000e-6\n")
polynomial_fit.write("a3(deformation_3)␣=␣1.000e-8\n")
polynomial_fit.write("\n")
polynomial_fit.write("Spectrum␣␣Template_Name␣␣a0␣␣a1␣␣a2␣␣a3␣␣Correlation\n")
polynomial_fit.write("\n")

for number, spectrum in spectra.items():
    best_max_correlation = None
    best_heat_map_data = None
    best_heat_map_x = None
    best_heat_map_y = None

    spectrum.remove_zeros()

    spectrum_deformed = spectrum_deformation(spectrum, 4.0, 1.030, 0.000005,
        ↪ 0.0)

    for template_name, template in templates.items():
        print("Computing␣spectrum␣\"" + number + "\"␣with␣template␣" +
            ↪ template_name + "\"-␣time␣%s␣s\n" % (time.time()-start_time))
        p0 = (0., 1., 0., 0.)
        bnd = (-1,1), (-1.05,1.05), (-10,10), (-2,2)
        popt = minimize(minus_normalized_correlation_rescale_params, p0, args=(
            ↪ template, spectrum_deformed), bounds=bnd, method='SLSQP', options
            ↪ ={'eps':1e-5})
        popt_rescaled = rescale_params(popt.x)
        correlation = -popt.fun
        polynomial_fit.write("{:8.5s}".format(number) + "{:8.5s}".format(
            ↪ template_name) + "␣␣{:10.4f}".format(popt_rescaled[0]) + "␣␣
            ↪ {:10.4f}".format(popt_rescaled[1]) + "␣␣{:12.4e}".format(
            ↪ popt_rescaled[2]) + "␣␣{:12.4e}".format(popt_rescaled[3]) + "␣␣
            ↪ {:10.4f}".format(correlation) + '\n')
```

```
polynomial_fit.close()
```

Bibliography

Abazajian, K. N. et al. 2009, *Astrophys. J. Suppl.*, 182, 543

Abbott, T. M. C. et al. 2017

Abell, P. A. et al. 2009

Adam, R. et al. 2016, *Astron. Astrophys.*, 594

Ade, P. A. R. et al. 2013, *Astron. Astrophys.*, 571, 66

Ade, P. A. R. et al. 2014, *Astron. Astrophys.*, 571, 66

Ade, P. A. R. et al. 2016, *Astron. Astrophys.*, 594

Alam, U. & Sahni, V. 2006, *Phys. Rev. D*, 73, 084024

Alcock, C. et al. 2000, *Astrophys. J.*, 542, 281

Amendola, L. 2000, *Phys. Rev. D*, 62, 18

Amendola, L., Quercellini, C., & Giallongo, E. 2005, *Mon. Not. R. Astron. Soc.*, 357, 429

Archeo E2E Team. 2013, ARCHEO-E2E Final Report, Tech. rep., GMV

Armendariz-Picon, C. et al. 2001, *Phys. Rev. D*, 103510

Bagot, D. 2015, EC SGS Coding Standards, Tech. rep., Euclid Consortium

Battaglia, P. & Romelli, E. 2014, EUCLID E2E Analyses and Trade-Offs, Tech. rep., Consorzio Interuniversitario per la Fisica Spaziale

Battaglia, P. & Romelli, E. 2015a, EUCLID E2E Design Definition, Tech. rep., Consorzio Interuniversitario per la Fisica Spaziale

Battaglia, P. & Romelli, E. 2015b, EUCLID E2E Requirements Baseline, Tech. rep., Consorzio Interuniversitario per la Fisica Spaziale

Battaglia, P. & Romelli, E. 2015c, EUCLID E2E Verification and Validation Plan, Tech. rep., Consorzio Interuniversitario per la Fisica Spaziale

Binetruy, P. 1999, *Phys. Rev. D*, 60

Bolton, A. S. et al. 2006, *Astrophys. J.*, 638, 703

Choudhury, T. R. & Padmanabhan, T. 2005, *Astron. Astrophys.*, 429, 807

Content, D. et al. 2013

Cyburt, R. H. 2004, *Phys. Rev. D*, 70

Derue, F. et al. 1999, *Astron. Astrophys.*, 351, 87

Dubath, P. 2015, in Astroinformatics Proceedings IAU Symposium No. 325, 10

Ealet, A. 2016, NISP Calibration Plan, Tech. rep., Euclid Consortium

Einstein, A. 1917, *Preuss. Akad. Wiss. Sitzungsber.*, 142
Einstein, A. 1936, *Science*, 84, 507
Eisenstein, D. J. & Hu, W. 1999, *Astrophys. J.*, 511, 5
Eisenstein, D. J. et al. 2005, *Astrophys. J.*, 633, 560
Ellis, R. S. 2010, *Phylos. Trans. of the Royal Soc.*, 368, 967
ESA Board for Software Standardization and Control. 1995, EUCLID E2E Verification and Validation Plan, Tech. rep., European Space Agency
Euclid Project Team. 2013, Euclid System Requirements Document, Tech. rep., European Space Agency - Euclid Consortium
Flaugher, B. et al. 2015, *Astron. J.*, 150, 43
Gibson, R. 1992, Managing Computer Projects: Avoiding the Pitfalls (Bcs Practitioner Series) (Prentice Hall)
Goobar, A., Hannestad, S., Mortsell, E., & Tu, H. 2006, *Journal of Cosmology and Astropart. Physics.*, 2006, 19
Gregorio, A. et al. 2016, in American Institute of Aeronautics and Astronautics, SpaceOps 2016 Conference
Gross, A. et al. 2015, in Astronomical Data Analysis Software and Systems:XXIV, Vol. 495
Guth, A. H. 1981, *Phys. Rev. D*, 347
HDF Group. 2017
Hinshaw, G. et al. 2013, *Astrophys. J. Suppl.*
Hubble, E. 1929, in Proceeding of the National Academy of Sciences of the United States of America, Vol. 15, 168
IEEE Standards Board. 1990, IEEE Standard Glossary of Software Engineering Terminology, Tech. rep., IEEE
Jenkins, A. et al. 1998, *Astrophys. J.*, 499, 20
Kamenshchik, A. Y. et al. 2001, *Phys. Lett. B*, 511, 265
Kirshner, R. P. 2003, in Proceeding of the National Academy of Sciences of the United States of America, Vol. 101, 8
Komatsu, E. et al. 2009, *Astrophys. J. Suppl.*, 180, 330
Levi, M. et al. 2013, 14
Luo, M. J. 2014, *Nuclear Physics B*, 884, 344
Maoz, D. 2007, Astrophysics in a Nutshell (Princeton University Press)
Mather, J. C. et al. 1990, *Astrophys. J.*, 354
Myers, S. E. et al. 2003, *Mon. Not. R. Astron. Soc.*, 341, 1
Perlmutter, S. et al. 1999, *Astrophys. J.*, 517, 565
Perrotta, F. et al. 2000, *Phys. Rev. D*, 61
Riess, A. G. et al. 1998, *Astron. J.*, 116, 1009
Riess, A. G. et al. 2004, *Astrophys. J.*, 607, 665
Rubin, V. C. 1983, *Scient. Americ.*, 248, 96
Rubin, V. C.and Kent Ford, W. 1970, *Astrophys. J.*, 159, 379
Sahni, V. & Shtanov, Y. 2003, *Journal of Cosmology and Astropart. Physics.*, 0311
Scodeggio, M. 2015a, EUCLID SGS SIR Processing Function Validation Plan, Tech. rep., European Space Agency - Euclid Consortium
Scodeggio, M. 2015b, EUCLID SGS SIR Requirements Specification Document, Tech. rep., European Space Agency - Euclid Consortium
Sunyaev, R. A. & Zeldovich, Y. B. 1970, *Astrophys. Space Sci.*, 7, 3
Volovik, G. E. 2005, *Annalen der Physik.*, 14, 165

Weinberg, S. 1989, *Rew. Modern Physics*, 61, 1
Wittman, D. M. et al. 2000, *Nature*, 405, 143
Zhao, G. et al. 2016, *Mon. Not. R. Astron. Soc.*, 457, 2377
Zlatev, I. et al. 1999, *Phys. Rev. Lett.*, 82, 896
Zwicky, F. 1937, *Astron. J.*, 86, 217

Acknowledgments

Firstly, I would like to express my sincere gratitude to my advisor, Prof. Anna Gregorio, and to my co-supervisor, Dr. Marco Scodeggio, for their continuous support of my Ph.D study and related research, for their patience, motivation, and knowledge. Their guidance helped me in all the time of research and writing of this thesis.

Besides my advisor and co-supervisor, I would like to thank Dr. Raffaella Franco and Dr. Rene Laureijs (Euclid Project Scientist) of the European Space Agency and Dr. Bianca Garilli of the National Institute for Astrophysics (IASF) - INAF Milano.

I thank the European Space Agency, the National Institute for Astrophysics, the Inter-University Consortium for Space Physics and the University of Trieste for having funded my research activity.

My sincere thanks also goes to my referee, Prof. Davide Maino (Physics Department of University of Milan) and Dr. Harry Teplitz (California Institute of Technology - Caltech) for their insightful comments and hard questions which incented me to widen my research from various perspectives.

I thank my fellows in INAF- IASF Milano: Dr. Paolo Franzetti and Dr. Marco Fumana for their precious support to my work, Adriana, Alida, Stefano, Giorgio and Paolo for their friendship and warm welcome in the research group.

Last but not the least, I would like to thank my family: my parents and to my husband Filippo for supporting me spiritually throughout writing this thesis and my life in general.

Someone who deserves a special mention in this acknowledgment list is Aniello: thanks to him I had the opportunity to take up this Ph.D. study.

The Euclid Space Mission: Development of End-to-End Simulation Software Tools Aimed at Improving the Wavelength Calibration of NISP Instrument Spectroscopic Data

We live in a Universe composed, mostly, of mysterious ingredients: 26.8% is a form of non-luminous matter called "*dark matter*" and the remaining 68.3% is "dark energy".

Is dark energy, which is accelerating the expansion of the Universe, a merely cosmological constant? Or, instead, is it a manifestation of a break-down of General Relativity and deviations from the law of gravity? What are the nature and properties of dark matter?

Several observational probes can help us to disentangle different answers, being weak gravitational lensing and baryon acoustic oscillations the two most powerful methods for dark Universe investigation. A great effort has been done by the international community of scientist to perform observations in the forthcoming years with the goal of mapping hundreds of milliions of galazies.

The Euclid mission is a medium class space mission of the European Space Agency. Starting from 2021, it will map the geometry of the by investigating the distance-redshift relationship and the evolution of cosmic structure. It will cover the entire period where dark energy played a significant role in accelerating the expansion.

Such complex missions need dedicated software tools that can simulate the complete behaviour of the probe, its payload, and scientific data acquisition starting from synthetic scenes.

This Ph.D. thesis deals with the realization and validation of software tools dedicated to the improvement of the wavelength calibration of the Near Infrared Spectrometer and Photometer onboard the Euclid probe.